

TABLE OF CONTENTS

	Page
INTRODUCTION	1
CHAPTER 1 LITERATURE REVIEW	23
1.1 Morphing wings at LARCASE at ÉTS	23
1.2 The different types of morphing wing	25
1.2.1 Wing aspect ratio	25
1.2.2 Morphing of the camber.....	25
1.2.3 Morphing of the trailing edge	27
1.2.4 Morphing of the leading edge	28
1.2.5 Morphing with compliant mechanisms.....	28
1.3 Design constraints.....	29
CHAPTER 2 RESEARCH APPROACH AND THESIS ORGANIZATION.....	31
2.1 Research approach	31
2.2 Thesis organization	32
CHAPTER 3 EXPERIMENTAL VALIDATION OF A NEW MORPHING TRAILING EDGE SYSTEM USING PRICE – PAÏDOUSSIS WIND TUNNEL TESTS	35
3.1 Introduction.....	36
3.2 Design of the Morphing Wing System	38
3.2.1 Deformation of the Camber	38
3.2.2 Deformation of the Trailing Edge.....	39
3.3 Sizing design and control of the MTE	44
3.3.1 Sizing design.....	44
3.3.2 MTE control.....	46
3.4 Manufacturing and wind tunnel testing	48
3.4.1 Manufacturing of the MTE system	48
3.4.2 Wind Tunnel Tests.....	49
3.5 Comparison of aerodynamics coefficients for a MTE versus a conventional aileron .	63
3.5.1 Comparison of aerodynamics coefficients.....	65
3.5.2 Electrical consumption.....	68
3.6 Conclusion	69
CHAPTER 4 DESIGN, MANUFACTURING AND TESTING OF A NEW CONCEPT FOR A MORPHING LEADING EDGE USING A SUBSONIC BLOW DOWN WIND TUNNEL.....	71
4.1 Introduction.....	72
4.2 Design of the MLE.....	76
4.3 Structural Analysis of the MLE System	81
4.4 Experimental setup of the MLE system.....	87

4.5	Wind Tunnel Tests Results	97	
4.6	Aerodynamic simulation of the wing.....	102	
4.7	Conclusion and further work	114	
CHAPTER 5 DESIGN AND VALIDATION OF A NEW MORPHING CAMBER SYSTEM BY TESTING WITH THE SUBSONIC PRICE – PAÏDOUSSIS WIND TUNNEL			117
5.1	Introduction.....	118	
5.2	Problem statement.....	120	
5.3	Design of the Morphing Camber System.....	122	
5.4	Prototype manufacturing.....	128	
5.5	The Price – Païdoussis wind tunnel	130	
5.6	Result	132	
5.7	Discussion.....	135	
5.8	Application of results with the UAS-S4 Ehécatl	137	
5.9	Conclusion	148	
CHAPTER 6 DISCUSSION OF RESULTS.....			151
CONCLUSION AND RECOMMENDATIONS			157
BIBLIOGRAPHY.....			159

LIST OF TABLES

		Page
Table 0.1	Characteristics of UAS S4 Ehécatl	1
Table 3.1	Range and resolution for ATI Omega 160 F/T sensor.....	52
Table 3.2	Size of the slits in the deformable rib	55
Table 4.1	Dimensions of the slits.....	85
Table 4.2	NEMA 23 Bipolar Stepper product specification.....	90
Table 4.3	Range and resolution for ATI Omega 160 force and torque (F/T) sensor. $F_{x,y,z}$ represent the forces and $T_{x,y,z}$ represent the torques.....	90
Table 4.4	PhidgetStepper Bipolar HC product specification.....	96
Table 5.1	Slits' dimensions on the trailing edge of the rib	123
Table 5.2	Slits' dimensions on the leading edge of the rib	123
Table 5.3	MTE tip displacement values according to the servomotor angle of rotation	125
Table 5.4	Morphing cases studied in wind tunnel	132
Table 5.5	Geometric data of the UAS-S4	137
Table 5.6	Equation of lift coefficient variation with angle of attack	139
Table 5.7	Values of cl_α for each studied case	140
Table 5.8	Equation of drag coefficient variation with angle of attack.....	141

LIST OF FIGURES

		Page
Figure 0.1	UAS-S4 Ehécatl of Hydra Technologies	2
Figure 0.2	Airfoil NACA0012 (red) and airfoil NACA4412 (green) superimposed....	4
Figure 0.3	Lift coefficient variation with the angle of attack for NACA0012 and NACA4412 airfoil for Reynolds numbers of 150,000 to 600,000	6
Figure 0.4	Zoom of lift coefficient variation with the angle of attack for NACA0012 and NACA4412 airfoils for Reynolds number from 150,000 to 600,000	7
Figure 0.5	Drag coefficient variation with the angle of attack for the NACA4412 airfoil (red) and for the NACA0012 airfoil (blue) at a Reynolds number of 500,000.....	8
Figure 0.6	Methodology's main steps	9
Figure 0.7	Step 1: List of systems	10
Figure 0.8	Step 2: Systems analysis	11
Figure 0.9	Step 3: Systems design.....	12
Figure 0.10	Step 4: Systems manufacturing.....	12
Figure 0.11	Step 5: Systems wind tunnel testing	13
Figure 0.12	Step 6: Integration in the UAS-S4	13
Figure 0.13	Side view of the reference wing.....	16
Figure 0.14	Top view of the reference wing	16
Figure 0.15	Variation of the drag coefficient with the angle of attack measured in the wind tunnel and calculated theoretically.....	18
Figure 0.16	Variation of the lift coefficient with the angle of attack measured in the wind tunnel and calculated theoretically.....	20
Figure 0.17	Variation of the pitch coefficient with the angle of attack measured in the wind tunnel and calculated theoretically.....	21

Figure 3.1	Control of the trailing edge rib deformation	41
Figure 3.2	Deformed rib in CATIA V5.....	41
Figure 3.3	NACA0012 airfoil with inclined aileron a) and with MTE b).....	41
Figure 3.4	Comparison of the performance of a wing with inclined aileron and MTE	43
Figure 3.5	Deformation of the rib	46
Figure 3.6	FEA of MTE control under aerodynamical pressures	47
Figure 3.7	Servomotor specifications.....	47
Figure 3.8	Structure of the MTE system	48
Figure 3.9	Prototype with a MTE system.....	48
Figure 3.10	Reference rigid wing dimensions.....	50
Figure 3.11	LARCASE Price-Païdoussis subsonic wind tunnel.....	51
Figure 3.12	Drag coefficients variation with angle of attack for the reference wing.....	52
Figure 3.13	Lift coefficients variation with angle of attack for the reference wing.....	53
Figure 3.14	Pitch coefficients variation with angle of attack for the reference wing.....	54
Figure 3.15	Size and location of the slits in the MTE rib (unit: in)	55
Figure 3.16	0.75 in displacement of the trailing edge tip (19.05 mm) for a 7° rotation	56
Figure 3.17	Controlling distance	57
Figure 3.18	Test wing with MTE	57
Figure 3.19	Influence of the MTE on the drag coefficient at 15 m/s (49.21 ft/s)	58
Figure 3.20	Experiment 1 with all slits covered by tapes (continuous surface).....	59

Figure 3.21	Experiment 2 tapes covering the intersection between the morphing fixed parts were removed.....	59
Figure 3.22	Experiment 3 with tapes installed on one side of the slits (deflector)	60
Figure 3.23	Experiment 4 with tapes installed on both sides of the slits	60
Figure 3.24	Cd variation with the angles of attack at the speed of 15 m/s (49.21 ft/s).....	62
Figure 3.25	Zoom-in of the drag coefficients variation with the angles of attack between -8° and 8°	62
Figure 3.26	Wing L/D ratio variation with the angle of attack	63
Figure 3.27	2D plan of the wing with an aileron.....	64
Figure 3.28	CL and CD variation with the angle of attack. At 15 m/s (49.21 ft/s) for each system	66
Figure 3.29	L/D ratio variation with the angle of attack at 15 m/s (49.21 ft/s) for each system	67
Figure 3.30	Cd variation with angle of attack- zoomed-in around 0°	67
Figure 3.31	L/D ratio variation with angle of attack- zoomed-in around 0°	68
Figure 4.1	Drag coefficient variation with lift coefficient (experimental values). Legend: MTE, morphing trailing edge	73
Figure 4.2	Morphing of camber: NACA0012 airfoil (grey) and NACA4412 airfoil (black)	74
Figure 4.3	Drag coefficient variation with lift coefficient variation for NACA0012 (grey) and NACA4412 (black) (computed values). The curves intersect for a lift coefficient $C_L = 0.367$ and for an angle of attack $AoA = 2.97^\circ$	74
Figure 4.4	Internal structure of the wing	77
Figure 4.5	Morphing leading edge (MLE) system	78
Figure 4.6	Connected morphing ribs with the control rod	78

Figure 4.7	Control arm through the main spar	79
Figure 4.8	Slits on wing surface	79
Figure 4.9	Impact of the slits on wing drag.....	80
Figure 4.10	Prototype of the MLE for wind tunnel testing	81
Figure 4.11	Slit parameter definitions. l = width of the slit, p = depth of the slit, L = distance between the slit and the LE, e = airfoil thickness and t = thickness at bottom of the slit.....	82
Figure 4.12	MLE with the aerodynamic loads around the wing	83
Figure 4.13	Finite element analysis (FEA) structural mesh of the MLE system	84
Figure 4.14	FEA of the Structure of the MLE system	85
Figure 4.15	Maximum displacement of the MLE tip.....	86
Figure 4.16	Maximum displacement values of the MLE tip.....	87
Figure 4.17	Test wing in the Price - Païdoussis subsonic wind tunnel	88
Figure 4.18	Price - Païdoussis subsonic blow down wind tunnel dimensions	88
Figure 4.19	Section of the Price-Païdoussis subsonic wind tunnel of the Laboratory of Applied Research in Active Controls, Avionics, and AeroServoElasticity (LARCASE)	89
Figure 4.20	Internal mechanism of the aerodynamic loading scales	91
Figure 4.21	Upper disc of the aerodynamic loading scales.....	92
Figure 4.22	Leading edge (LE) of the prototype in its morphed configuration	93
Figure 4.23	LabVIEW interface.....	94
Figure 4.24	Display of forces read by F/T sensor	94
Figure 4.25	Disc angle controller	95
Figure 4.26	Servomotor controller	95
Figure 4.27	Variation of the lift coefficient with angle of attack.....	98

Figure 4.28 Variation of the lift coefficient with morphing angle of the MLE99

Figure 4.29 Variation of the drag coefficient with angle of attack100

Figure 4.30 Variation of the drag coefficient with morphing angle of the MLE101

Figure 4.31 Variation of the lift on drag (L/D) ratio with angle of attack101

Figure 4.32 Wing with 4 mm displacement of LE tip.....103

Figure 4.33 Model of wing with MLE103

Figure 4.34 Fluid domain of the simulation104

Figure 4.35 Fluent simulation104

Figure 4.36 Fluid domain mesh of the simulation.....105

Figure 4.37 Lift coefficient variation with angle of attack.....106

Figure 4.38 Drag coefficient variation with angle of attack.....107

Figure 4.39 Drag variation with angle of attack for MLE at 0°107

Figure 4.40 Drag coefficient variation with angle of attack with experimental values shift by 3°108

Figure 4.41 MLE with grooves and bumps109

Figure 4.42 Lift coefficient variation with angle of attack for improve modeling110

Figure 4.43 Drag coefficient variation with angle of attack for improved modeling110

Figure 4.44 Pressure around the wing with MLE at 18° with an airspeed of 20 m/s and (a) angle of attack 0°, (b) angle of attack 10°, and (c) angle of attack 18°111

Figure 4.45 Velocity vector around the wing with MLE at 18° with an airspeed of 20 m/s and (a) angle of attack 0°, (b) angle of attack 10°, and (c) angle of attack 18°112

Figure 4.46	Velocity streamlines for an angle of attack of 8° and the MTE at 18°	113
Figure 5.1	NACA0012 and NACA4412 airfoil superimposed	121
Figure 5.2	Drag coefficient variation with the lift coefficient for NACA0012 (grey) and NACA4412 (black). For $CL = 0.367$, angle of attack of NACA0012 = 7.8° and angle of attack of NACA4412 = 2.97°	121
Figure 5.3	MLE tip maximum displacement of 0.333 in (8.46 mm)	124
Figure 5.4	MTE tip displacement of 1.01 in (25.65 mm) for a 10° rotation of servomotor	124
Figure 5.5	MTE system	125
Figure 5.6	MLE system	126
Figure 5.7	MC system	126
Figure 5.8	MC system internal assembly	127
Figure 5.9	Morphing ribs place in the manufacturing guide	128
Figure 5.10	Central section of the wing corresponding to the MC system	129
Figure 5.11	Leading edge mold	129
Figure 5.12	Price - Païdoussis subsonic wind tunnel of LARCASE	130
Figure 5.13	Dimensions of the Price - Païdoussis subsonic wind tunnel	130
Figure 5.14	Dimension of the test chamber of the wind tunnel	131
Figure 5.15	Aerodynamic loading scales	132
Figure 5.16	Drag coefficient variation with the angle of attack	133
Figure 5.17	Lift coefficient variation with the angle of attack	133
Figure 5.18	Lift on drag ratio variation with the angle of attack	134
Figure 5.19	Lift coefficient variation with the angle of attack around the stall angle	135

Figure 5.20	Drag coefficient variation with the lift coefficient variation	136
Figure 5.21	Lift coefficient variation curve with the angle of attack.....	139
Figure 5.22	Induce drag coefficient variation with the angle of attack.....	141
Figure 5.23	Equation of drag coefficient variation with angle of attack.....	142
Figure 5.24	Skin friction drag variation with the angle of attack.....	142
Figure 5.25	Lift coefficient variation with angle of attack for the UAS-S4 wing	145
Figure 5.26	Lift coefficient variation with angle of attack for UAS-S4 (wing + fuselage)	145
Figure 5.27	Drag coefficient variation with the angle of attack for UAS-S4	146
Figure 5.28	Drag coefficient variation with the lift coefficient for the UAS-S4	147
Figure 5.29	Drag coefficient variation with the lift coefficient for UAS-S4 (zoom).....	147
Figure 6.1	Shapes of NACA0012, NACA4411, NACA4412 and MLE.....	152
Figure 6.2	Lift coefficient variation with the angle of attack (theoretical using XFLR5 code)	153
Figure 6.3	Drag coefficient variation with the angle of attack (theoretical)	154
Figure 6.4	Shape of UAS-S4 Ehécatl wing airfoil and morphed airfoil	155

LIST OF ABBREVIATIONS

AIAA	American Institute of Aeronautics and Astronautics
CASI	Canadian Aeronautics and Space Institute
CFD	Computational Fluid Dynamics
CIRA	Italian Center for Aerospace Research
CRIAQ	Consortium for Research and Innovation in Aerospace in Quebec
ÉTS	École de technologie supérieure
F/T	Force and Torque
LARCASE	Laboratory of Research in Active Controls, Avionics and AeroServoElasticity
LE	Leading Edge
LLT	Lifting Line Theory
L/D	Lift on Drag
MCS	Morphing Camber System
MDO	Multidisciplinary Design Optimization
MLE	Morphing Leading Edge
MTE	Morphing Trailing Edge
NACA	National Advisory Committee for Aeronautics
NRC-IAR	National Research Council - Institute for Aerospace Research
NSERC	Natural Sciences and Engineering Research Council of Canada
AWACS	Airborne Warning and Control System
SMA	Smart Material Actuators
UAS	Unmanned Aerial Systems

XXIV

UAV Unmanned Aerial Vehicle

VLM Vortices Lattice Method

LIST OF SYMBOLS

BASIC UNIT

m meter (unit length)
 A Ampere (unit of electric current intensity)

Area

m² square meter

GEOMETRIC UNIT

Length
 International System
 km kilometer
 mm millimeter

Imperial System
 in inch (= 0.0254 m)
 ft feet (= 12 in)

MASS UNIT

Mass
 International System
 g gram
 kg kilogram

Imperial
 lb pound (= 0,453 kg)

Density
 kg/m³ kilogram per cubic meter

MECHANICAL UNIT

Speed
 International System
 m/s meter per second
 km/h kilometer per hour
 steps/sec step motor per second

Imperial
 kn knot (= 1.852 km/h)
 ft/s feet per second (= 0,3048 m/s)
 RPM round per minute

Acceleration
 step motor for second square

Angle plan
 ° degree
 rad radian
 steps step motor

Viscosity
 Kg/(m.s) kilogram per meter-second

Forces
 International System
 N newton (= 1 kg.m/s²)

Moment
 International System
 Nm newton meter
 kg.cm kilogram centimeter
 kg/cm kilogram per centimeter

Imperial
 lbf-in pound-force inch (= 0,1129848 Nm)
 oz/in once per inch

Imperial
 lbf pound-force (= 4,44822 N)

TIME UNIT

h hour

ELECTRIC UNIT

Electric current voltage
 V volts

Current intensity
 mA milliamperere
 mΩ milliohms

Inductance

mH millihenry

Diameter of an electric cable

AWG American Wire Gauge

Electric power

W watt

mW milliwatt

kW kilowatt

Heat unit

°C degree Celsius

INTRODUCTION

This thesis presents research results obtained for the development of a morphing camber system for an UAV wing. The different steps to achieve this morphing system are described through three papers published in scientific journals. These papers describe the design, manufacturing and the experimental tests carried out using the morphing. By this design, the morphing system presented can be improved in order to make it more efficient but also to be used in the design of UAV by the reader of this thesis, or by the published papers within the framework of this thesis.

0.1 UAS-S4 Ehécatl – study aircraft

The Unmanned Aerial System (UAS) S4 Ehécatl is an autonomous flight system, that includes an onboard camera, an autopilot and the sensors necessary for its operation. The UAS-S4 Ehécatl model was developed in Mexico by Hydra Technologies in 2002 and made its first flight in 2006. UAS-S4 Ehécatl is used by the Mexican Army and Police. As part of the research developed at the research laboratory in active control, avionics and aeroservoelasticity (LARCASE), new methods of analysis, design and manufacturing applied to morphing wings, were developed. The main parameters of the UAS-S4 Ehécatl are as follows:

Table 0.1 Characteristics of UAS S4 Ehécatl

Span	12 pi 2 po (3.7 m)
Maximum takeoff weight	120 lb (54.43 kg)
Maximum speed	90 kn (167 km/h)
Cruise speed	38 kn (70 km/h)
Autonomy	8 h

Figure 0.1 shows the UAS-S4 Ehécatl from the LARCASE laboratory. This version is used to take accurate measurements of the UAS-S4 Ehécatl to perform structural and aerodynamic analyses. Another UAS-S4 identical version is kept in Mexico, and it will be used for its flight tests.



Figure 0.1 UAS-S4 Ehécatl of Hydra Technologies

0.2 Problematics

With its surveillance function, the UAS S4 Ehécatl performs irregular flights, for which, flight conditions change frequently and significantly. Two flight conditions prevail in the flight of the UAS: the "slow flight" which allows the UAS to observe the area, and the "fast flight" which allows the UAS to fly from one observation zone to another. In this thesis, the wind tunnel results were obtained at 20 m/s, which is the speed corresponding to the slow flight of the UAS.

For a classical UAS, the wing is fixed. An airfoil, and thus a wing shape were chosen, and thus considered during the design of the UAS. As the UAS flies through different phases (ascent, descent, cruising), a compromise is considered to obtain the best efficiency of the global flight. This compromise induces a loss of efficiency for the flight phases for which the

wing would not optimise. This loss of efficiency results in higher fuel consumption and / or a lower battery life.

The main problem currently area is the inability to change a wing airfoil from one theoretical airfoil to another. Current morphing systems do not experimentally allow the wing to achieve its desired form calculated theoretically using Computational Fluid Dynamics (CFD). The first problem is that the aerodynamic team must therefore work, and interact continuously with the structural team, because of the fact that the deformations obtained experimentally by the structural team must be analyzed by the aerodynamics team in order to quantify the aerodynamic performances. Therefore, an aero-structural optimized model will be design. It was found very difficult to obtain, from the experimental point of view, the structural deformations desired by the aerodynamic team initially.

The second problem is the mass of morphing systems that increase the weight of the UAS, because morphing wing systems generally need a more complex structure than a classical wing (more parts). If the morphing system did not replace or use actuators already present in the classical wing, it will give an additional weight for the wing. Thus, the gain obtained by the morphing system is lost by the weight of the system. We must also be able to solve this second problem.

The third problem concerns the consumption energy of the morphing system. The use of a morphing system aims to reduce to the power consumption due to the drag forces. But the use of the morphing wing system usually implied an energy consumption higher than that of a classical wing. In order to be used, the morphing system must imply an increase of the energy consumed lower than the reduction in the consumed power energy.

Thus, the originality of this new research in the field of morphing wings consists in the resolution of these three problems by used of new methodologies of aero-structural design, and by their experimental validation using the Price-Païdoussis subsonic blow down wind tunnel.

0.3 Objective

The objective of the research presented in this thesis is to design a mechanical morphing wing system that significantly modifies the wing airfoil. This significant deformation was defined by the ability of the system to change the shape of a wing using the NACA0012 airfoil to its shape using the NACA4412 airfoil (Figure 0.2).

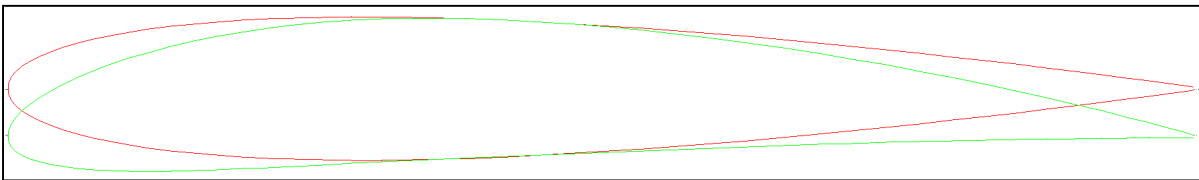


Figure 0.2 Airfoil NACA0012 (red) and airfoil NACA4412 (green) superimposed

A deformation defined in Figure 0.2 increases the lift as well as the drag of the wing. The lift increase allows the UAS to fly at a lower angle of attack, which reduces its drag. A morphing system will be considered “effective” if the drag reduction due to the reduction of the angle of attack is greater than the drag increase due to the deformation of the wing. As the lift required for an UAS depends on its flight case, the lift is considered fixed during the study of a flight case, so that we seek to reduce the corresponding drag.

As seen in the problematic section, morphing wing systems often have the disadvantage of increasing the mass of the UAS due to additional sensors and actuators. This increase in the mass of the UAS results in a higher lift needed to fly and therefore in an increase of the angle of attack of the UAS. This increase therefore counteracts the reduction of the angle of attack obtained due to the morphing wing system. Thus, an increase in the mass of the aircraft will therefore reduce the efficiency of the system or make it inefficient, that it would result in an increase in the drag of the UAS. A system must be designed that keeps constant the total mass of the UAS or minimizes the increase in its mass.

In addition to conserve the mass of the aircraft, the increase in electric current of the UAS must be minimized. Too much power consumption causes an increase in the fuel consumption of the UAS engine, which is equivalent to an increase in the total drag of the aircraft.

As a result of this airfoil change, an increase of the wing lift would have a lower impact on wing drag than with the deflection of an aileron. This change will allow us to reduce drag during turn and thus to reduce the effect of reverse roll a the UAS. In addition, the shape of the wing would be changed to adapt it to different flight conditions. In the “take-off acceleration” phase, reduced drag is needed so the NACA0012 airfoil will be appropriate. When the pilot decides to take-off, the airfoil used will be that of NACA4412 which will reduce the take-off distance and fuel consumption. Gradually during the flight of the UAS, the NACA4412 airfoil will change to NACA0012 airfoil. Therefore, it will be possible to save fuel during flight and take-off. When the UAS enters observation flight, the wing can take the shape of NACA4412 airfoil which will allow a slower flight, and thus obtain a better observation of the ground. For the first prototype, these standard airfoils will be used. We will adapt it to the profiles used by UAS-S4 thereafter.

To better understand the effectiveness of this research idea, the performance curves of both NACA0012 and NACA4412 airfoils are plotted using the XFLR5 code for Reynolds number of 150,000 to 600,000. The performance curves shown in Figure 0.3 the variations of the lift and drag coefficients as functions of the angle of attack.

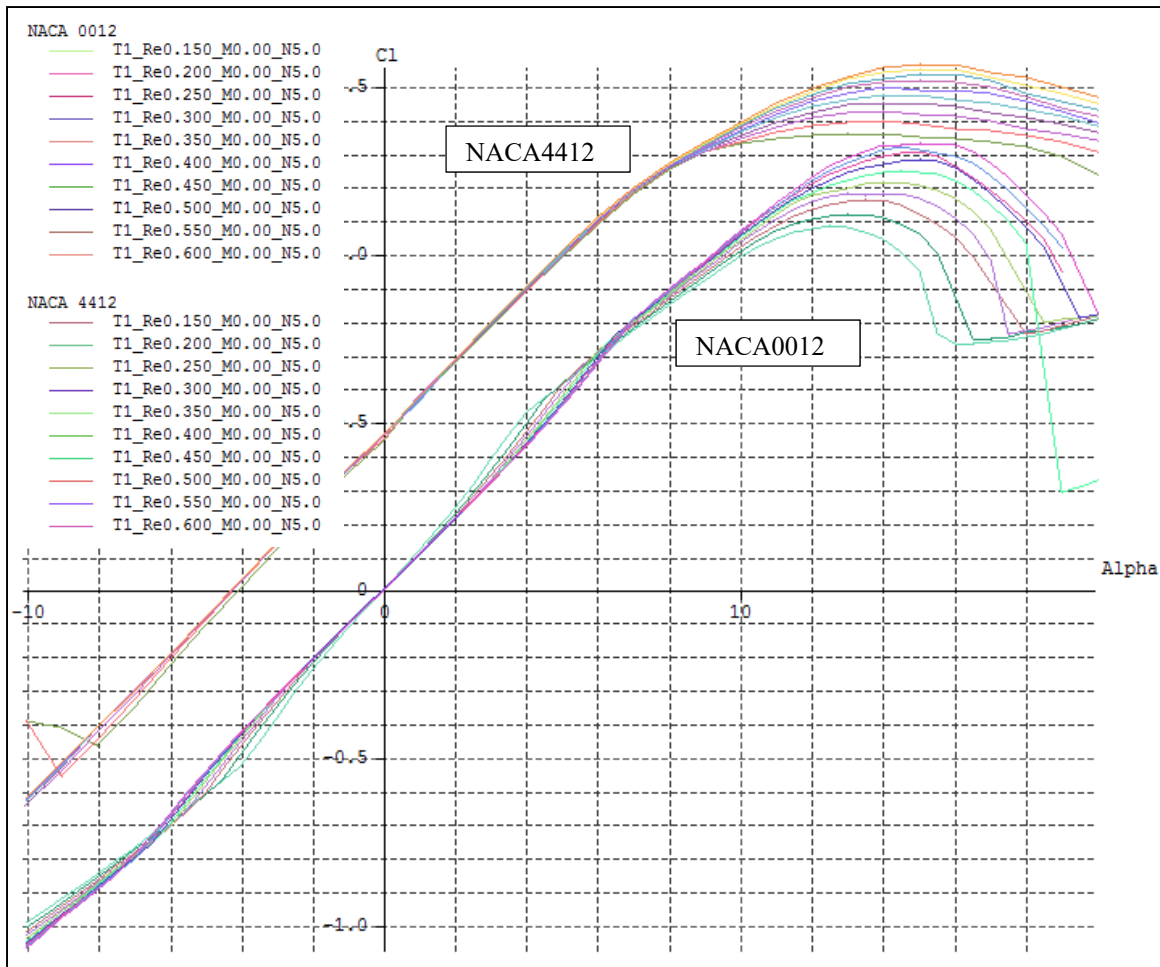


Figure 0.3 Lift coefficient variation with the angle of attack for NACA0012 and NACA4412 airfoil for Reynolds numbers of 150,000 to 600,000

The first observation is that the NACA4412 airfoil offers a gain of up to 0.5 on the lift coefficient. The two curves are parallel on their linear part (straight lines) and the stall angle of attack for the NACA4412 airfoil is higher than the stall angle for the NACA0012 airfoil.

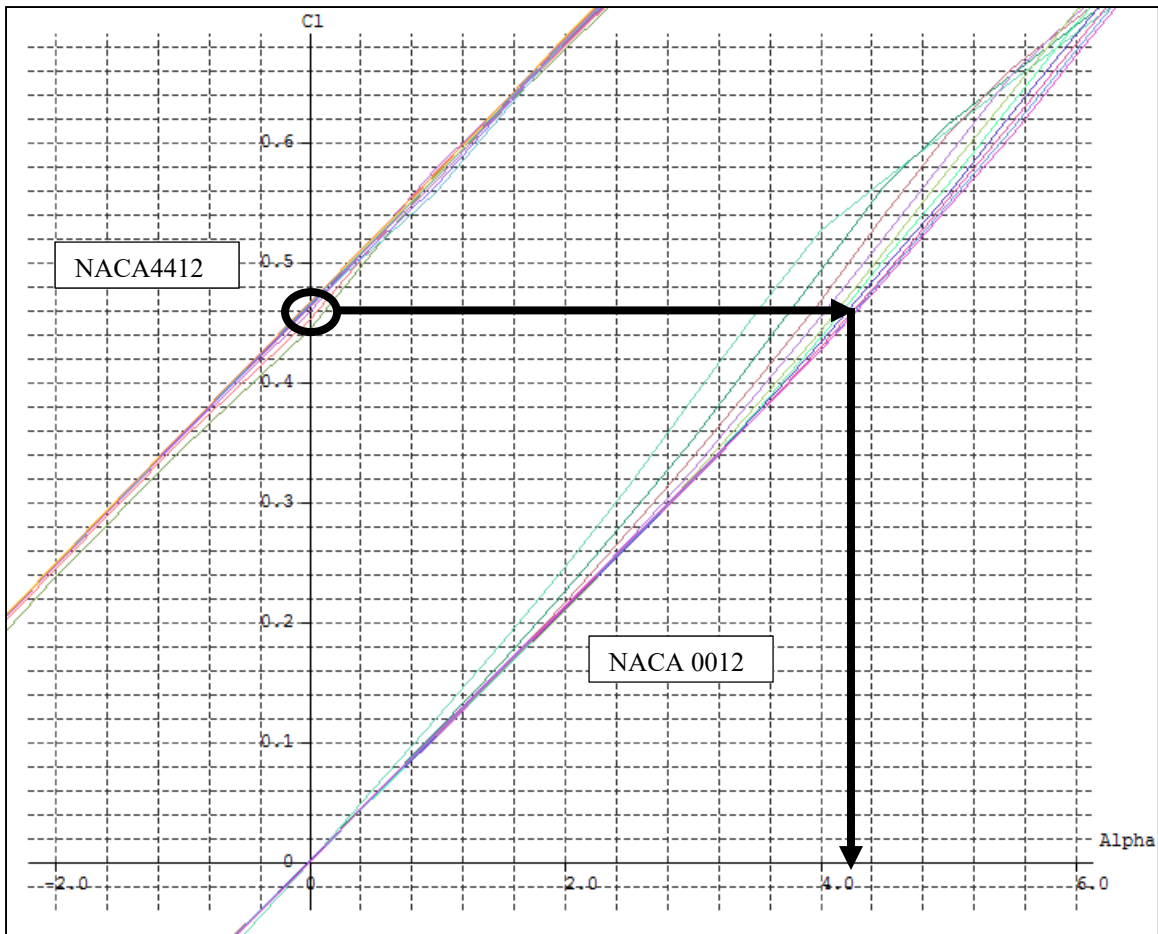


Figure 0.4 Zoom of lift coefficient variation with the angle of attack for NACA0012 and NACA4412 airfoils for Reynolds number from 150,000 to 600,000

In Figure 0.4, the lift coefficient of the NACA4412 airfoil is 0.46 for an angle of 0° . To obtain the same coefficient with the NACA0012 airfoil, the angle of attack should be 4° . Which means that by changing the shape of the wing from NACA0012 airfoil to NACA4412 airfoil, the angle of attack of the UAS could be reduce by 4° .

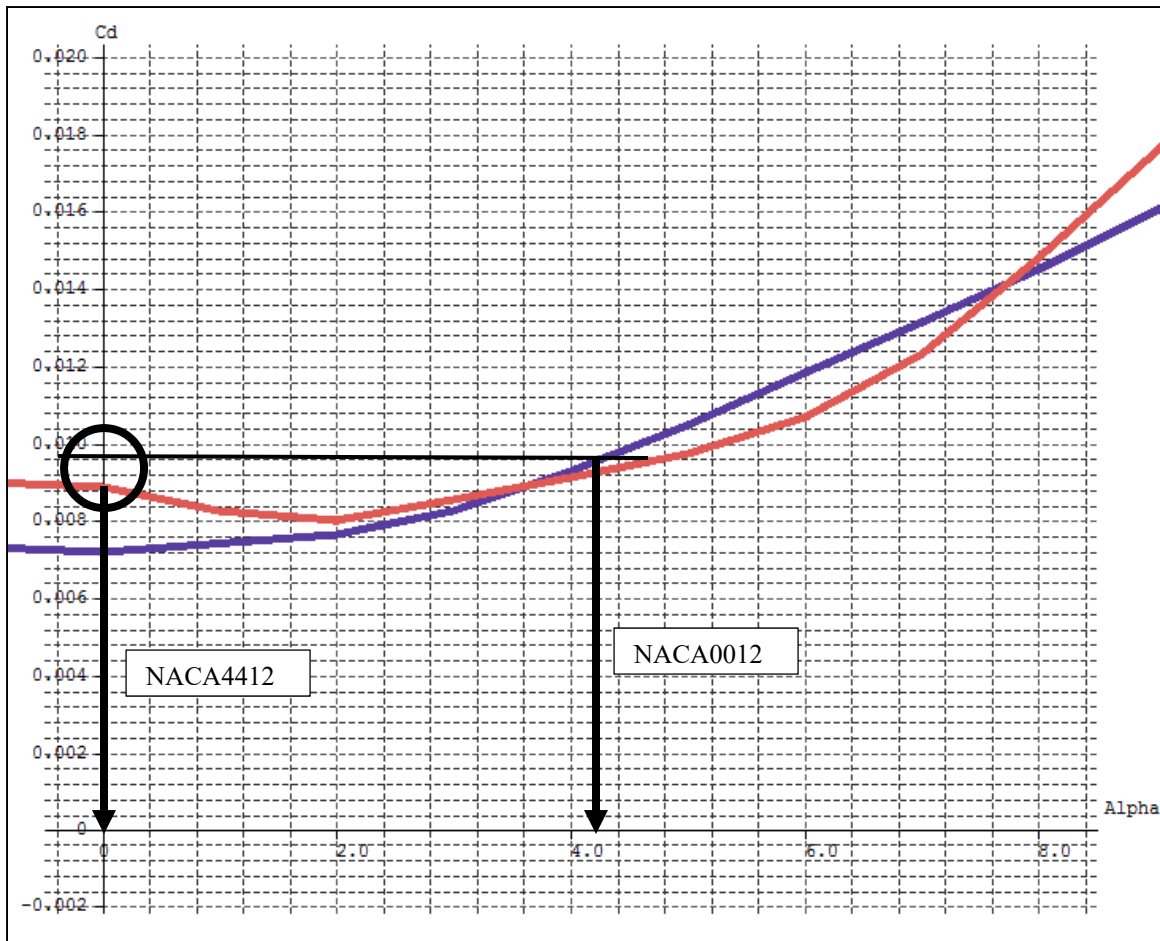


Figure 0.5 Drag coefficient variation with the angle of attack for the NACA4412 airfoil (red) and for the NACA0012 airfoil (blue) at a Reynolds number of 500,000

The drag coefficient of the NACA4412 airfoil for the angle of attack of 0° is 0.0088 at the Reynolds number of 500 000. The drag coefficient of the NACA0012 airfoil for an angle of attack of 4° is 0.0092 at the Reynolds number of 500 000. We see a 4% gain on the drag coefficient. By changing the shape of the wing airfoil, we can increase the lift of the wing with a smaller influence on the drag than if only the angle of attack of the wing is changed. In an hypothetical case where we would need a 4° angle of attack to take-off using a NACA0012 airfoil, it will be possible to take-off without changing the angle of attack but only by changing NACA0012 airfoil shape into NACA4412 airfoil. However, the drag coefficient of the NACA4412 airfoil at 0° is smaller than the drag coefficient of the

NACA0012 airfoil at 4° angle of attack, therefore a gain on the drag coefficient of the airfoil can be obtained during the take-off. A gain from the reduction of the angle of attack of the other part of the UAS (fuselage, empennage, ...) can be added to the gain obtained from the wing. This example illustrates the potential gain of such a system during the take-off phase, in which its impact will be a shorter take-off phase and a lower fuel consumption.

0.4 Methodology

0.4.1 Main Steps

The work methodology is broken down into the following six main steps (Figure 0.6). At the end of each step, a selection process is carried out to refine our list of possible solutions defined in the first step of the following methodology described in Figure 0.6. At the end of step 5, one single solution will be retained in order to implement it in the structure of the UAS-S4 in the step 6.

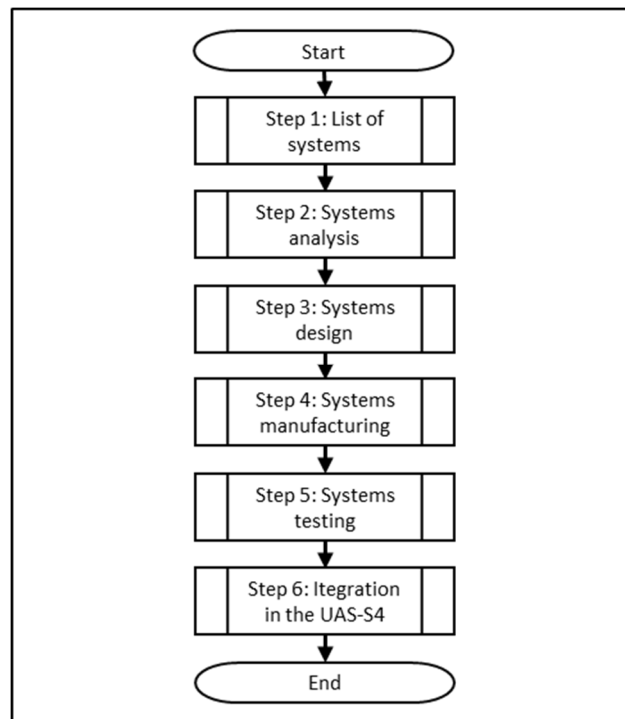


Figure 0.6 Methodology's main steps

The first step of this research (Figure 0.7) consists in studying the existing morphing systems. Teams from our laboratory and from other labs are also researching morphing wings. Therefore, to accelerate our research, we have analyzed the works and conclusions of other laboratories on other morphing systems to determine if these systems were working in accordance with our objectives. From these studies, we were able to establish in step one a list of morphing systems, as seen in Figure 0.7.

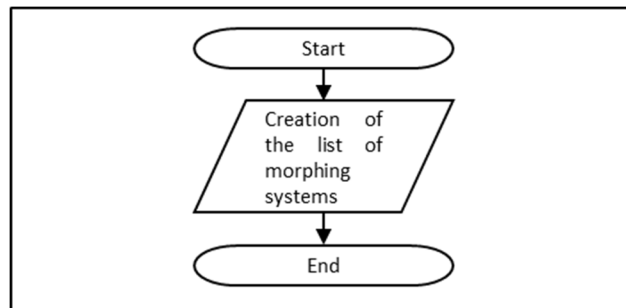


Figure 0.7 Step 1: List of systems

During second step, different morphing systems were compared from the list defined in the first step. The two main criteria of this comparison were the feasibility and the effectiveness of the solution. As shown in Figure 0.8, the feasibility was determined by the possibility of manufacturing the system, so that it would fit into the wing of the UAS-S4 Ehécatl while its effectiveness was determined by its positive influence on the aerodynamic performance of the wing. Our goal was to achieve a lower drag with the morphing system than with the actual classical system of the UAS-S4.

The UAS-S4 has a certain wing configuration and therefore some morphing systems can not be applied on it because of the fact that the space is too small in this configuration. As mentioned above, the existing studied morphing systems do not all have the same objectives, and therefore their effectiveness in our research is not guaranteed. We need to analyze which surface of the wing is morphing and how it affects the UAS-S4 aerodynamic performance. Thus, the advantages and disadvantages of these analyses are determined.

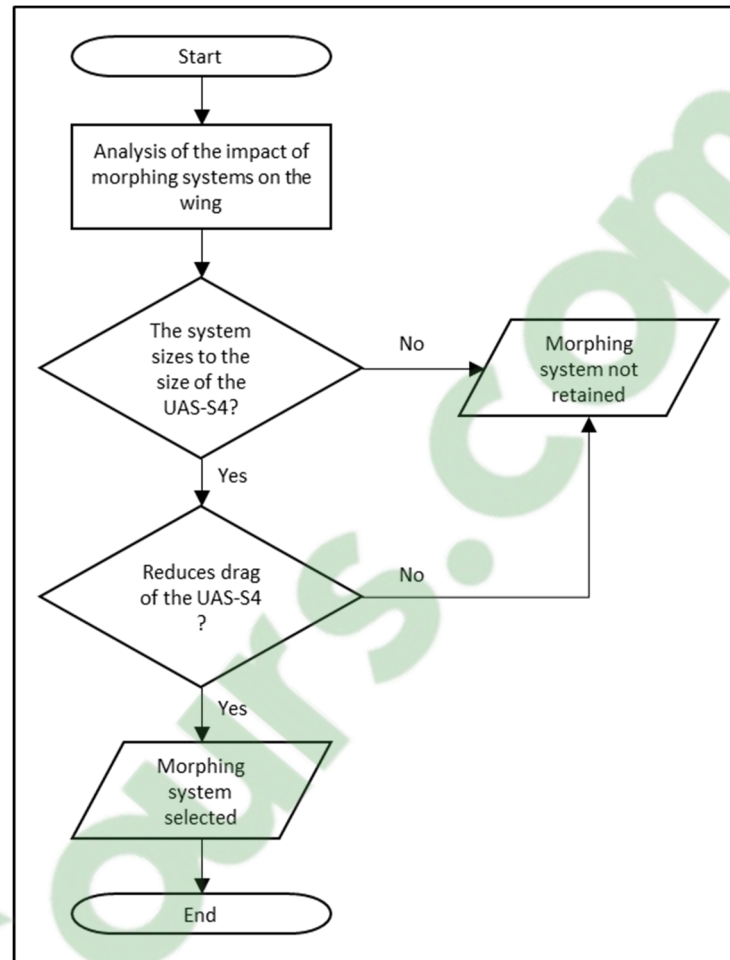


Figure 0.8 Step 2: Systems analysis

The third step consists in the selection of the best solutions for our application, and thus in further studies of these solutions. In Figure 0.9, it is shown that each selected solution must be designed it into a morphing wing system. This step is the most difficult because of the fact that the mechanical problems related to an experimental morphing system should be solved in the design phase. Such a problem would be the existence of waves on the surface of the wing during its deformation. These waves would be caused by the interaction of the structure with actuators, if these actuators would be punctually distributed.

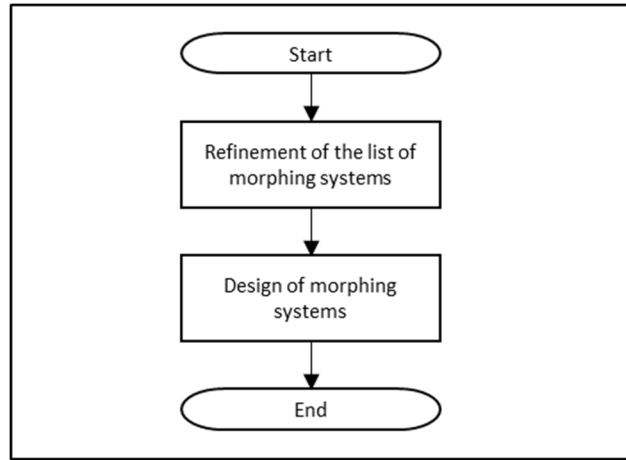


Figure 0.9 Step 3: Systems design

The fourth step is the manufacturing of the selected systems. To compare the effects of these systems on morphing wings, these morphing wings will be equipped with different systems, and further manufactured. These tasks are shown in Figure 0.10.

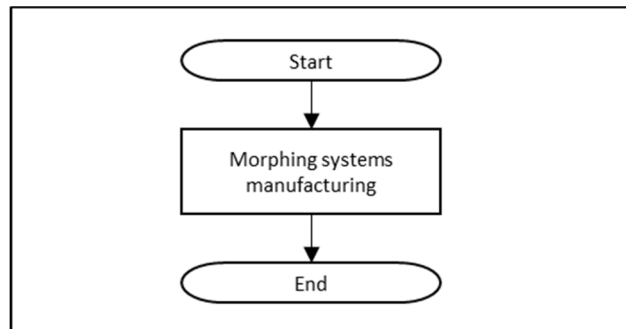


Figure 0.10 Step 4: Systems manufacturing

During the fifth step (Figure 0.11), the wind tunnel tests of morphing wings will be performed and the results obtained as function of aerodynamic performance will be analyzed. The flow of air will be simulated around the morphing wing and the aerodynamic forces will be calculated and compared with those obtained during wind tunnel tests.

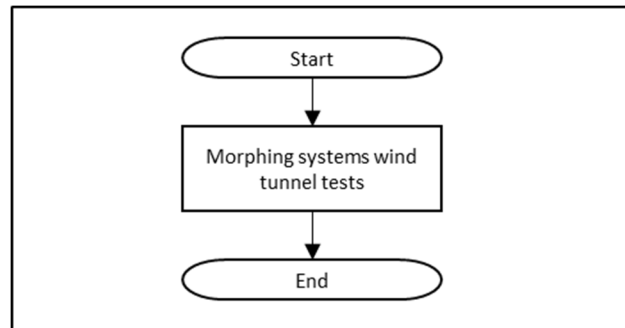


Figure 0.11 Step 5: Systems wind tunnel testing

The sixth and final step (Figure 0.12) will, based on the experimental results, select the most effective morphing system with respect to our drag reduction objective, and would integrate it into the wing of the UAS-S4.

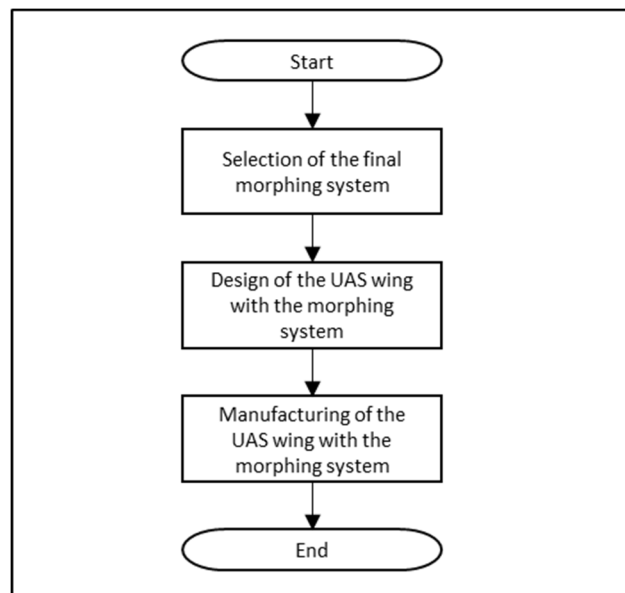


Figure 0.12 Step 6: Integration in the UAS-S4

The design and manufacturing of the morphing wing systems will be detailed in the following subsections.

0.4.2 Design phases of a morphing wing system

In order to realize the design of a morphing system, three phases are chosen. The first phase consists in a study of the morphing system influence on the aerodynamic performance of the wing. During this step, the type of aerodynamic performance improvement is determined for the wing, and thus the effective position of the morphing system in the wing. This "effective position" will be obtained following the displacement of the morphing system with respect to the chord and to the calculation of the aerodynamic coefficients on the morphing wing. The most effective position will be the one for which the lift on drag (L/D) ratio will be the highest. The aerodynamic coefficients calculations will be performed using well known software such as Xfoil, Fluent, etc. XFOIL is an open source code that calculates the aerodynamic performance of a wing airfoil (2D), and it has the advantage of its easy integration into an optimization code (Gabor, Koreanschi, & Botez, 2012). Fluent is an Ansys tool that calculates the aerodynamic coefficients of a 3D flow around the wing.

During the second phase, a design of the system was made, located in the area of the wing obtained during the first step. From this design, the possible structural deformation of the wing was determined using Finite Element Analysis (FEA) (Nastran, Hyperworks, CATIA V5). During this phase, the positions of the actuators, were determined.

During the third phase, an aerodynamic analysis of the wing was performed by use of the deformation obtained previously using either the "3D Panels" calculation method in XFLR5 code or the FEA in Fluent-Ansys. XFLR5 is an "open source" software that is used for aerodynamic calculations on aircraft (Fraqueiro, Albuquerque, & Gamboa, 2016) (wings, horizontal and vertical stabilizer and fuselage), as well as for the aircraft stability. It allows the user to perform an aerodynamic analysis of the aircraft according to three methods of calculation: Lifting Line Theory (LLT) (Phillips & Snyder, 2000), Vortex Lattice Method (VLM) (Konstadinopoulos, Thrasher, Mook, Nayfeh, & Watson, 1985) and 3D Panels (Katz & Plotkin, 2001).

The numerical results were validated by wind tunnel tests on the morphing wings. These morphing wings will have the same dimensions as the reference wing (Figure 0.13), and will allow us to compare the impact of the system on the morphing wing with respect to its impact on same wing without actuating system (or reference wing). The reference wing has the NACA0012 airfoil with a 10 in chord, and a 11.5 in wingspan. The 10 in chord was chosen following the ATR42 test wing project, in which a 10 in chord was also chosen ((Ben Mosbah, Botez, & Dao, 2014), (Ben Mosbah, Botez, & Dao, 2016)). The wingspan is 12 in, which is half of the height of the test chamber, but 0.5 in are embedded in the wing base, that attaches the model to the aerodynamic loading scales. This is the reason why the analysis is done on a wing with a span of 11.5 in.

The initial objective of the reference wing described above was to validate the operation of our new aerodynamic loading scales by comparing the measured values with the numerical values of the loads (forces and moments). Figure 0.13 and Figure 0.14 show the dimensions of the reference wing. In Figure 0.13, the chord of the wing is 10 in, the span of the wing is 11.5 in, the diameter of the wing base is 10.7 in and the thickness of the wing base is 0.5 in. In Figure 0.14, it can be seen that the shape of the wing base is circular while the airfoil of the wing is NACA0012.

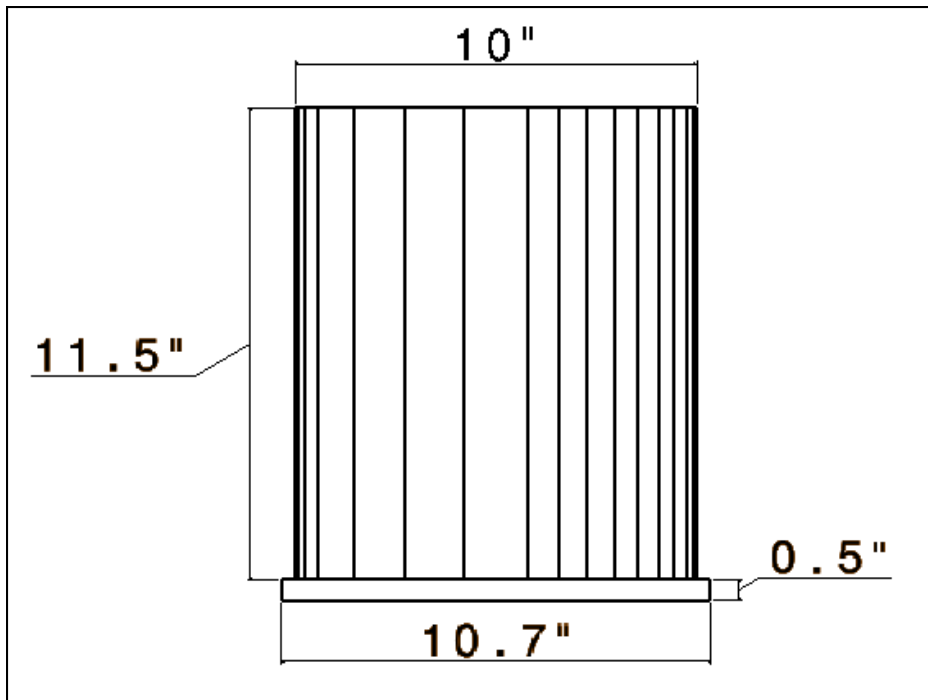


Figure 0.13 Side view of the reference wing

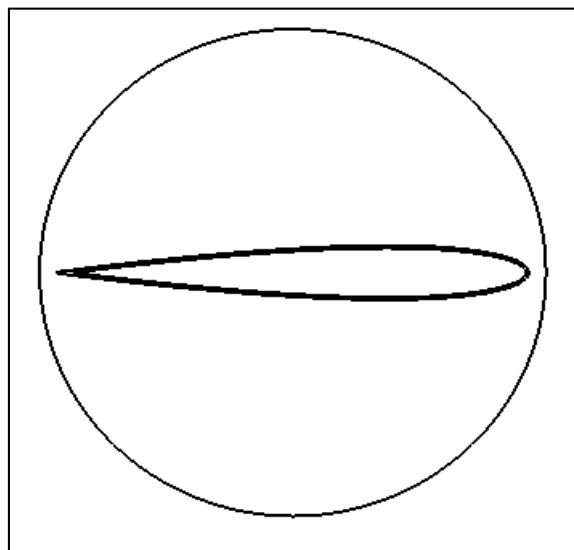


Figure 0.14 Top view of the reference wing

Wind tunnel tests were conducted on this reference wing as part of my Master's thesis (Communier, 2015). The experimental aerodynamic performance was validated by its comparison with the numerical values calculated by use of XFLR5 software. Figure 0.15 to

Figure 0.17 show the experimental wind tunnel tests results obtained for wing with respect to the numerical results. These results were expressed as function of lift coefficient and drag coefficient. The tests were conducted in a rectangular section chamber (2 ft per 4 ft) at flow speeds of 20 m/s, 25 m/s, 30 m/s, and 35 m/s. The angle of attack of the wing varied from -10° to 20° in intervals of 1° . The measurements were made by an aerodynamic loading scales including a Mini45-E transducer from ATI Industrial Automation. This aerodynamic loading scales was designed by the LARCASE team. The theoretical values of the reference wing were calculated using the XFLR5 code for a wing of a span of 11.5 in and a 10 in chord by the "3D Panels" calculation method of XFLR5. As our wing in the wind tunnel is in contact with the floor of the test chamber, this contact is simulated by a symmetry of the wingspan considered in the XFLR5 software. Therefore, the wing has a total span of 23 in. Figure 0.15 shows the variation of the measured versus calculated drag coefficients of the wing with the angle of attack.

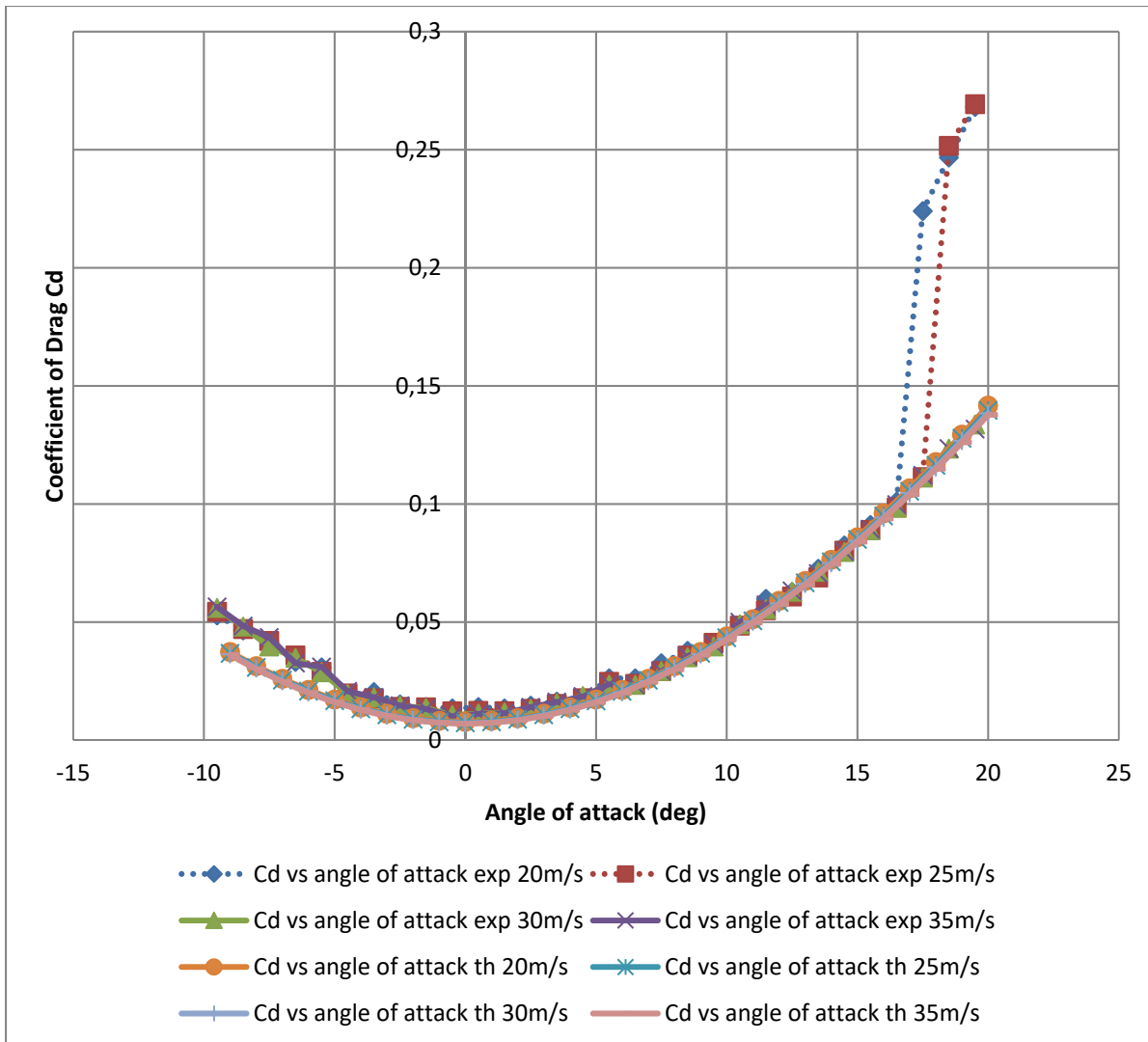


Figure 0.15 Variation of the drag coefficient with the angle of attack measured in the wind tunnel and calculated theoretically

In Figure 0.15, the curves of variation of the drag coefficient with the angle of attack are superimposed for positive angles of attack, but a slight asymmetry is observed for the negative angles. These results include a correction coefficient presented in equation (0.1) and detailed in the Master's thesis (Communier, 2015), as well as in the AIAA conference paper (Communier, Flores Salinas, Carranza Moyao, & Botez, 2015). This coefficient is composed of a static part and a dynamic one. The static part result from the contact surface between the aerodynamic loading scales base and the air flow. The dynamic part varies with the angle of

the wing and the speed of the air flow. This dynamic part was determined by measurements. According to the aerodynamics coefficients computation theory at low speed, the aerodynamic coefficient is constant as a function of the speed. However, in the measurements, a divergence of the drag coefficient was observed as a function of the speed. By using a subtraction of the drag coefficients curves between them, it was possible to determine proportionality between the divergence and the air flow speed, as well as between the angle of attack (α) and the air flow speed (v).

$$\begin{cases} \text{If } v \leq 20 \text{ m/s Then correction} = 0.022 \\ \text{Else correction} = (-0.00012 \times |\alpha| + 0.0003) \times (v - 20) + 0.022 \end{cases} \quad (0.1)$$

Figure 0.16 shows the variation of the lift coefficient of the wing with the angle of attack. A small difference between the lift coefficient calculated and the lift coefficients experimentally determined was found at angles greater than 15° , thus close to stall. This difference is explained by a loss of precision in the calculations for stall condition (high angle of attack).

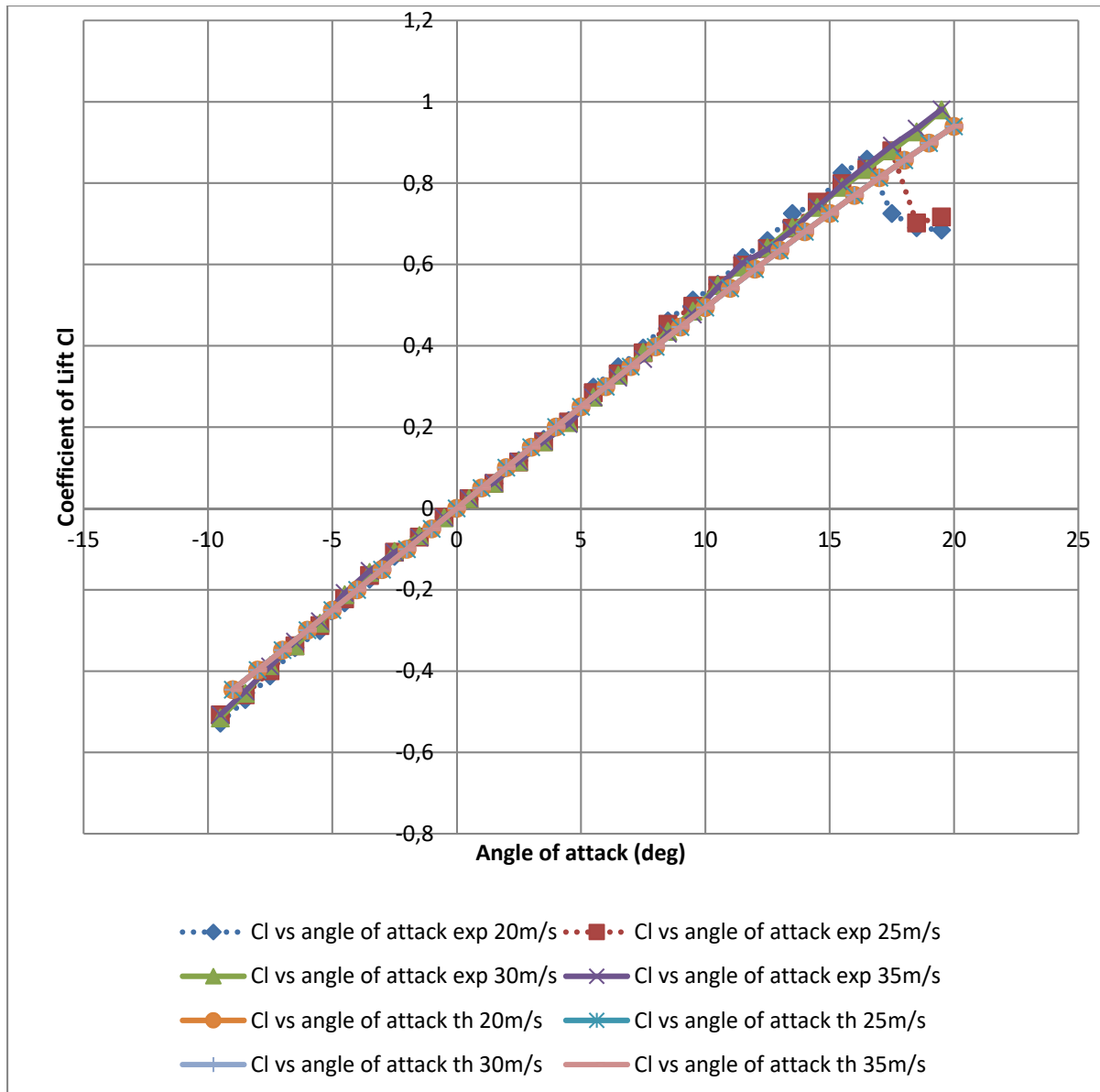


Figure 0.16 Variation of the lift coefficient with the angle of attack measured in the wind tunnel and calculated theoretically

The theoretical pitch coefficients were calculated at 25% of the chord while their experimental measurements are performed at 50% of the chord. This position of 50% of the chord came from the position of the sensor that is placed in the center of the aerodynamic scales and the wing is centered on the aerodynamic scale. Therefore, we carried out a conversion to find the equivalent measured values to 25% of the chord. This conversion was

given by a simplified equation (equation (0.2)), so differences exist for angles of attack below 1° and over 11° between the results obtained by calculation, and by wind tunnel tests (Figure 0.17). In equation (0.2), $C_{M_{1/4}}$ represents the pitch coefficient at 25% of the chord, $C_{M_{1/2}}$ represents the pitch coefficient at 50% of the chord and C_l represents the lift coefficient.

$$C_{M_{1/4}} = C_{M_{1/2}} + \frac{\text{chord}}{4} \times C_l \quad (0.2)$$

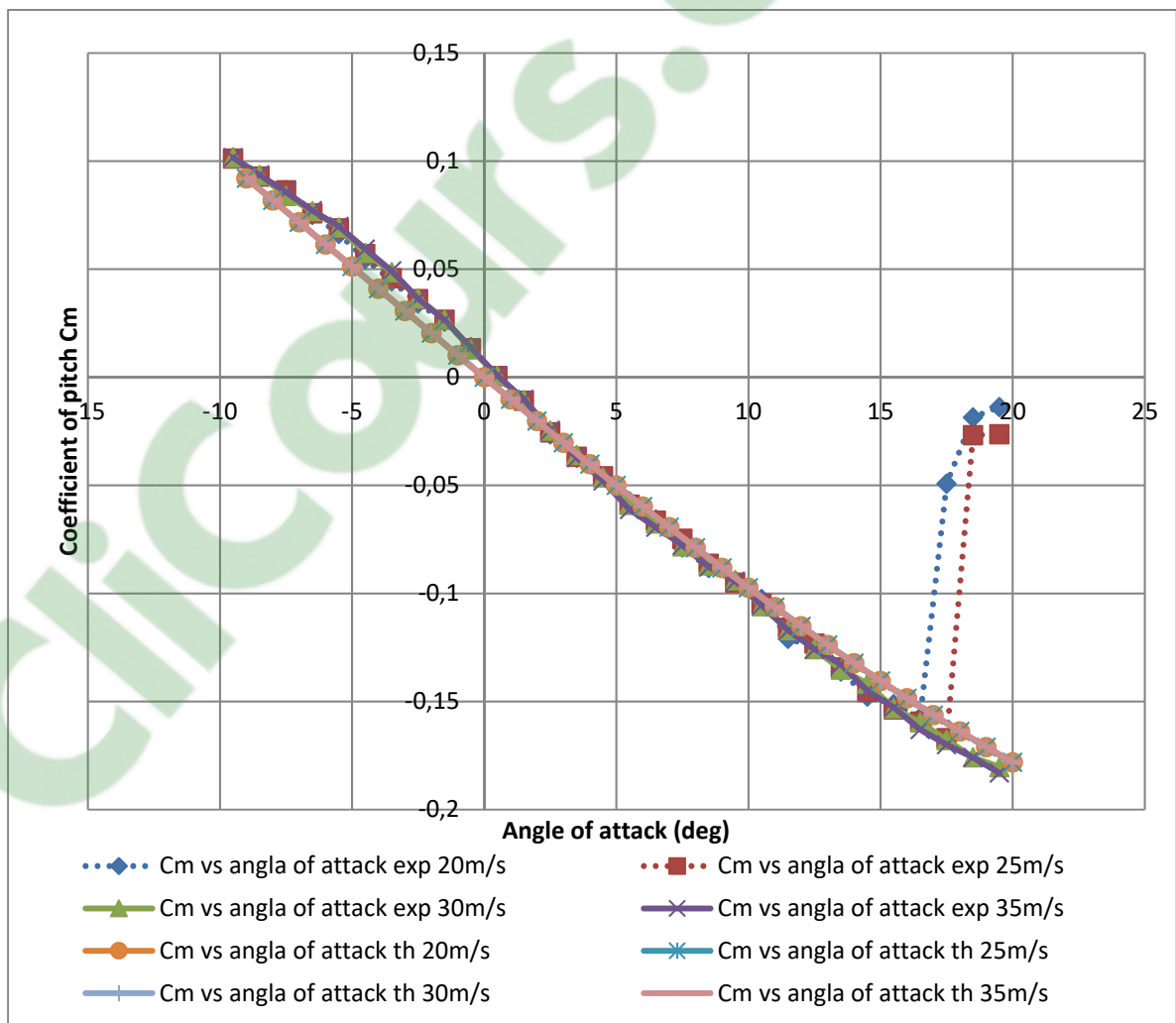


Figure 0.17 Variation of the pitch coefficient with the angle of attack measured in the wind tunnel and calculated theoretically

0.5 Conclusion

The morphing systems presented in this thesis were designed by taking account the UAS-S4 Ehécatl specifications. Therefore, the morphing systems had to give to the UAS the ability to switch between low speed and high-speed flights, and must have the proper size in order to fit in the wings of the UAS-S4 with a small weight and electrical consumption. Because of the fact that the work in this thesis aims to show the functionality of the morphing systems, and its advantages with respect to classical wing, the NACA0012 airfoil was used during the analysis. In order to give a focus on this research, the morphing systems had to change the NACA0012 airfoil shape to a new shape similar to the NACA4412 airfoil, the morphing wings tested must have the same size as the reference wings; the reference wing is a fixed wing which has a NACA0012 airfoil, and had been previously tested in the Price-Païdoussis wind tunnel of the LARCASE.

CHAPTER 1

LITERATURE REVIEW

This Chapter present the literature review about morphing wing which was done at the beginning of the work presented in this thesis. In first place, the previous work on morphing wing done by the LARCASE team will be presented. Then a summary of the work and the results obtained for several type of morphing wing will be presented. In order to get an extensive review of the previous work on morphing wing, the work of Barbarino (Barbarino, Bilgen, Ajaj, Friswell, & Inman, 2011), Sofla (Sofla, Meguid, Tan, & Yeo, 2010) and Weisshaar (Weisshaar, 2013) can be read.

1.1 Morphing wings at LARCASE at ÉTS

The study of morphing wings is not new to our laboratory (LARCASE). Indeed, the LARCASE team has already explored research and development paths for morphing wing technologies. This research was conducted in the frame of two major projects funded at the governmental level by the Consortium for Research and Innovation in Aerospace in Quebec (CRIAQ) and the Natural Sciences and Engineering Research Council of Canada (NSERC). These projects were carried out within the framework of agreements signed between university and industry partners. Each of these projects has led to the design and manufacture of prototypes and their tests in the National Research Council – Institute for Aerospace Research (NRC-IAR) wind tunnel, and to publications in scientific journals. These projects, entitled CRIAQ 7.1 and CRIAQ MDO 505 (where MDO stands for Multidisciplinary Design Optimization), were realized in collaboration with Bombardier, Thales, the NRC-IAR and École Polytechnique in Canada. In addition, the CRIAQ MDO 505 international project was realized in collaboration with Italian partners such as Alenia, the Italian Center for Aerospace Research (CIRA), University of Naples - Federico II. These two major projects carried out under the leadership of LARCASE aimed at morphing the upper surface of the wing in order to improve its aerodynamic performance.

The first project was called CRIAQ 7.1 (Popov, Grigorie, Botez, Mamou, & Mebarki, 2010). In this project, the morphing of the upper surface was done using Smart Material Actuators (SMA). The deformation obtained made it possible to delay the transition of the flow on the wing. In this project, an ideal rectangular wing was used, thus, no existing structural constraints for a real wing were considered. This concept has been validated using wind tunnel tests.

The second CRIAQ project was called CRIAQ MDO 505 (Koreanschi, et al., 2016). In this project, the goal was to design and validate a wing with an aileron, that was able to delay along the wing chord the flow transition from the laminar regime to the turbulent regime. For this aim, the wing was provided with four-point actuators in order for it to be able to morph. This wing was equipped with an aileron of a real Bombardier regional aircraft and presented the structural constraints. Experimental results have shown that this system composed of wing and aileron could produce the delay of the flow transition. However, irregular deformation of the wing and aileron surface appeared. Between the four-point actuators, the surface morphed did not had a quadratic form because of the structural constraint of the wing.

Another project was realized on a wing with the airfoil of an ATR42 (Regional Transport Aircraft). In this project, the upper surface of the wing was modified by using two oval bars. As they turned, the surface was pushed outwards (Sugar Gabor, Koreanschi, & Botez, 2012). This system therefore made it possible to morph the surface towards the outside but not towards the inside. Thus, aerodynamic performance gain of lift coefficient and drag coefficient was limited.

These morphing projects made it possible to optimize the laminar flow on the upper surface of the wing, but they were limited in order to modify the aerodynamic coefficients of lift and drag for the improvement of their performances. These morphing systems can not replace the control surfaces of the wing. From these three projects, we can conclude that in order to significantly improve the aerodynamic coefficients of lift and drag of a wing, the morphing

of the upper surface only was not enough. Thus, in the research proposed here, we will focus on the design and experimental validation of different types of morphing wing systems.

1.2 The different types of morphing wing

1.2.1 Wing aspect ratio

The aerodynamic coefficients improvement was made possible by modifying the span of the wing by using telescopic spars. A morphing prototype has been tested in the wind tunnel (Blondeau, Richerson, & Pines, 2003). The results analysis indicated that this morphing system made it possible to improve the lift and drag coefficients, however, this improvement was countered by the perturbation on the flow generated by the model. It was therefore necessary to obtain a significant increase in wingspan before perceiving a gain on the aerodynamic performance of the morphing wing. Following experimental tests, a 5 in extension in the span increase the drag coefficient of the wing while a 7 in extension in the span reduce it. This type of morphing was more effective in reducing the drag coefficient for angles of attack between 0° and 5° . From the structural point of view, this type of mechanism has been complex; there were three nested cylinders which involved a complex manufacturing and handling.

1.2.2 Morphing of the camber

The most promising type of morphing to meet our objectives will be the “morphing of the camber” of the airfoil (Sanders, Eastep, & Forster, 2003). Indeed, by modifying the camber of the airfoil, one could for example convert a NACA0012 airfoil into a NACA4412 airfoil, which would bring a significant increase in the lift coefficient of the wing, and a small drag coefficient increase. The National Advisory Committee for Aeronautics (NACA) airfoil, whose name includes two digits and a two-digit number, respect the following rule:

1. The first digit denotes the airfoil maximum camber as a percentage of chord;
2. The second digit gives the position of this maximum camber in ten percentage (10%) of chord;
3. The third number (last two digits) represents the thickness of the airfoil in % of the chord

Two types of deformations, combined together, make it possible to achieve this objective of deformation of the camber; the two types include the deformation of the leading edge and the deformation of the trailing edge (Gandhi & Anusonti-Inthra, 2008). However, a problem often encountered during the morphing of the shape of the airfoil is the appearance of waves on the wing surface due to interactions between the actuating system and the wing structure (Peel, Mejia, Narvaez, Thompson, & Lingala, 2009).

Another difficulty encountered in the development of morphing wing mechanism for UAS is the weight of the mechanism, and its size. The gains in aerodynamic coefficients (lift, drag) can therefore be canceled out by the additional weight of the mechanism. We must therefore be able to develop a mechanism that would improve the aerodynamic performances of the morphing wing without increasing its weight. Several morphing mechanisms have been studied in our project to achieve this objective.

1.2.2.1 Morphing wing using SMA

SMAs ((Elzey, Sofla, & Wadley, 2005), (Elzey, Sofla, & Wadley, 2003) and (Berton, 2006)) are materials that can change their size under the action of an electrical current and thus morph the surface of a wing. They have the advantage of being light enough, however they consume a lot of energy to work, thus, the energy saving goal is not respected (Fischer, Terriault, & Brailovski, 2012). Another method considered the acting on the surface directly by used of piezoelectric materials (Moosavian, Chae, Pankonien, Lee, & Inman, 2017), (Wang, Bartley-Cho, Martin, & Hallam, 2001). However, these materials required large electrical consumption.

1.2.2.2 Morphing wing using oval bars

The system with oval bars of the ATR-42 project made it possible to obtain uniform deformation of the upper surface along the wingspan, but it had the disadvantage of being heavy and bulky (Tchatchueng Kammege, Grigorie, Botez, & Korenschi, 2016). If the weight of the UAS was increased, there was the need to increase the angle of attack in order to carry the same payload. This increase in the angle of attack implied an increase in the UAS drag. Therefore, the fuel consumption of the UAS was increased, which was a high disadvantage of this proposed system.

1.2.2.3 Morphing wing using actuation points

The third deformation system, used in the CRIAQ MDO 505 project, consists of 4 actuators installed on the wing, that pushed or pulled its surface. These actuators provided a high force for a very low weight (Tchatchueng Kammege, Khan, Grigorie, & Botez, 2016). However, these actuators are suitable for a passenger aircraft wing but, they are too bulky to be installed in the UAS-S4 Ehécatl wing. In addition, the limited values of deformations were considered for each actuator (up to 5 mm). Measurements by LARCASE team with a 3D scanner showed that the deformation between two actuation points was not as linear as desired, small bumps were formed on the skin of the wing by the interaction between actuators and wing skin.

1.2.3 Morphing of the trailing edge

During the CRIAQ MDO 505 project, a morphing wing and aileron system was developed. The morphing aileron was able to operate an aileron using an arm that was rotated (Amendola, Dimino, Pecora, & Amoroso, 2015). This system allowed to change the shape of the aileron without external mechanisms to the aileron. Research in Germany has presented a concept of morphing trailing edge by use of ribs through an articulated skeleton (Monner, D., & Elmar J., 2000). This concept has shown that by use of this type of morphing, it was possible to

replace the ailerons at the wing tip, but this morphing alone was not enough to replace the flaps at the wing root.

Many research studies have been carried out on the morphing trailing edge by using different types of actuators (mechanical, piezoelectric, SMA). The mechanical deformations were mainly produced by using articulated ribs, such as “fingers” (Monner, Hanselka, & Breitbach, 1998), (Poosong, 2004) or by using a morphing structure (Kota, et al., 2003), (Shili, Wenjie, & Shujun, 2008) for compliant mechanisms of the trailing edge. These mechanisms made possible the control of the deformation of the structure, while the desired linear deformations were not obtained on the surface of the wing (wave formed on the surface). The actuators were generally heavy and bulky as they need to deform the wing structure.

1.2.4 Morphing of the leading edge

Several mechanisms were designed in order to morph the leading edge and have been studied in the literature ((Sodja, Martinez, Simpson, & De Breuker, 2015), (Rudenko, Radestock, & Monner, 2016), (Radestock, et al., 2016), (Takahashi, Yokozeki, & Hirano, 2016)). The systems that were tested in wind tunnel indicate that the deformation of the leading edge did not affect the values of the lift coefficients. This deformation could be used to delay the stall angle with less impact on the wing drag than a conventional slat, which was an important benefit.

1.2.5 Morphing with compliant mechanisms

By using compliant mechanisms, the main difficulty was to precisely morph the surface of a wing following a target curve. To achieve this objective, research on morphing wings using compliant mechanisms methods has been carried out (Kota, et al., 2003). This morphing method is still under study in laboratories. The main problem of this system is its ability to keep its position under external constraints (air pressure). For this reason, it is difficult to apply this method on real wing.

1.3 Design constraints

In order to continue to work on the analyses of various types of morphing systems, and on their influences on the wing, a new mechanism will be developed that will morph the trailing edge and the leading edge of the wing by maintaining a continuity in the camber of the airfoil. This structure should not increase the weight of the wing, but it must retain its rigidity to withstand the aerodynamic forces, and should not require a large additional energy consumption. In addition, a uniform deformation of the wing surface must be obtained. These restrictive design constraints are composing the complexity and originality of the development of the morphing wing mechanism.

CHAPTER 2

RESEARCH APPROACH AND THESIS ORGANIZATION

2.1 Research approach

The experimental research presented in this thesis consists in the validation of the assumptions (the morphing mechanism improves the performance of the aircraft) using wind tunnel tests. The first step of this experimental research consisted in the wing model developed with a NACA0012 airfoil which will serve as a reference for the study of wings with morphing systems. The aerodynamics results for the reference wing (numerical and experimental) has been validated as part of a Master project (Communier, 2015).

When a morphing method has been selected, a wing model incorporating the morphing system was designed and manufactured in order to validate its mechanical behavior, and its ability to morph according to the objective defined above, its NACA4412 airfoil.

Another wing model equipped with an aileron has been manufactured to serve as a reference for the performance of conventional UAS. This model made possible a comparison of the wing equipped with the morphing system against the wing with an aileron, and to determine which system (“conventional” or “morphing”) is the most effective from the point of view of the UAS drag reduction.

After the demonstration of functionality and efficiency, the next step was to adapt the morphing system to the leading edge of the wing. In this step, it is verified that the system fitted into a smaller space, (20% of the chord for the leading edge with respect to 40% of the chord for the trailing edge). In this step, the impact of a deformation of the leading edge on the aerodynamic performance of the wing was validated.

The last step was to manufacture a wing equipped with both morphing systems to validate that the two systems have the same behavior when they were separated, and when they were working together on the same wing.

2.2 Thesis organization

This thesis presents the three journal articles, published based on my research work, of which I am the main author, these papers have been shared with the scientific community. This research work was also presented in two conferences.

Professors Dr. Ruxandra Botez and Dr. Tony Wong are co-authors of all these articles, Professor Ruxandra Botez as Thesis Director and Professor. Tony Wong as Co-Thesis Director. They supervised all the work presented in this thesis. In the second article, Mr. Franck Le Besnerais is also co-author. The internship of Franck focused on the analysis of the morphing wing using Fluent-Ansys software. He participated in the section writing on the modeling of the morphing leading edge using Fluent-Ansys.

In CHAPTER 3, the article entitled “*Experimental validation of a new morphing trailing edge system using Price – Païdoussis wind tunnel tests*” was published in the peer-review journal Chinese Journal of Aeronautics in June 2019, Vol 32, Issue 6, p1353-1366.

This article presents the design of a wing equipped with a Morphing Trailing Edge (MTE) as well as its static and dynamic behaviors. It also presents a comparison of behavior of the MTE versus the behavior of an aileron. The results of this comparison show that for the same lift, the MTE generates less drag than the aileron.

In CHAPTER 4, the article entitled “*Design, Manufacturing and Testing of a New Concept of Morphing Leading Edge using a Subsonic Blow Down Wind Tunnel*” was published in the peer-review journal “Biomimetics”, Special issue on Morphing Aircraft Structures in December 2019, Vol 4, Issue 4, p 76.

This article presents the design of a wing equipped with a Morphing Leading Edge (MLE); the setup to allow the measurements of the forces on the wing during the wind tunnel tests, the results of the wind tunnel tests, and the modeling of the test wing with the MLE under Ansys-Fluent. The design of the MLE was made accordingly to the design of the MTE. As the results for the MTE were very good, the design was applied on the MLE, and it consisted of six slits along the chord as the MTE, but their size was adjusted for the leading edge. The results of this article show that the MLE allows the modification of the wing stall angle. In comparison to the first article, that presents a comparison between two models, the second article presents a comparison between the wind tunnel tests results obtained for the MLE design, and the CFD results obtained for the MLE design. This comparison had the aim to show that our design methodology allowed to the accurately modeling of the morphing wing system, by obtaining a good correlation between the experimental and the computed values.

In CHAPTER 5, the article entitled “*Design and Validation of a New Morphing Camber System by Testing in the Price – Païdoussis Subsonic Wind Tunnel*” was submitted in the peer-review journal “Aerospace”, Special issue on Design and Analysis of Wind-Tunnel Models and Fluidic Measurements in December 2019.

This article presents the design and manufacture of a wing equipped with a MLE and a MTE, that allow a complete morphing of the camber of the wing. The analysis of the MTE and of the aileron in the first article shows that the presence of the control surface on the wing degraded the stall angle of the wing. To counter this negative effect, the results presented in the second article are used, which show that the MLE allowed delaying the stall angle. The results of the wind tunnel tests of this morphing camber system (MCS) show that these two systems do not interfere with each other, and that their control could be decoupled. A discussion in this article presents a case study in which the MCS is integrated on the UAS-S4 Ehécatl wings from Hydra Technologies, and shows that the MCS reduces the drag of the UAS-S4.

As mentioned earlier, two conference articles were presented based on his work.

The first article, entitled « *Aero-structural analysis – Creation of a wing assembly with non-linear aerodynamic pressure distribution on its surface* » was presented at the CASI AERO17 conference. This article concerned the methodology used for the Finite Element Analysis (FEA) of morphing wing with Catia V5 by taking into account the distribution of pressures around the wing. This article presents an improvement of the Master thesis project by applying the distribution of pressure on a wing assembly instead on a single part wing.

The second article entitled "Rolling authority of a morphing trailing edge system design" was presented at the CASI AERO19 conference. In this article the analysis of the behavior of a wing, equipped with an MTE, in roll was studied. This article demonstrates that the MTE system allows the UAS to have roll control. This article follows a recommendation of a jury member when submitting the first paper article to the Chinese Journal of Aeronautics.

CHAPTER 3

EXPERIMENTAL VALIDATION OF A NEW MORPHING TRAILING EDGE SYSTEM USING PRICE – PAÏDOUSSIS WIND TUNNEL TESTS

D. Communier^a, R. M. Botez^b and T. Wong^c

^{a, b, c} Department of Systems Engineering, École de Technologie Supérieure,
1100 Notre-Dame West, Montreal, Quebec, Canada H3C 1K3

Paper published in *Chinese Journal of Aeronautics*, Vol. 32, No. 6, pp. 1353-1366, June 2019, DOI:10.1016/j.cja.2019.03.016

Résumé

Cet article présente la conception et la fabrication d'un nouveau système d'aile déformable réalisé au laboratoire de recherche en commande active, avionique et aéroserveoélasticité (LARCASE) de l'ÉTS à Montréal. Cette première version d'une aile déformable permet la déformation de son bord de fuite, dénommée *Morphing Trailing Edge* (MTE). Afin de caractériser l'impact technique de cette déformation, nous comparons ses performances avec celles d'un aileron rigide en utilisant des tests dans la soufflerie subsonique Price-Païdoussis du LARCASE. La première série de résultats montre qu'il est possible de remplacer un aileron par un MTE sur une aile, car une amélioration a été observée pour les performances aérodynamiques du MTE par rapport aux performances aérodynamiques de l'aileron. L'amélioration a consisté dans le fait que le coefficient de traînée était plus petit, et la finesse était plus élevée pour le même coefficient de portance.

Abstract

This paper presents the design and manufacturing of a new morphing wing system carried out at the Laboratory of Applied Research in Active Controls, Avionics and AeroServoElasticity (LARCASE) at the ETS in Montréal. This first version of a morphing wing allows the deformation of its trailing edge, denote by *Morphing Trailing Edge* (MTE). In order to characterize the technical impact of this deformation, we compare its performance with that of a rigid aileron by testing in the LARCASE's price—Païdoussis subsonic wind

tunnel. The first set of results shows that it is possible to replace an aileron by a MTE on a wing, as an improvement was observed for the MTE aerodynamic performances with respect to the aileron aerodynamic performances. The improvement consisted in the fact that the drag coefficient was smaller, and the lift-to-drag ratio was higher for the same lift coefficient.

3.1 Introduction

Due to its monitoring function, an Unmanned Aerial Vehicle (UAV) makes irregular flights, in which, the flight conditions change frequently and significantly. For a conventional aircraft, the surface of the wing is fixed. That is, airfoils representing wing shapes are chosen and utilized throughout the aircraft's design. As the aircraft passes through different flight phases (climb, descent, and cruise), a compromise is considered to obtain the best efficiency of the global flight. If this efficiency is compared to the optimal efficiency for each flight phase, the efficiency of each phase will be less optimal than the total efficiency. This loss of efficiency would result in higher fuel consumption and/or a shorter operating time. (Nemec, Zingg, & Pulliam, 2004) (Park, Han, Kim, & Lee, 2008) (Barbarino, Bilgen, Ajaj, Friswell, & Inman, 2011)).

The first objective is to modify the geometrical shape of the wing according to flight conditions with the aim to reach as much as possible its optimal shape for each flight condition. The morphing wing will be designed to increase its aerodynamic performance by increasing lift-drag ratio, which therefore would be equivalent to the increase of the lift and reduction of the drag. This fact will have the effect of reducing fuel consumption, increasing flight autonomy, etc.

The second objective is to keep the wing weight less than or equal to its current weight. To perform this objective, the structure of the current wing should be analyzed to establish its design criteria (weight, flexural strength and torsion, maximum permissible load), and to further design a new wing that meets these design criteria.

The morphing wings are studied at our Laboratory of Applied Research in Active Controls, Avionics and AeroServoElasticity (LARCASE) at the ETS since 2003. Indeed, this team has already explored numerous development strategies for morphing wing technologies. This research was carried out as part of two major projects of the Consortium of Research and Innovation in Aerospace in Quebec (CRIAQ). CRIAQ projects are carried out within the framework of signed agreements between universities, industrial partners and research institutes. Each of these projects has led to the designing and manufacturing of prototypes and their experimental wind tunnel tests, and to publications of results in scientific journals and conferences. These projects, CRIAQ 7.1 and CRIAQ MDO 505, were carried out in collaboration with Bombardier, Thales, NRC-IAR and École Polytechnique in Canada. In addition, the CRIAQ MDO 505 project was realized in collaboration with Italian partners, Alenia, CIRA, and the University of Naples—Frederico II. These two studies carried out under the leadership of LARCASE team aimed at deforming the upper surface of the morphing wing in order to improve its aerodynamic performance. The first project was called CRIAQ 7.1, in which the deformation of the upper surface was applied to a wing using “Smart Material Actuators” (SMA). (Popov, Grigorie, Botez, Mamou, & Mebarki, 2010) (Tchatchueng Kammegne, Grigorie, Botez, & Koreanschi, 2016). The resulting deformation made it possible to delay the flow transition on the wing. An ideal rectangular “wing” was used, and therefore no existing structural constraints for a real wing were considered. This concept was experimentally validated in the NRC-IAR wind tunnel. The second CRIAQ project was called the CRIAQ MDO 505 project, ((Koreanschi, et al., 2016), (Koreanschi, Sugar-Gabor, & Botez, 2016), (Michaud, Joncas, & Botez, 2013)), where MDO stands for “Multidisciplinary Design Optimization”. The objective was to design and validate a wing with an aileron. For that wing, it was necessary to move the passage of the air flow along the chord of the wing in order to delay the transition from the laminar to the turbulent flow. In order to perform this motion, the wing tip was equipped with four punctual actuators to change its aileron shape design for a real regional Bombardier aircraft that exhibited structural constraints. The experimental results showed that the system could produce the delay of the airflow transition. A subsequent project with an airfoil of an ATR 42 (Regional Transport Aircraft) made it possible to modify the morphing wing upper surface by means of

two oval spars. (Sugar Gabor, Koreanschi, & Botez, 2012). When those spars rotated, the surface was pushed outwards. This system therefore makes it possible to change the surface outward but not inward, and therefore the improvement of the aerodynamic performances was limited. These deformation methods allowed modification of the airflow, but they proved to be limited in modifying the coefficients values for aerodynamic performance improvement on the morphing ATR-42 wing (less than 5% for the lift and less than 2% for the drag (Koreanschi, Sugar-Gabor, & Botez, 2016)). From these three projects, in order to significantly improve the aerodynamic coefficients of a wing (Reich & Sanders, 2007) (for example, an increase of more than 50% of the lift with an increase of L/D ratio), the deformation of the upper surface alone was not sufficient. Therefore, in this work, the design and experimental validation of a morphing wing trailing edge system are analyzed.

Concerning the state of the art in wing morphing, we can refer to the work of Sofla, et al. (Sofla, Meguid, Tan, & Yeo, 2010)

3.2 Design of the Morphing Wing System

3.2.1 Deformation of the Camber

Studies have shown that the most promising type of deformation to meet this study objectives would be the deformation of an airfoil's camber (Sanders, Eastep, & Forster, 2003). Indeed, by modifying the camber of an airfoil, it could be possible, for example, to convert a NACA0012 airfoil into a NACA4412 airfoil, thereby attaining a significant increase of the lift of the wing while incurring a smaller increase of the drag, thus resulting in a higher L/D. National Advisory Committee for Aeronautics (NACA) airfoils, whose names consist of two digits and a two-digit number (convention for NACA airfoil with 4 digits), follow the following standard: the first digit denotes the maximum camber of the airfoil as a percentage of the chord; the second digit gives the position of this maximum camber in tens of percent of the chord; the third number (the last two digits) represents the thickness of the airfoil at a percentage of the chord (Jacobs, Ward, & Pinkerton, 1933).

Two types of deformations, combined together, made possible to change an airfoil's camber; and these deformations are: the deformation of the leading edge and the deformation of the trailing edge (Gandhi & Anusonti-Inthra, 2008). However, an often encountered problem when the shape of the airfoil deforms consists in the occurrence of waves on the surface of the wing due to the interactions between the actuating system and the wing structure (Peel, Mejia, Narvaez, Thompson, & Lingala, 2009).

Another difficulty encountered in the development of a morphing wing mechanism for reduced sized aircraft is its weight and its bulk. Any gain in aerodynamic performance (lift, drag) could thus be cancelled out by the additional weight of the mechanism. This is our motivation for developing a mechanism that can improve the aerodynamic performance of a morphing wing without increasing its weight.

3.2.2 Deformation of the Trailing Edge

A morphing aileron system was developed as part of the CRIAQ MDO 505 project (Amendola, Dimino, Pecora, & Amoroso, 2015). This system made it possible to operate an articulated aileron from an arm that was rotated, which allowed the shape of the aileron to be changed without the need for a mechanism external to the aileron. Research in Germany at Braunschweig presented a concept of the deformation of the ribs at the trailing edge of the wing using an articulated skeleton (Monner, D., & Elmar J., 2000). Their report concluded that using the deformation of the trailing edge, it would be possible to replace the ailerons at the end of the wing, but that this deformation alone would not be sufficient to replace the flaps on the wing.

Many research studies have been carried out on the morphing trailing edge, using different actuators types (mechanical, piezoelectric, smart materials actuators). The mechanical deformations were mainly done using articulated ribs like fingers (Monner, Hanselka, & Breitbach, 1998), (Poonsong, 2004) or using a morphing structure (Kota, et al., 2003), (Shili, Wenjie, & Shujun, 2008) (compliant mechanisms). These mechanisms made possible to

control the deformation of the structure, but the surface of the wing did not completely respect the desired deformations (wave formations on the surface). In addition, the necessary actuators were often heavy and bulky. The use of smart material actuators (Elzey, Sofla, & Wadley, 2003), (Elzey, Sofla, & Wadley, 2005), (Berton, 2006) made it possible to replace mechanical actuators. This reduced the weight of the system but required greater power consumption in return. Another method considered the acting on the surface directly using piezoelectric materials (Moosavian, Chae, Pankonien, Lee, & Inman, 2017), (Wang, Bartley-Cho, Martin, & Hallam, 2001). However, these materials only allowed small displacements, and required large electrical consumption.

In our work, to obtain a deformation of the trailing edge rib, vertical incisions were made. Depending on the length, the number and the width of these incisions, it is possible to modify the flexibility of the rib and the amplitude of the deformation. To control the deformation of the rib, a servomotor is used that acts directly on the trailing edge as shown in Figure 3.1.

In order to analyze the aerodynamics of the deformed rib, it is firstly necessary to compute its structural deformation using a Finite Element Analysis modelling in CATIA V5 as illustrated in Figure 3.2.

From the results of the Finite Element Analysis, the contour of the deformed rib was extracted using the PROFSCAN tool (Aero@Net & Cnc@Net, 2004). PROFSCAN can draw a curve from an image to create a “.DAT” file that is used further in the XFLR5 software (Figure 3.3). To compare the aerodynamic efficiency of the two airfoils, a wing was defined with the same geometrical dimensions as the reference wing previously studied at the LARCASE (Communier, Flores Salinas, Carranza Moyao, & Botez, 2015): 10 in (254 mm) for the chord and 11.5 in (292.1 mm) for the span. This wing was analyzed for the inclined, rigid aileron, and then, for the Morphing Trailing Edge (MTE), both with a vertical displacement of trailing edge corresponding at 6.8% of the chord.

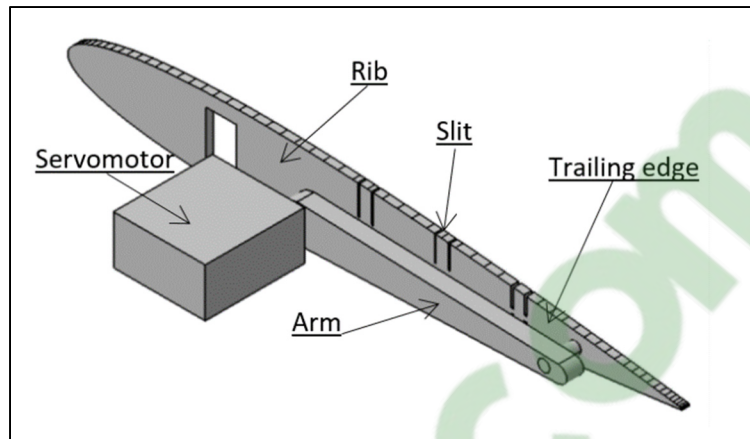


Figure 3.1 Control of the trailing edge rib deformation



Figure 3.2 Deformed rib in CATIA V5

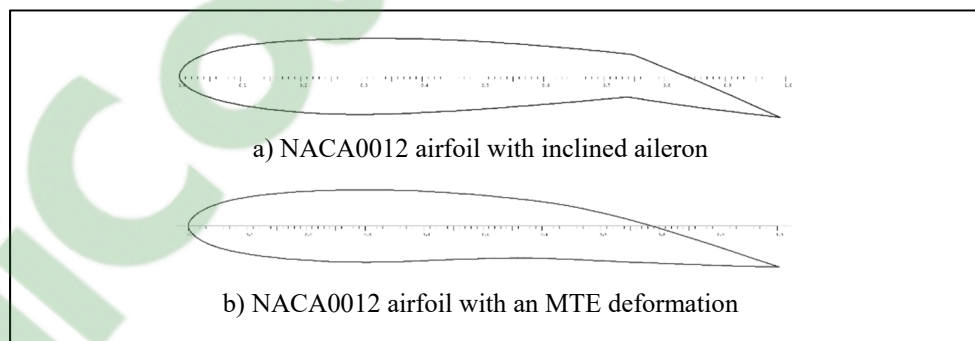


Figure 3.3 NACA0012 airfoil with inclined aileron a) and with MTE b)

The curves presented in Figure 3.4 compare the performance of a wing with an inclined aileron and that of a wing with a MTE for the airfoils presented in Figure 3.3(a), and in Figure 3.3(b). The calculations were carried out for a speed of 20 m/s (65.62 ft/s) using the 3D Panels method of the XFLR5 code (Onen, et al., 2015). The 3D Panels method calculates the aerodynamic flow around a wing quickly. This method alone does not allow to obtain the viscous flow characteristics (parameters), but by using the Xfoil analysis on the wing airfoils (2D), an extrapolation was made to calculate the viscous flow for the wing (3D). XFLR5

proposes another method of calculation, but we prefer this method because it allow us to recover the distribution of the coefficients of pressure on the upper and lower surfaces of the wing in order to carry out an aero structural analysis on CATIA V5 (Communier, Flores Salinas, Carranza Moyao, & Botez, 2015). The calculation method does not allow for the aerodynamic coefficients to be computed after the stall of the air flow, and for this reason, the calculations stop at the angle of 14° .

Regarding the drag coefficient reduction, the MTE generates less drag than the inclination of the aileron for the same displacement, which meets our goal. This decrease in drag comes mainly from the fact that the deformation of the camber takes place on a larger portion of the wing chord than the deformation of the camber induced by the aileron. The size of the aileron was chosen accordingly to its required geometry by the aircraft model ($\sim 25\%$ of the chord), and the length of deformation according to the chord of the MTE was chosen to be close to a NACA4412 airfoil chord, so that a variation of camber from 40% of the chord to the leading edge was obtained.

The wing with an inclined aileron generates more lift than the MTE for their same vertical displacement of the trailing edge of 6.8% of the chord. Wing with inclined aileron generates more lift but they incur more drag, while the MTE generates less drag but also less lift. Therefore, it is difficult to determine which system is the most efficient from the point of view of these two forces. However, the variation of the L/D ratio with the angle of attack is traced in Figure 3.4 to indicate which system would have the best ratio of lift to drag (L/D).

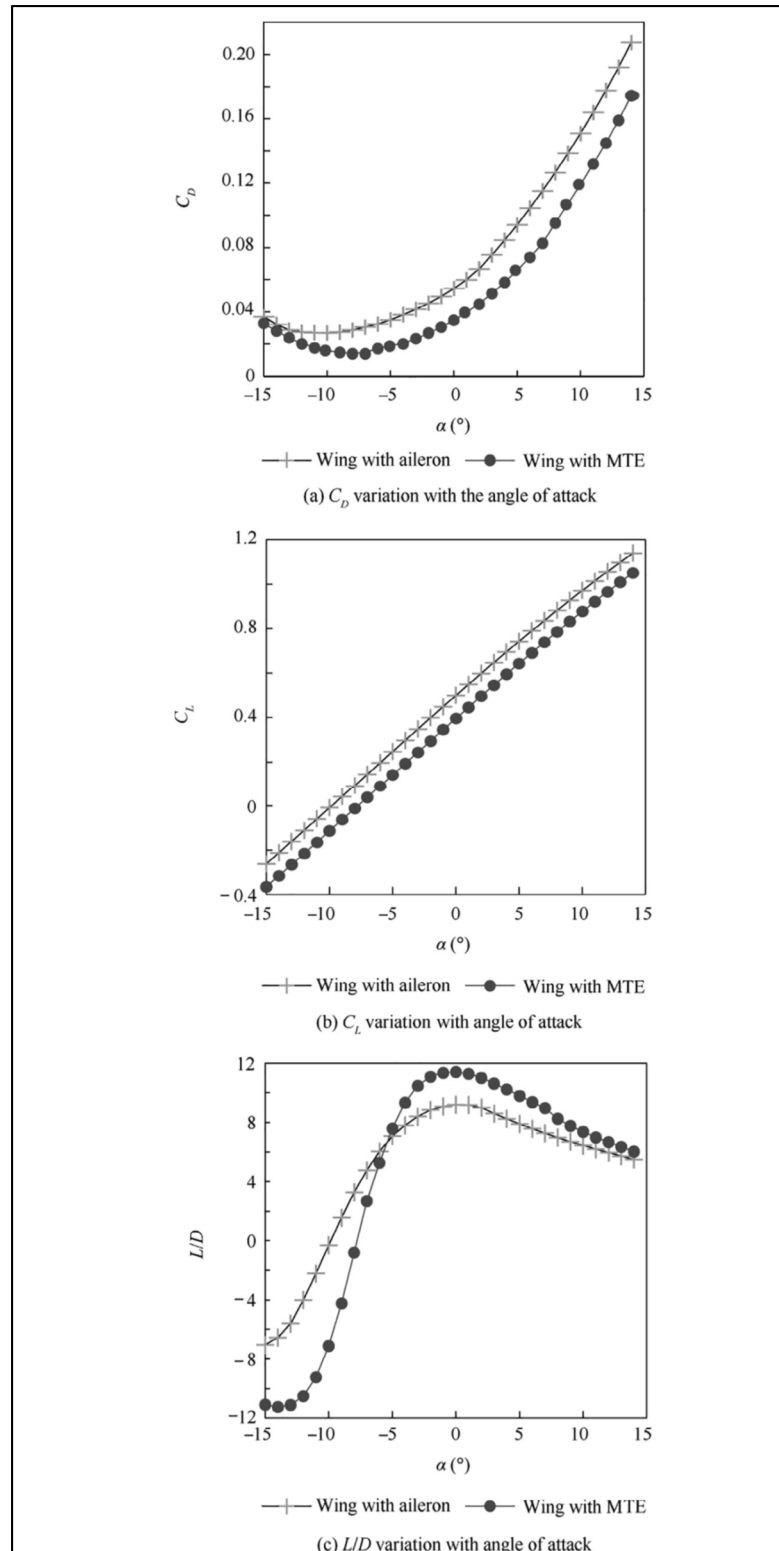


Figure 3.4 Comparison of the performance of a wing with inclined aileron and MTE

The L/D ratio variation with the angle of attack presented in Figure 3.4 shows that the MTE has a better L/D ratio than an inclined aileron for angles of attack higher than -5° ; thus, the MTE is more efficient than the inclined aileron for positive angles of attack. These first theoretical results encouraged us to continue in this direction in order to obtain experimental results.

In the next section, we will discuss on the ways in which the slits in the ribs were sized through design to obtain the MTE that was manufactured using wood.

3.3 Sizing design and control of the MTE

3.3.1 Sizing design

To achieve rib flexibility, the anisotropic property of wood was used. Using the fibers in the direction of the chord of the airfoil and making a slit section on the thickness of the airfoil, the bending points were created according to the characteristics of the “compliant mechanisms” (Howell L. L., 2001). These bending points behave like “pivot points” (Howell & Midha, 1994) by allowing the simplification of the calculation of the maximum displacement of the MTE. The advantage of this design using bending pivots with respect to a conventional design with mechanical pivots is that there is no need for a mechanism to allow the rotation of the MTE. This fact reduces the weight of the assembly, and facilitates wing maintenance. In order to reduce the force required to bend the rib, the slit (see Figure 3.1) must be designed as deep as possible, while keeping enough material for the rib structure to withstand tangential stresses. In order to find out the values of these stresses, the aerodynamic forces were firstly computed on the MTE.

For the first prototype, no sizing calculations were made, and the already acquired experience in wooden wing design and fabrication was sufficient for its manufacturing. In addition, to facilitate the prototype design, the symmetrical slits were dimensioned with symmetrical airfoils that allowed the MTE to change its shape by moving upwards and downwards. The

slit was considered as a pivot point, and its displacement for a given width in the rib was calculated. Figure 3.5 illustrates the parameters required for the rib deformation calculation.

From Figure 3.5, the following equations are obtained as the rib is symmetrical:

$$p = (e - t)/2, \quad (3.1)$$

$$l = p \times \tan a \quad (3.2)$$

$$y = L \times \tan a \quad (3.3)$$

The displacement y depends on the dimensions of the slit according to the next equation:

$$y = (l \times L)/p \quad (3.4)$$

To obtain this equation, the slits were considered as pivot and so the equations correspond to an angle return.

As we have n slits in the rib, we get the total displacement given by:

$$y_t = \sum_{i=1}^n y_i \quad (3.5)$$

$$y_t = \sum_{i=1}^n (l_i \times L_i)/p_i. \quad (3.6)$$

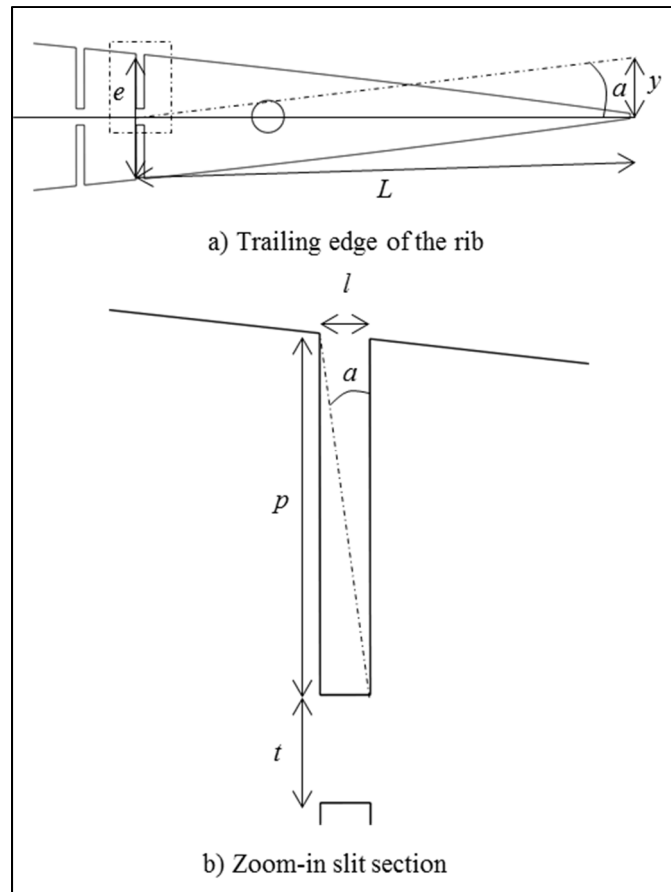


Figure 3.5 Deformation of the rib

3.3.2 MTE control

The deformation of the MTE is controlled by a servomotor via a rod connected to the trailing edge (see Figure 3.1). In order for the system to operate properly, the actuator must deliver sufficient torque. A FEA was performed to obtain the needed torque for the control of the wing under aerodynamical pressures. (20 m/s = 65.62 ft/s) with an angle of attack of 15° , as shown on Figure 3.6, the surface stresses caused by the aerodynamic pressure were low. The servomotor must mainly counter the elastic resistance of the ribs. The geometry of the ribs makes their resistance to be very low. However, the servomotor provides enough forces to counteract the aerodynamic forces on these ribs. For the prototype, the same servomotor as the one for a conventional aileron was used (Figure 3.7). Therefore, the morphing mechanism

was transferred on a conventional wing without changing its weight from the point of view of the controls.

In the next section, the manufacturing of the MTE system and, the results of the wind tunnel test are presented.

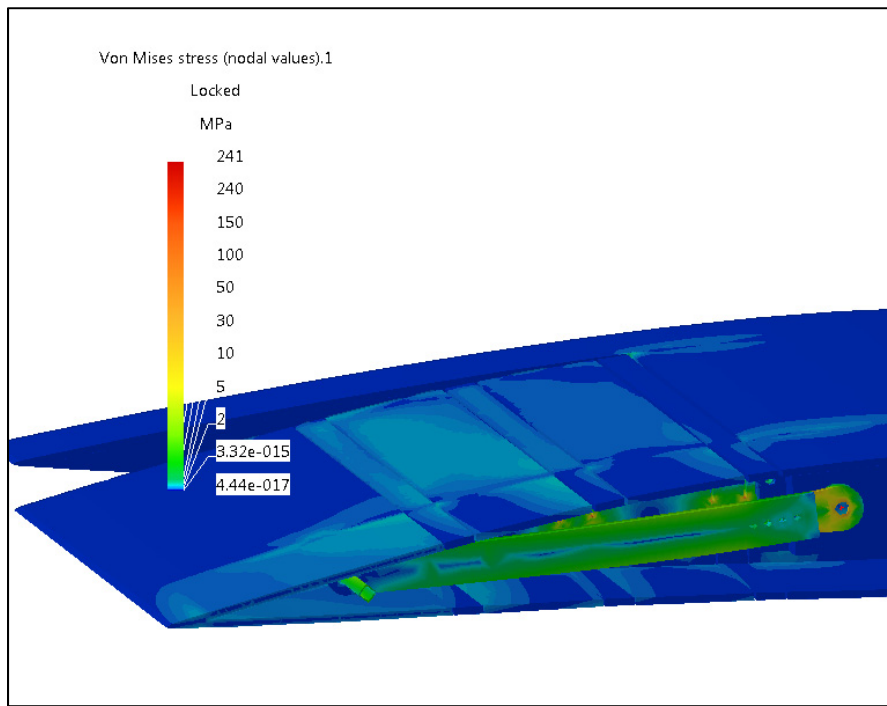


Figure 3.6 FEA of MTE control under aerodynamical pressures

ANNOUNCED SPECIFICATION OF HS-5645MG STANDARD SPORT DIGITAL HIGH TORQUE SERVO		
1. TECHNICAL VALUES		
CONTROL SYSTEM	:+PULSE WIDTH CONTROL 1500usec NEUTRAL	
OPERATING VOLTAGE RANGE	:4.8V TO 6.0V	
OPERATING TEMPERATURE RANGE	:-20 TO +60°C	
TEST VOLTAGE	:AT 4.8V	
OPERATING SPEED	:0.23sec/60° AT NO LOAD	:0.18sec/60° AT NO LOAD
STALL TORQUE	:10.3kg.cm(143.03oz.in)	:12.1kg.cm(168.03oz.in)
OPERATING ANGLE	:45° ONE SIDE PULSE TRAVELING 400usec	
DIRECTION	:CLOCK WISE/PULSE TRAVELING 1500 TO 1900usec	
IDLE CURRENT	:3mA	:3mA
RUNNING CURRENT	:350mA	:450mA
DEAD BAND WIDTH	:1usec	
CONNECTOR WIRE LENGTH	:300mm(11.81in)	
DIMENSIONS	:40.6x19.8x37.8mm(1.59x0.77x1.48in)	
WEIGHT	:60g(2.11oz)	

Figure 3.7 Servomotor specifications

3.4 Manufacturing and wind tunnel testing

3.4.1 Manufacturing of the MTE system

LASER cutting machine was used to manufacture both test wings, and allowed obtaining their components quickly and at a reasonable cost. To validate the functionality of this MTE, a prototype was manufactured to deform three ribs as shown in Figure 3.8. Figure 3.9 shows the system including the ribs deformation. The trailing edge is shown on the right hand side of Figure 3.8 and Figure 3.9. The structure of the wing is simple as is equipped with a main spar and three ribs. The thin spars have a main purpose of helping during the manufacturing process but are not required in the wing structure because balsa sheeting is added to cover the wing and the main spar is designed to support all the loads on the wing.

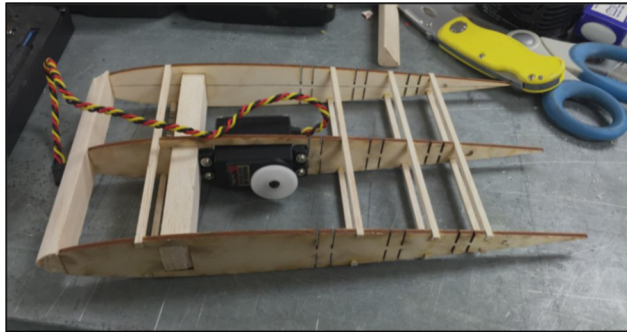


Figure 3.8 Structure of the MTE system



Figure 3.9 Prototype with a MTE system

3.4.2 Wind Tunnel Tests

The numerical results were validated by means of wind tunnel tests on the various morphing wings. The morphing wings have the same dimensions as the reference wing (Figure 3.10(a)), so that the impact of the system on the morphing wing was compared to the same wing without any deformation system (the reference wing). The reference wing has the NACA0012 airfoil with a chord of 10 in (254 mm) and a wingspan of 11.5 in (292.1 mm). The 10 in (254 mm) chord relates to the chord of the test wing of the ATR42 research project at the LARCASE which also was of 10 in (254 mm). The wing span is 12 in (304.8 mm), which corresponds to the mid-height of the wind tunnel test chamber, but 0.5 in (12.7 mm) is embedded in the base of the wing that is attached to the aerodynamic scale, which is the reason why the analysis is carried out on a wing with a span of 11.5 in (292.1 mm). The aerodynamic scales is used to measure the loads (forces and moments) on the aerodynamic model installed in the wind tunnel.

An objective of the design of the reference wing was to validate firstly the functioning of the LARCASE aerodynamic scales by comparing the measured values with the numerical values of the loads (forces and moments) acting on the wing. Figure 3.10(b) shows the dimensions of the reference wing.

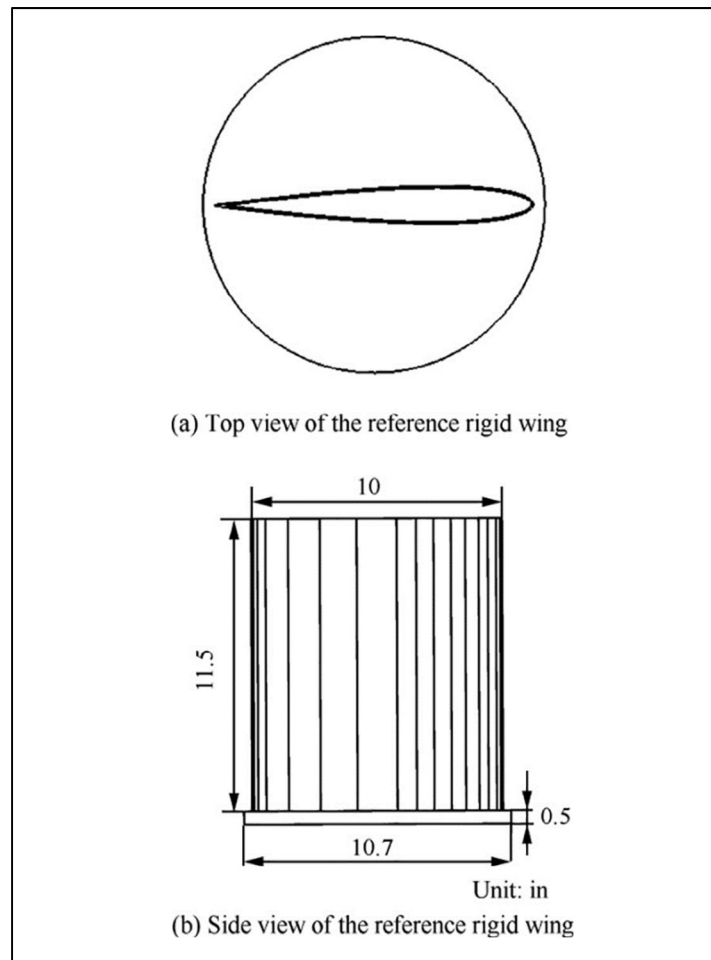


Figure 3.10 Reference rigid wing dimensions

Wind tunnel tests were performed on this reference wing as part of the Master's thesis of the main author (Communier, 2015), in which the experimental aerodynamic performances with respect to their numerical values computed by XFLR5 software (Communier, Flores Salinas, Carranza Moyao, & Botez, 2015) were compared, and further validated. The tests were carried out in the Price-Paidoussis wind tunnel's rectangular test chamber (2 ft [609.6 mm] x 3 ft [914.4 mm], Figure 3.11) at speeds of 20 m/s (65.62 ft/s), 25 m/s (82.02 ft/s), 30 m/s (98.43 ft/s) and 35 m/s (114.83 ft/s). The Price-Paidoussis wind tunnel can reach a maximum speed of 37 m/s (121.39 ft/s) for this test chamber.



Figure 3.11 LARCASE Price-Paidoussis subsonic wind tunnel

The angle of attack of the wing was changed from -10° to 20° by 1° steps. The measurements were carried out with an aerodynamic scales equipped with an Omega 160 force sensor from ATI Industrial Automation. Its technical details expressed in term of maximum loads (forces and moments) are presented in Table 3.1. This scale was designed by the LARCASE team. Following the manufacturer's specifications, it was possible to improve the resolution of the sensor, as well as its accuracy by filtering the measurement given by the aerodynamic scales. This filtering allowed us to obtain resolution of 0.01 N with a maximum error of 0.1 N due to the rotation mechanism of the aerodynamic scales. The applied digital filtering enable higher accuracy sampling of the drag force. The theoretical values of the lift, the drag and the pitch coefficients were calculated with the “3D Panels” method by using XFLR5 code for a wing with the span of 11.5 in (292.1 mm) and the chord of 10 in (254 mm). The wing in the wind tunnel was in contact with the floor of the test chamber, and this contact was simulated using the symmetry of the span in the XFLR5 code. The calculated wing therefore had a total span of 23 in (584.2 mm). Figure 3.12 to Figure 3.14 show the variation of the drag, lift and pitch coefficients of the wing with the angles of attack. The measured values in the wind tunnel are compared to the calculated values using XFLR5 code.

At a speed of 20 m/s (65.62 ft/s), the wing has a stall angle of 18° , and at a speed of 25 m/s (82.02 ft/s), the stall occurs at 19° . For a speed of 30 m/s (98.43 ft/s) and 35 m/s (114.83 ft/s),

there was no stall occurrence before 20°. The stall angles at 20 m/s (65.62 ft/s) and 25 m/s (82.02 ft/s) were not obtained during the calculations because of the fact that the calculation method does not allow the coefficients to be computed (Communier, Flores Salinas, Carranza Moyao, & Botez, 2015).

Table 3.1 Range and resolution for ATI Omega 160 F/T sensor

Technical index	F _x ,F _y	F _z	T _x ,T _y	T _z
Sensing ranges	2500 N (600 lbf)	6250 N (1500 lbf)	400 Nm (3600 lbf-in)	400 Nm (3600 lbf-in)
Resolution	1/2 N (1/8 lbf)	3/4 N (1/4 lbf-in)	1/20 Nm (1/2 lbf-in)	1/20 Nm (1/4 lbf-in)

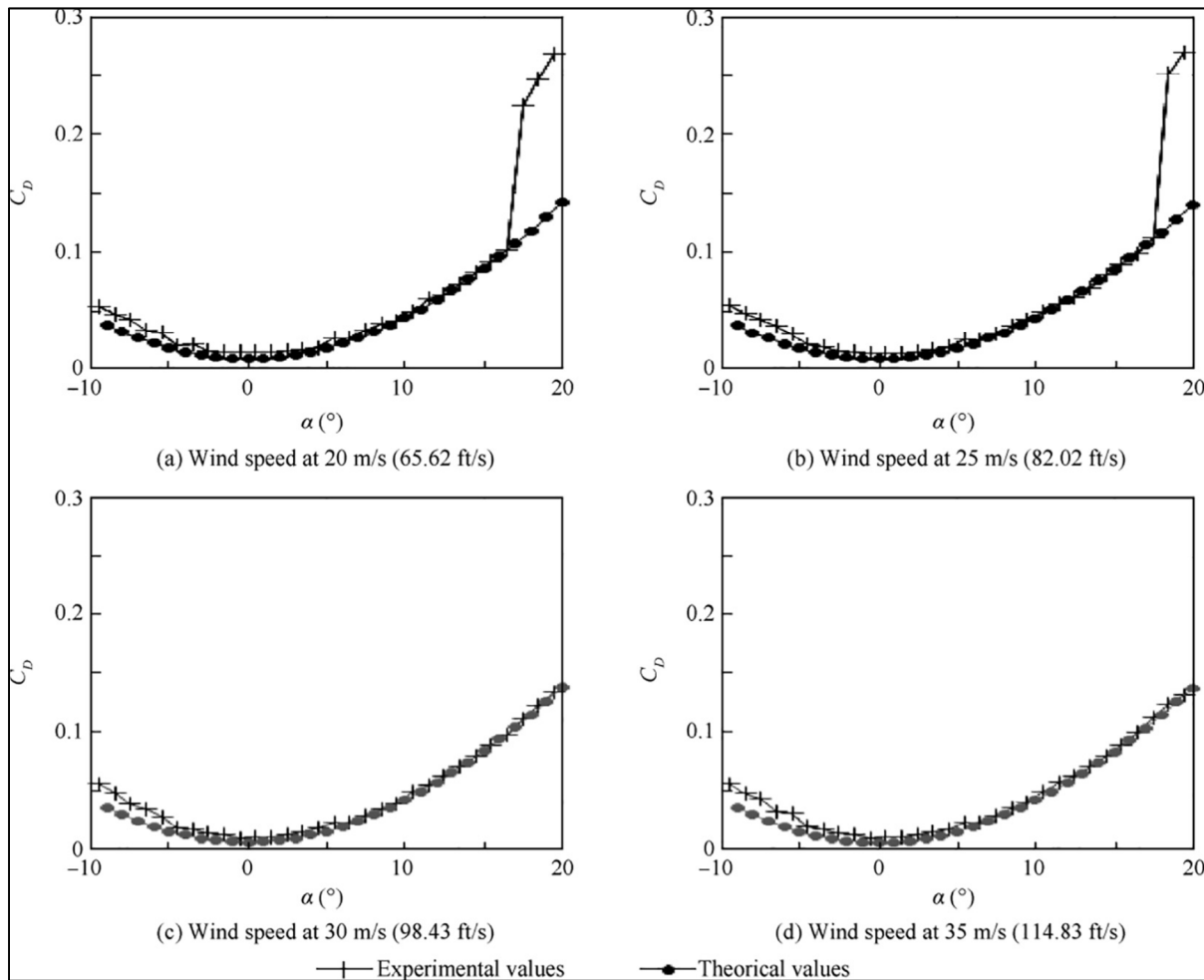


Figure 3.12 Drag coefficients variation with angle of attack for the reference wing

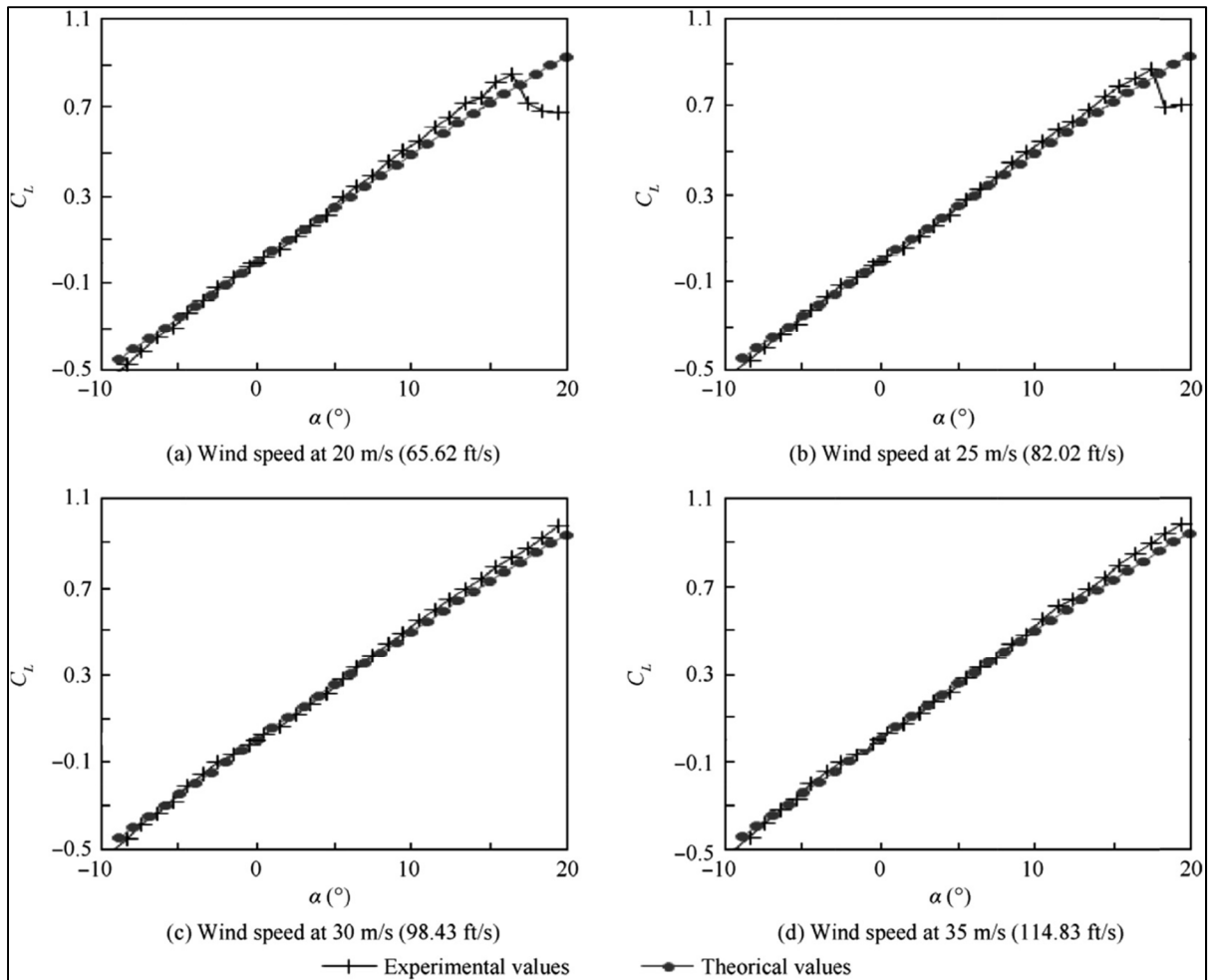


Figure 3.13 Lift coefficients variation with angle of attack for the reference wing

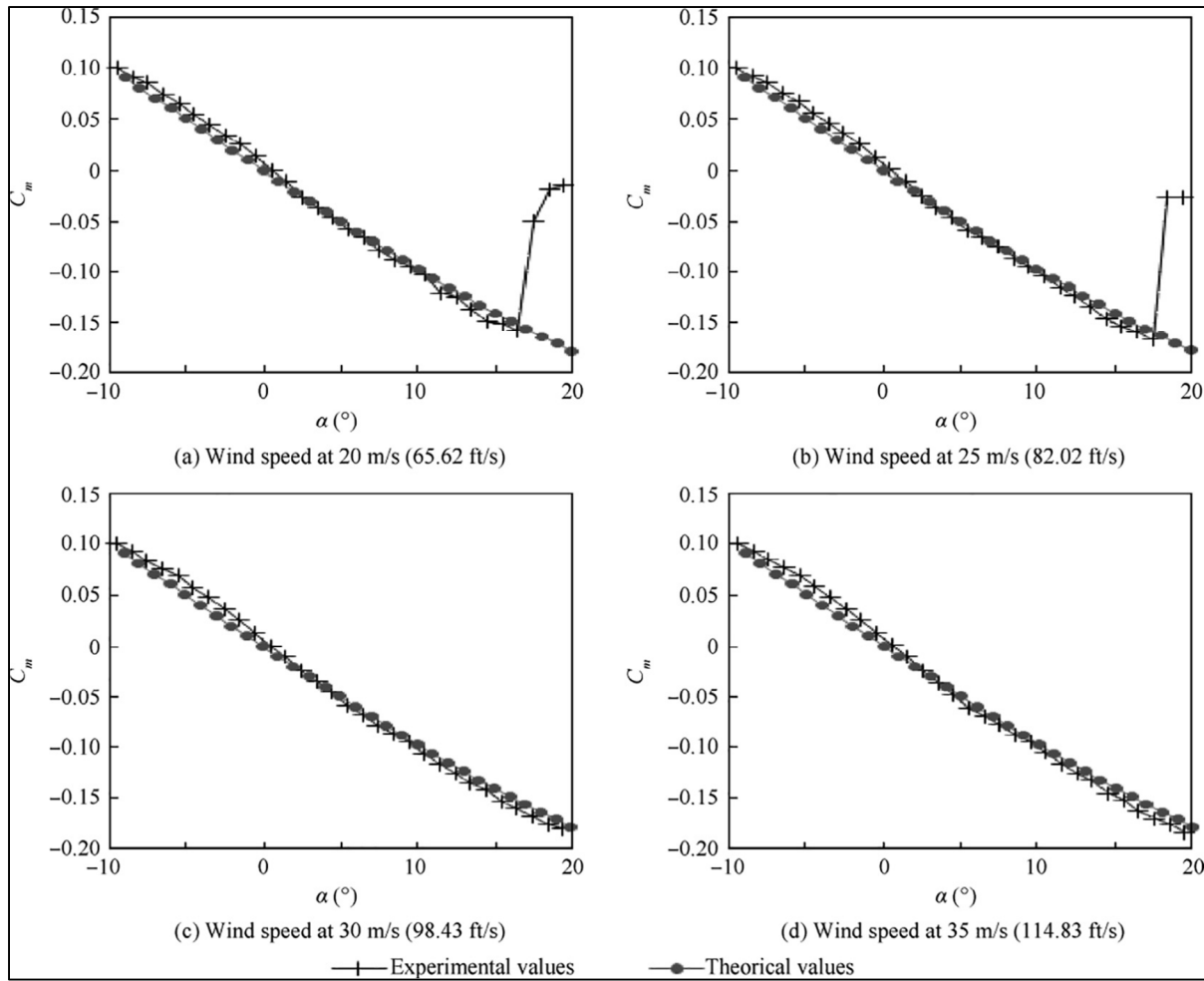


Figure 3.14 Pitch coefficients variation with angle of attack for the reference wing

The objective of the static test is to validate that the mechanism of the MTE is morphed when a command is sent to the system. There is the need to validate that this experimental deformation of the MTE corresponds to the calculated deformation. For the static tests, a command was sent to the servomotor controlling the MTE, and the vertical displacement at the tip of the trailing edge was measured.

Figure 3.15 shows the dimensioned slits necessary to calculate the total deformation of a rib of the wing. An optimization method was not used to determine the number of slots and their dimensions. Instead, an iterative method using FEA module of CATIA V5 was used, by manually changing the sizes of the slits according to the stresses on the ribs obtained using

FEA. The main objective of static tests was to obtain the deformation of the inclined aileron presented in Figure 3.15 with the constraints, expressed in term of the torque available by the actuator and the mechanical strength of the wood used for the prototype (plywood (Cai & Ross, 2010)).

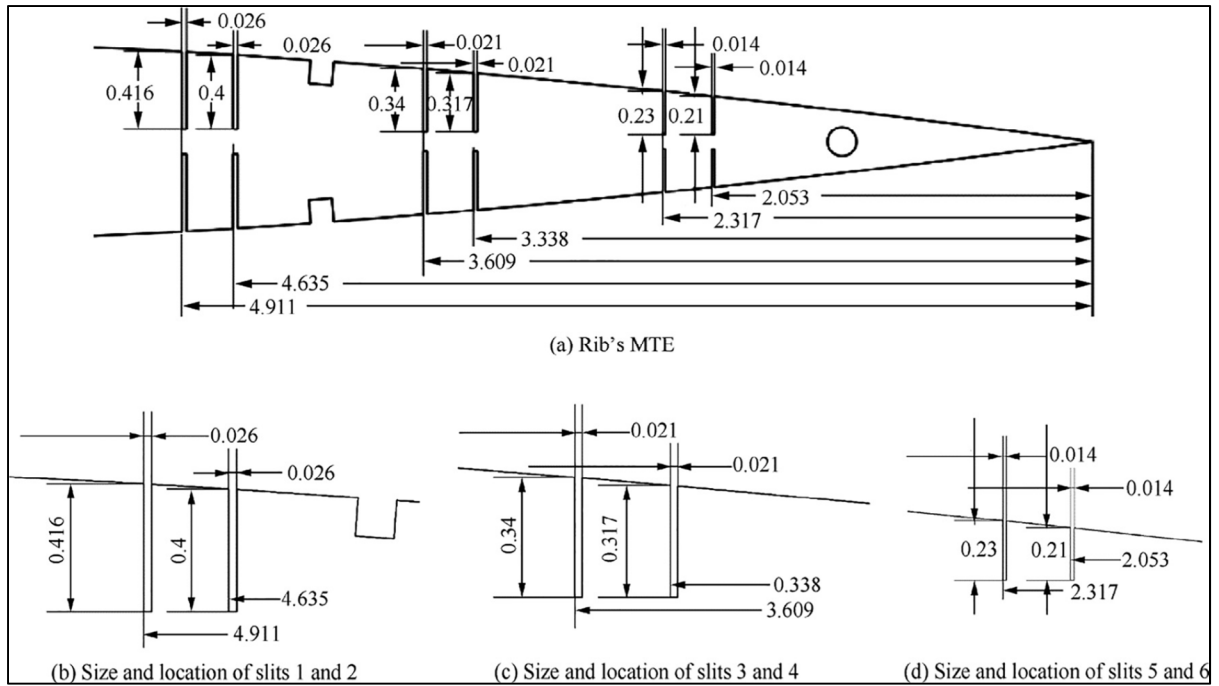


Figure 3.15 Size and location of the slits in the MTE rib (unit: in)

The Table 3.2 lists the dimensions of the slits from left to right in inches

Table 3.2 Size of the slits in the deformable rib

Slit number	l_n	L_n	p_n
1	0.026	4.911	0.416
2	0.026	4.635	0.4
3	0.021	3.609	0.34
4	0.021	3.338	0.317
5	0.014	2.317	0.233
6	0.014	2.053	0.205

According to equation (3.6) and values of l_n , L_n and p_n given in Table 3.2Table , the maximum displacement y_t is calculated as

$$y_t = \frac{0.026 \times 4.911}{0.416} + \frac{0.026 \times 4.635}{0.4} + \frac{0.021 \times 3.609}{0.34} + \frac{0.021 \times 3.338}{0.317} + \frac{0.014 \times 2.317}{0.233} + \frac{0.014 \times 2.053}{0.205} = 1.33 \text{ in} \quad (3.7)$$

Figure 3.16 illustrates the measurement of the displacement of the trailing edge during a 7° rotation of the actuator.

The distance between the axis of the servomotor that controls the deformation and the axis that moves the trailing edge is 4.25 in (107.95 mm) and the distance between the axis of the servomotor and the trailing edge is 5.6 in (142.24 mm) (Figure 3.17). Thus, for a displacement of the servomotor axis of 7° , the displacement of the trailing edge axis is 0.52 in (13.21 mm) according to the equation (3.3). For a linear displacement of the trailing edge, this displacement would be 0.69 in (17.526 mm). Since the deformation is given by six articulations (joints) that are not aligned on the actuator axis, the MTE does not move along the same axis as the actuator arm. These calculations do not give a precise value for the displacement; a FEA method makes it possible to obtain a very good precision on the deformation value.

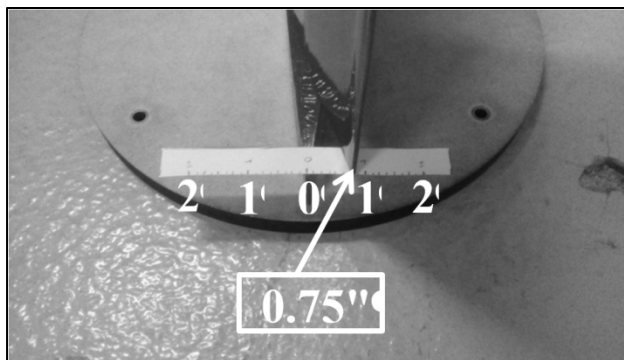


Figure 3.16 0.75 in displacement of the trailing edge tip (19.05 mm) for a 7° rotation

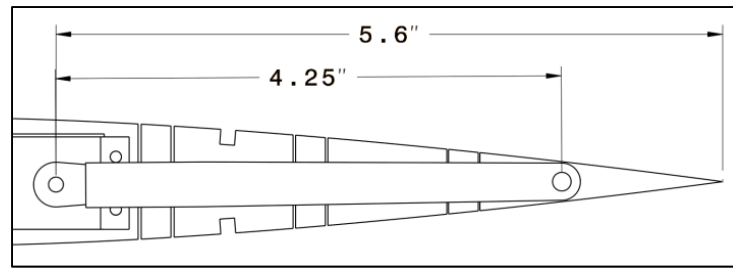


Figure 3.17 Controlling distance

Wind Tunnel Tests measurements were performed to validate the dynamic operation of the system. The main objective of these measurements was to validate that the deformation was well carried out in the presence of aerodynamic loads. These tests allowed us to observe the influence of the mechanism on the drag of the wing compared to the drag of the reference wing (without any mechanism). In this section, the MTE is not moved (displaced) by the controller. Wind tunnel measurements with controlled displacement of the MTE will be presented in the next section. Figure 3.18 presents the test wing used to obtain the following results, shown in Figure 3.19.

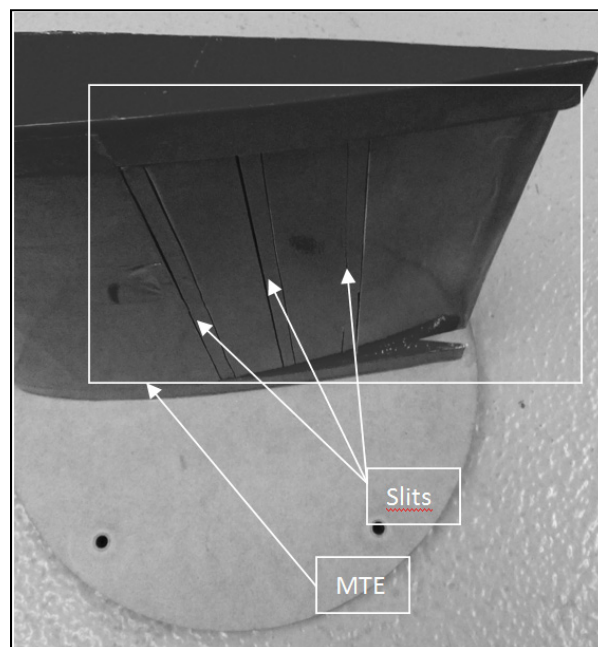


Figure 3.18 Test wing with MTE

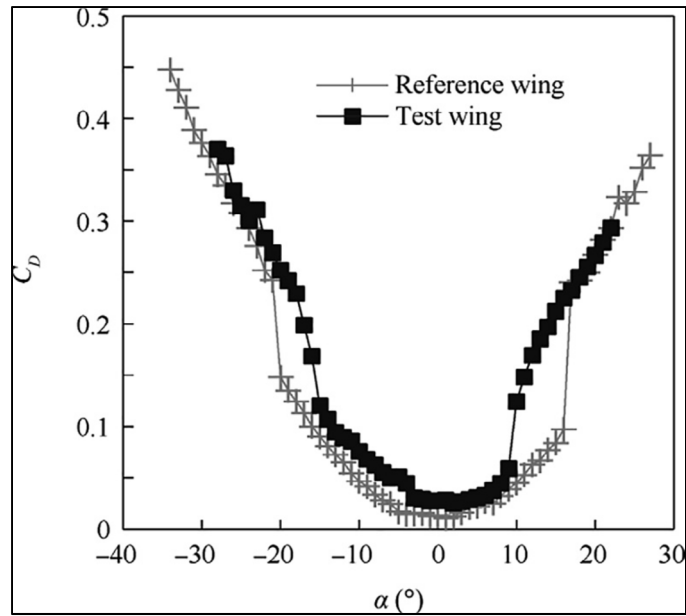


Figure 3.19 Influence of the MTE on the drag coefficient at 15 m/s (49.21 ft/s)

Two causes were identified for the increase in drag on the morphing wing with respect to the drag for the reference wing:

1. The discontinuity between the fixed section of the wing and the moving section of the wing;
2. The presence of the slits on the surface of the wing allowing deformations.

The first cause is common to both the aileron and the MTE system. The second cause is due only to the specific design of the MTE system. For this reason, it was chosen to work on the second cause in order to improve the design of the MTE system.

Four experiments were therefore defined to improve the airflow around the wing. The first experiment reproduced a rigid wing by covering all the slits on the wing with tapes (Figure 3.20). For the second experiment, the tape covering the intersection between the morphing part and the fixed part of the wing was removed (Figure 3.21). For the third experiment, the tapes were installed on one side of the slits (leading edge side) with the aim to hide them but

without hampering the deformation (Figure 3.22). For the fourth and last experiment (Figure 3.23), tapes were installed on both sides of the slits that allowed some deformation of the trailing edge (a bump or a hollow were formed on the tape during the deformation).



Figure 3.20 Experiment 1 with all slits covered by tapes (continuous surface)

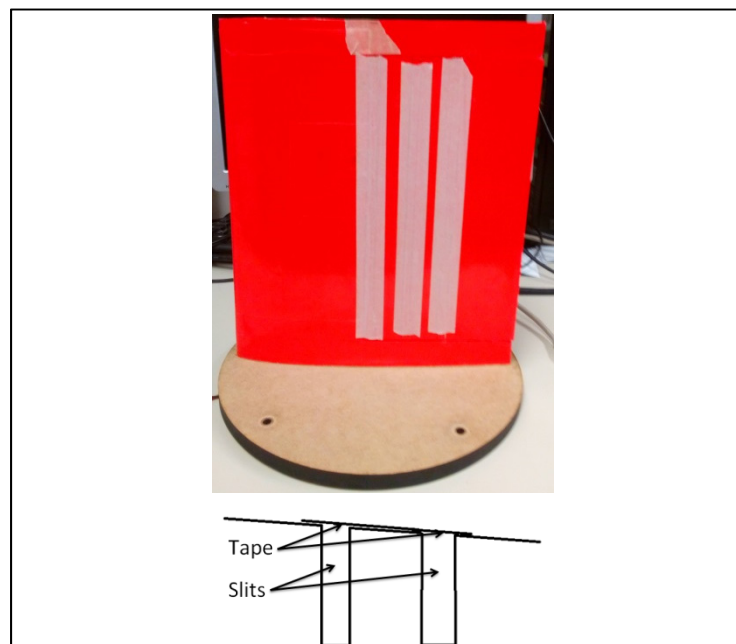


Figure 3.21 Experiment 2 tapes covering the intersection between the morphing fixed parts were removed

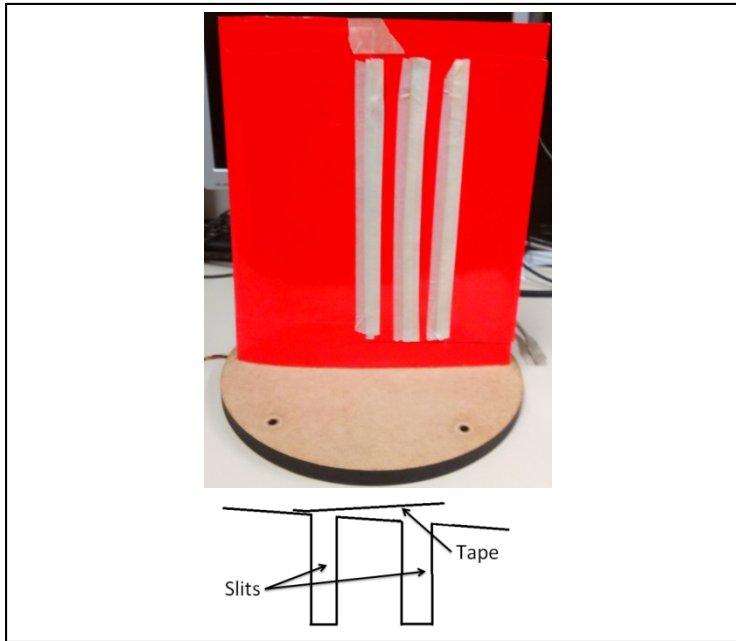


Figure 3.22 Experiment 3 with tapes installed on one side of the slits (deflector)

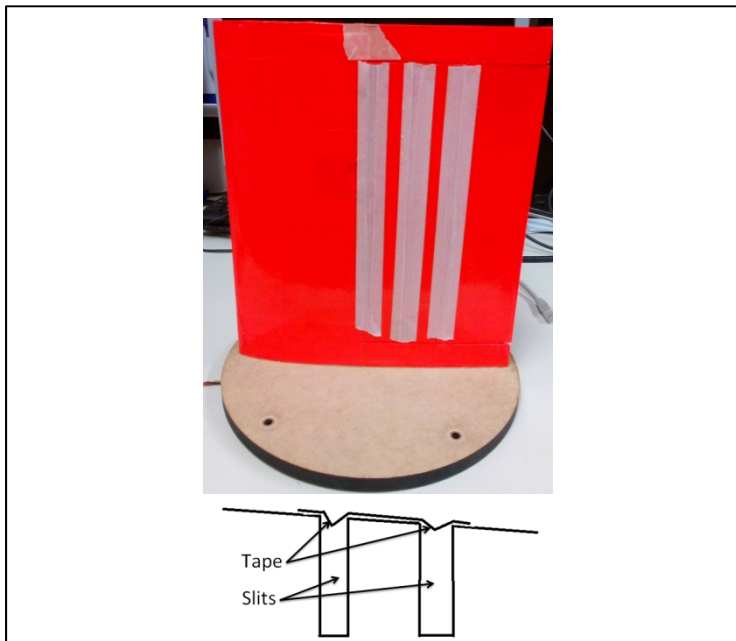


Figure 3.23 Experiment 4 with tapes installed on both sides of the slits

The first experiment was conducted to confirm that the drag difference was not due to an imperfection on the wing. The second experiment was performed to identify the influences of the discontinuities between the fixed part and the morphing part of the wing. Experiments 3 and 4 were conducted on improved design of the morphing test wing and had the aim of improving its aerodynamic performances. The drag coefficient measurements obtained with experiments 1-4 were traced versus the drag coefficients obtained numerically for the morphing and reference test wings (Figure 3.24).

During Experiment 1, difference was recorded in the stall angles (from 9° to 16° for positive angles and from -16° to -20° for negative angles). Further studies are necessary to identify the cause of this difference. A drag coefficient curve variation similar to that of the reference drag coefficients was observed (Figure 3.25).

Experiment 2 indicates that the discontinuity would have a higher influence for an angle of attack close to 0° than the influence for higher angles of attack ($\pm 5^\circ$). The comparison between results obtained for experiments 3 and 4 is not obvious. Thus experiment 3 was found to be more efficient than experiment 4 for positive angles but less efficient for negative angles (Experiment 3 shows an asymmetry in the results). However, an analysis of the L/D ratio variation with the angle of attack makes it possible to determine that one experiment is more effective than another (Figure 3.26). In Figure 3.26, the L/D variation with the angle of attack between 4° and 8° for the reference wing is due to the maximum error of 0.1 N on the measurement of the drag force.

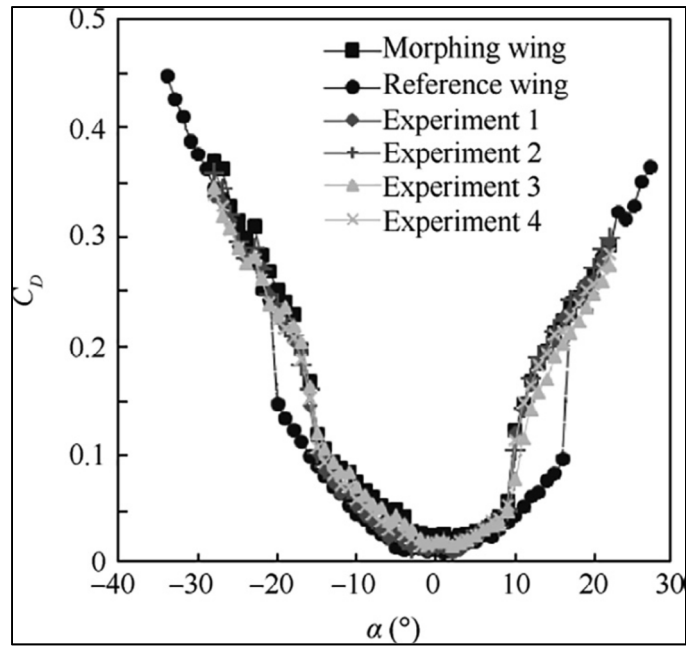


Figure 3.24 C_d variation with the angles of attack at the speed of 15 m/s (49.21 ft/s)

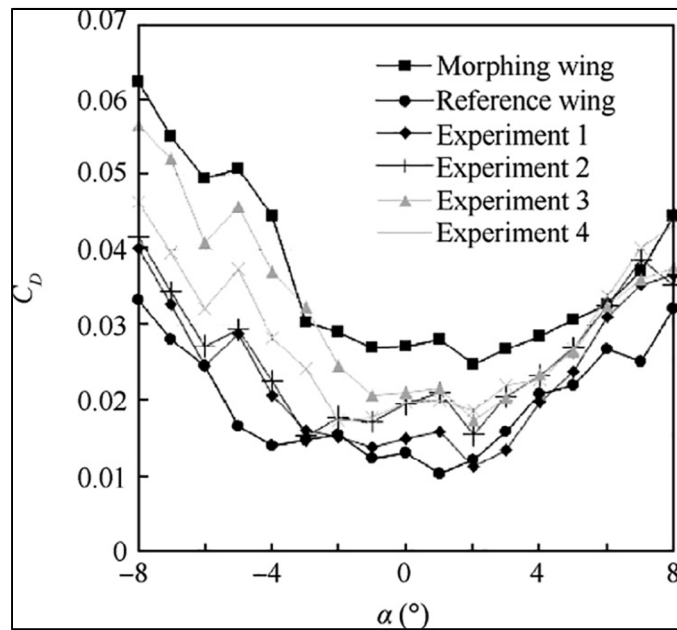


Figure 3.25 Zoom-in of the drag coefficients variation with the angles of attack between -8° and 8°

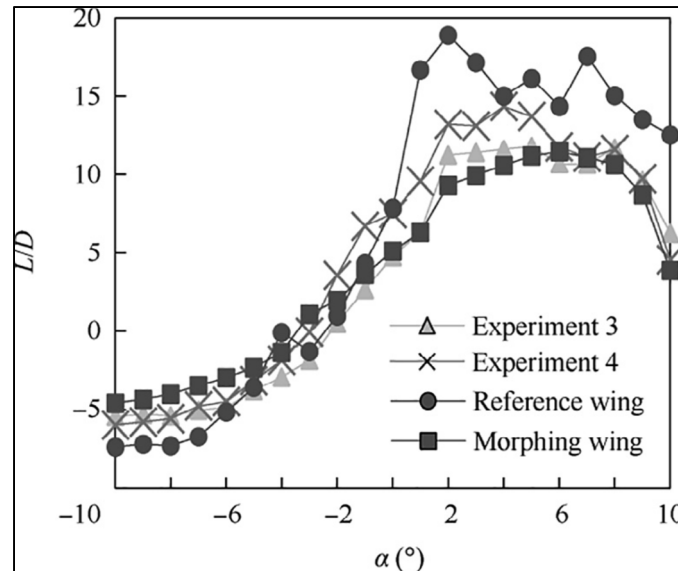


Figure 3.26 Wing L/D ratio variation with the angle of attack

3.5 Comparison of aerodynamics coefficients for a MTE versus a conventional aileron

Studies (Monner, D., & Elmar J., 2000) revealed that elastic trailing edge could be used for adaptive wing. To validate in this paper that the MTE is capable of replacing an aileron, wind tunnel tests were performed on both, the MTE and also on an aileron.

To perform these wind tunnel tests, a wing was designed and manufactured with its basic dimensions given in Figure 3.27, on which we placed an aileron. The width of the aileron is 25% of the wing chord and its span is 9.5 in (241.3 mm). There is 1 in (25.4 mm) on each side of the aileron as shown in Figure 3.27.

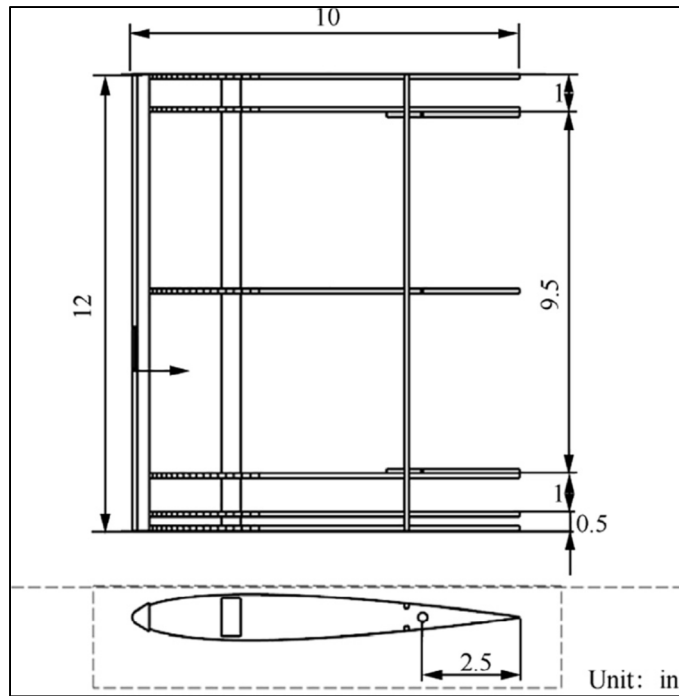


Figure 3.27 2D plan of the wing with an aileron

To be able to retrieve data efficiently, a control interface was added for the aileron to the Labview interface of the aerodynamic balance. Labview software makes it possible to program commands for actuator controls, and to read instrument outputs through a graphical interface that displays results. This interface controls a servomotor by indicating an angle for its control arm. The force was calculated and displayed for each angle of the actuator. To obtain an angle of the servomotor, the forces reading were averaged, and were further saved in a table. As long as this position was kept constant by the servomotor, its average value in the array was updated; when the angle changed, it was the average value of this new angle that was updated. By reviewing all the possible angles, the graph of the forces was drawn as a function of the angle of the servomotor, and the results were directly visualized. A backup function was added to write the values table of to a text file as a means to save the data. Then these values were studied in order to analyze the wings' aerodynamic performance.

3.5.1 Comparison of aerodynamics coefficients

In order to determine if the MTE system can replace an aileron on a wing, the corresponding lift and drag coefficients of the two systems were compared. Since the angles of the two systems are different, their behaviors are also different; their respective motions cannot be directly compared because of the difference in size between moving surfaces (Figure 3.15) and the control arms (Figure 3.16 and Figure 3.17). However, a similar evolution of the lift coefficient was observed for the two systems. As the goal of this paper is to determine if one system creates more drag than another system, the drag of both systems was compared for the same generated lift. The following graphs (Figure 3.28 and Figure 3.29) show the variation of the lift and drag coefficients C_L and C_D with the angle of attack for the aileron and the MTE compared to the C_L and C_D of the reference wing. From these figures, it was observed that the aileron can create a C_L greater than the C_L of the MTE, but the C_D of the aileron was also larger than the C_D of the MTE. Analysis of the behavior of the C_L allowed to define the roll that it could induce, and thus, to determine if the MTE can indeed replace ailerons (Vorobiev, Rennie, Jumper, & McLaughlin, 2008). This observation alone made it possible to define if one system was more efficient than another.

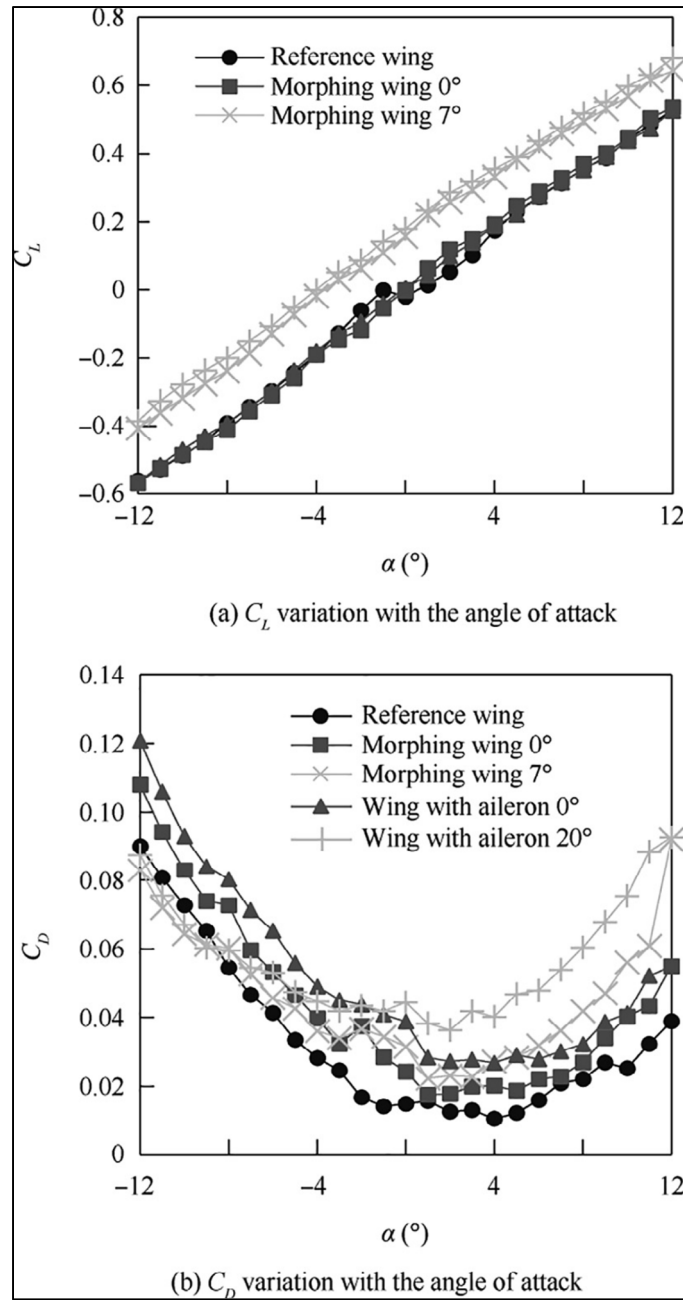


Figure 3.28 C_L and C_D variation with the angle of attack. At 15 m/s (49.21 ft/s) for each system

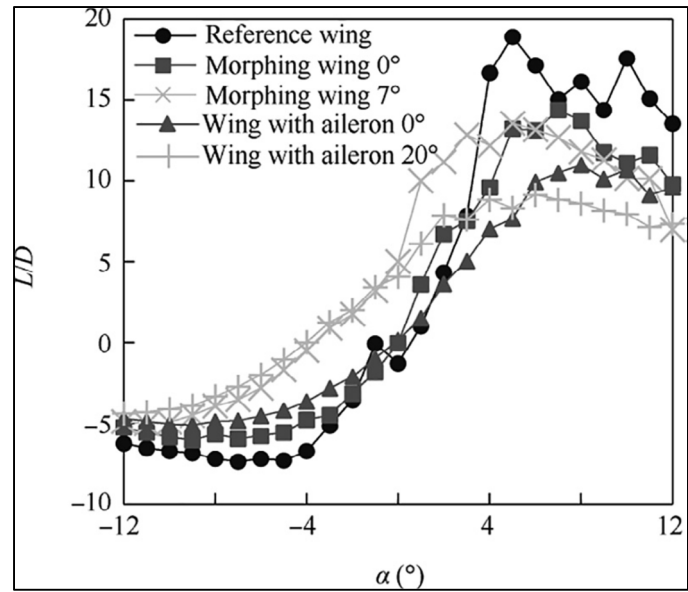


Figure 3.29 L/D ratio variation with the angle of attack at 15 m/s (49.21 ft/s) for each system

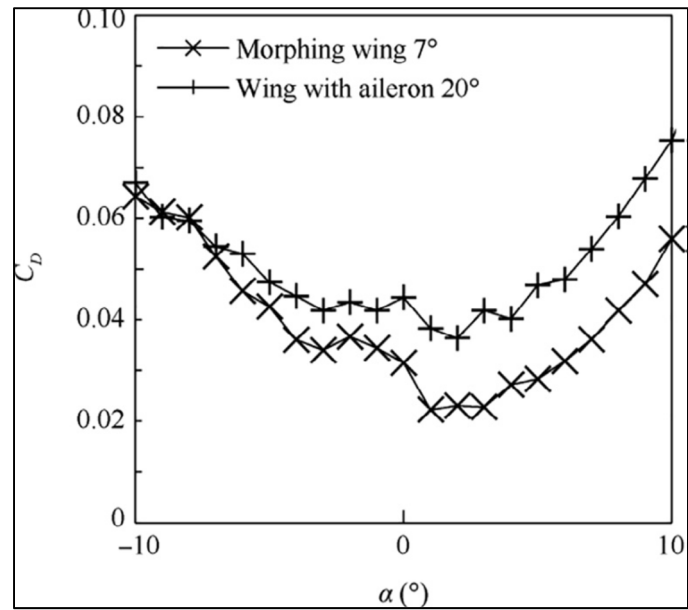


Figure 3.30 C_d variation with angle of attack zoomed-in around 0°

It was observed that the wing with the MTE created less drag (Figure 3.30), and therefore it had a higher L/D ratio (Figure 3.31) than the wing with an aileron. It can be therefore concluded that the MTE was more efficient than the aileron for angles of attack between -10° and 10° . Therefore, by replacing the conventional aileron with the MTE should result in a reduction in fuel consumption and further in an increase in aircraft autonomy and efficiency. This observation might also be valid for other aircraft control surfaces such as elevator and rudder.

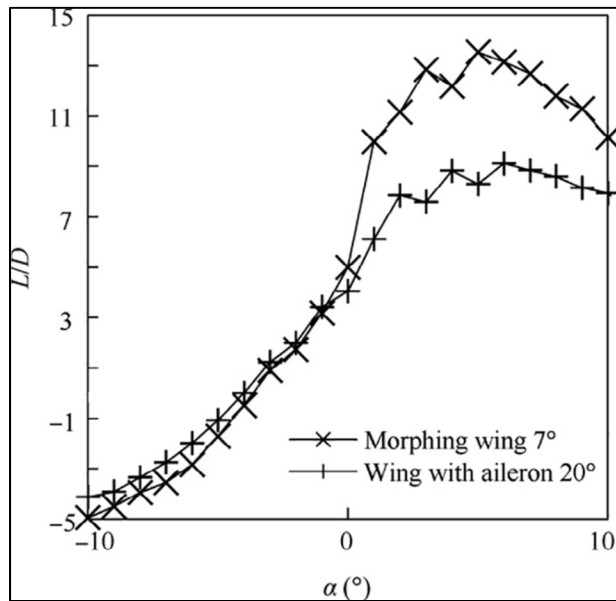


Figure 3.31 L/D ratio variation with angle of attack- zoomed-in around 0°

3.5.2 Electrical consumption

As the MTE requires deformation of the ribs actuated by the servomotor, the MTE requires more electrical energy to operate than an aileron. For a conventional aileron, without external aerodynamic forces, the servomotor does not need to act to keep the aileron in a fixed position (the wing is placed vertically) but for the MTE, the electrical resistance of the ribs induces an increase of the current required by the servomotor when its deformation is increased. In order to ascertain the magnitude of this difference, the current consumed by the

servomotors of the test wings was measured. For the wing equipped with an aileron, the current consumption remains constant at 3.5 mA from -40° to 40° . For the wing with the MTE, the current consumption varies from 3.5 mA at 0° to 70 mA at $\pm 7^\circ$ (with a jump from 16 mA at 6° to 70 mA at 7°). The current jump is due to the mechanical limit of the MTE. It is therefore important to accurately measure the travel limits of the MTE to avoid overconsumption of the system that could lead to a breakage of the servomotor. On the other hand, for the two test wings, an increase of the current consumption has not been noticed when an external aerodynamic force was applied. The dimensions of our test wings and the speeds used were too small for the forces, on the control surfaces, to disturb significantly the servomotors.

3.6 Conclusion

This paper describes the first phase of a new morphing wing project at the LARCASE. The MTE was firstly studied in this paper because this section of the wing was easier to deform (morph) than its other sections. The next step will be to adapt existing MTE design to modify also the leading edge of the wing. That leading edge section is more complicated than the trailing edge section to deform because of its smaller width (20% width for the leading edge and 50% width for the trailing edge), and thus, it is not evident that the morphing leading edge design will achieve a reduction in the wing drag.

However, the results obtained in this paper have shown an improvement in the effectiveness of the MTE on the wing drag, in particular in the sections where the ailerons are located. This comparative study between the MTE and the rigid aileron has verified that the MTE had the same behavior as an aileron regarding the increase of lift with the angle of attack. The drag analysis showed us that the MTE generated less drag than the aileron. Finally, analysis of the L/D ratio has shown that the MTE gave a lower drag for the same lift as an aileron, which led to less fuel consumption. Moreover, the MTE has the same components (rib and actuator) as an aileron, and thus does not increase the weight of the wing (both test wings weight is a total of 725 g (1.6 lb)). The use of the MTE led to the satisfaction of the following three criteria: to replace ailerons, to reduce fuel consumption and to maintain the mass of the wing.

Acknowledgments

The authors would like to thank Mr Aurélien Mons for his help in the preliminary design of the MTE, Mr Antoine Machetto for his help in the design of the rotation system of the aerodynamic balance and Mr Théo André for his help in carrying out tests in the wind tunnel for the wing with an aileron. In addition, the authors would like to thank very much to the NSERC for the Canada Research Chair in Aircraft Modeling and Simulation New Technologies funding.

CHAPTER 4

DESIGN, MANUFACTURING AND TESTING OF A NEW CONCEPT FOR A MORPHING LEADING EDGE USING A SUBSONIC BLOW DOWN WIND TUNNEL

D. Communier^a, F. Le Besnerais^b, R. M. Botez^c, and T. Wong^d

^{a, b, c, d} Department of Systems Engineering, École de Technologie Supérieure,
1100 Notre-Dame West, Montreal, Quebec, Canada H3C 1K3

Paper published in *biomimetics*, Vol. 4, No. 4, pp. 76, December 2019,
DOI:10.3390/biomimetics4040076

Résumé

Cet article présente la conception et les résultats des essais en soufflerie d'une aile comprenant un bord d'attaque déformable pour un véhicule aérien moyen sans pilote d'une envergure maximale de 5 m. La conception du système de bord d'attaque déformable fait partie des recherches sur la conception d'un système de cambrure déformable. La conception présentée ici a l'avantage d'être simple à fabriquer (construction en bois) et légère pour la structure de l'aile (*compliance mechanism*). Le prototype de bord d'attaque déformable montre la possibilité d'augmenter l'angle de décrochage de l'aile dans le but de retarder le décrochage. De plus, la modification de l'angle de décrochage est effectuée sans affecter la pente du coefficient de portance. Ce prototype est conçu pour valider la fonctionnalité de la méthode de déformation appliquée au bord d'attaque de l'aile. Pour la suite, le mécanisme peut être encore optimisé en termes de forme et de matériau pour obtenir une grande déformation du bord d'attaque et, ainsi, obtenir un impact plus important sur l'augmentation de l'angle de décrochage que le premier prototype de bord d'attaque déformable présenté dans cet article.

Abstract

This paper presents the design and wind tunnel test results of a wing including a morphing leading edge for a medium unmanned aerial vehicle with a maximum wingspan of 5 m. The design of the morphing leading edge system is part of research on the design of a morphing camber system. The concept presented here has the advantage of being simple to manufacture (wooden construction) and light for the structure of the wing (compliance mechanism). The morphing leading edge prototype demonstrates the possibility of modifying the stall angle of the wing. In addition, the modification of the stall angle is performed without affecting the slope of the lift coefficient. This prototype is designed to validate the functionality of the deformation method applied to the leading edge of the wing. The mechanism can be further optimized in terms of shape and material to obtain a greater deformation of the leading edge, and, thus, to have a higher impact on the increase of the stall angle than the first prototype of the morphing leading edge presented in this paper.

4.1 Introduction

This paper presents the morphing of the leading edge (LE) of a wing with the main goal of developing a morphing camber system and integrating it within the wing of a UAS-S4 Hécatl. The development of a morphing trailing edge (MTE) system has been presented in (Communier, Botez, & Wong, 2019). The effectiveness of this MTE system has been demonstrated experimentally in the Price–Païdoussis wind tunnel by comparing it to the effectiveness of a rigid aileron (Andre, et al., 2017). It was concluded that the MTE could replace an aileron, as it was able to improve the efficiency of the wing. However, in order to improve the lift on drag (L/D) ratio of the wing over the entire wing, the MTE alone was not enough, as seen in Figure 4.1, where results are expressed in terms of drag coefficient (C_D) variation with lift coefficient (C_L). From these results, it was able to be observed that for all lift coefficient values, the drag coefficient measured was found to be higher for the MTE than for a fixed wing. For this reason, it was necessary to combine the MTE with a morphing leading edge (MLE) in order to obtain a morphing camber system.

In Figure 4.2, NACA0012 airfoil and NACA4412 airfoil shapes are superimposed. The only difference between these shapes is the camber, while the thickness remains the same along their chord. One airfoil shape can change to another shape via morphing of the trailing edge (TE) and of the LE, while a constant central section is maintained. In Figure 4.3, a gain in the drag coefficient was found for a lift coefficient greater than 0.367 when the shape of the wing changed from an NACA0012 to an NACA4412 airfoil for an angle of attack greater than 2.97° .

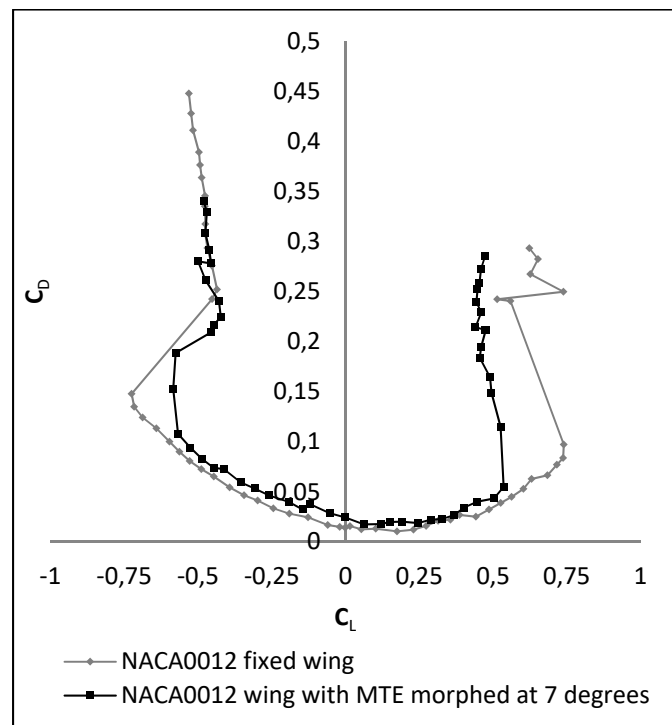


Figure 4.1 Drag coefficient variation with lift coefficient (experimental values). Legend: MTE, morphing trailing edge

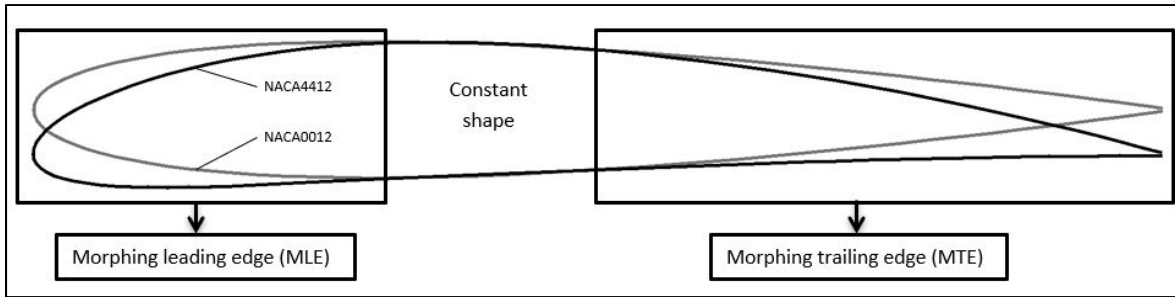


Figure 4.2 Morphing of camber: NACA0012 airfoil (grey) and NACA4412 airfoil (black)

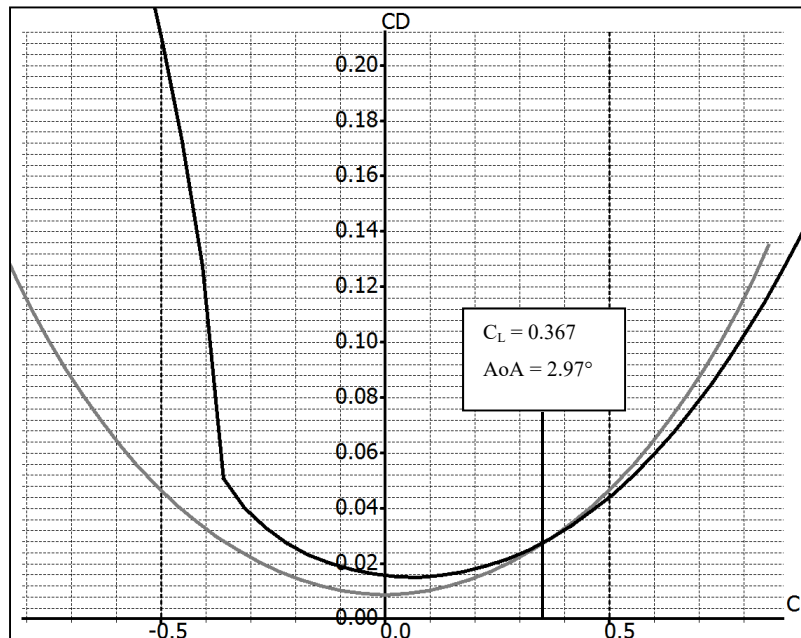


Figure 4.3 Drag coefficient variation with lift coefficient variation for NACA0012 (grey) and NACA4412 (black) (computed values). The curves intersect for a lift coefficient $C_L = 0.367$ and for an angle of attack $AoA = 2.97^\circ$

We found in (Andre, et al., 2017) that for an NACA0012 airfoil, the displacement of a rigid aileron will have the effect of moving the C_L variation with the angle of attack curve to the left or to the right according to the direction (up or down). In fact, if a down displacement of the LE is performed for a given angle of attack, the lift increases. We also found in (Communier, Botez, & Wong, 2019) that a rigid aileron and an MTE induce a decrease in the

stall angle. The use of an MLE allows for the delaying of the stall angle of the wing, thus compensating for the weakness of the MTE.

Several mechanisms of MLEs have already been studied in the literature. For example, Sodja (Sodja, Martinez, Simpson, & De Breuker, 2015) and Rudenko (Rudenko, Radestock, & Monner, 2016) have carried out bench tests of MLE systems.

The Sodja mechanism allowed the LE to be morphed but it required a very high force from its linear actuator. This study aimed to validate the idea that an MLE system can reach the desired shape for drag and noise reduction.

Rudenko's study presented another MLE concept. In his study, the numerical results expressed obtained by finite element analysis (FEA) were compared with the experimental results in terms of the MLE deformations. The MLE mechanism used a circular actuator coupled with internal articulations.

Radestock (Radestock, et al., 2016) and Takahashi (Takahashi, Yokozeki, & Hirano, 2016) have developed mechanisms for MLEs whose performances were tested in a wind tunnel.

Radestock indicated that lift does not change during MLE deformation. This study did not have any effect on the stall angle, since the largest angle of attack studied was 8.68° .

Takahashi proposed a mechanism combining the MLE and the MTE. This combined mechanism was tested in a wind tunnel, and the results indicated that the deformation of the camber could increase the lift coefficient by 1 compared to the lift coefficient values before deformation. However, bumps were observed on the lower surface of the test wing which could have increased its drag. Takahashi confirmed that the combination of the MTE with the MLE would allow the lift coefficient to significantly increase. A study of the drag of the system is needed to determine its effectiveness compared to a conventional wing.

Our Laboratory of Applied Research in Active Controls, Avionics, and AeroServoElasticity (LARCASE) team has a long history in the field of morphing wings. Thus, the LARCASE team collaborates with major players in the aeronautical engineering sector of Montreal. Through the Consortium of Research and Innovation in Aerospace in Quebec (CRIAQ) projects, several studies have been conducted with major research consortiums (CRIAQ 7.1 (Popov, Grigorie, Botez, Mamou, & Mebarki, 2010), (Tchatchueng Kammegne, Grigorie, Botez, & Koreanschi, 2016)) and CRIAQ MDO 505 (Koreanschi, et al., 2016), (Koreanschi, Sugar-Gabor, & Botez, 2016), (Michaud, Joncas, & Botez, 2013), (Botez, et al., January 2017), (Concilio, Dimino, Pecora, & Ciminello, January 2016), (Pecora, Barbarino, Concilio, Lecce, & Russo, 2011))) and internal projects have been conducted at the LARCASE laboratory, such as one project on the morphing of a wing equipped with an ATR-42 airfoil (Gabor, Koreanschi, & Botez, 2012).

4.2 Design of the MLE

The MLE had to be a simple and easy-to-manufacture system. We therefore limited ourselves to the use of materials and actuators common in large model unmanned aerial vehicle (UAV) designs because of the fact that this system is mainly intended for UAV usage. The wing airfoil used for the design of this system was the NACA0012. This airfoil was symmetrical and thus allowed us to identify if a variation in its aerodynamics performances according to the angle of attack resulted from a manufacturing defect (dissymmetry) or from the behavior of the MLE system. An airfoil thickness of 12% of the chord allowed for servomotor installation inside the wing.

To facilitate the deformation of the wing surface of the MLE system, the wing surface does not contribute to the structural strength of the wing. Hence, the main spar of the wing had to be designed to withstand all the aerodynamic loads that the wing would be subjected to during tests in the wind tunnel. Figure 4.4 shows the internal structure of the wing, including its main spar.

The MLE deformation is given by the deformation of three ribs, as seen in Figure 4.4, with the control rod linking these ribs. A servomotor-type actuator moves the tip of the LE via a control arm, while the flexibility of the rib is ensured by six slits regularly spaced between the main spar and the anchor point at the LE. The widths of the slits were calculated according to the desired deformation while the remaining thickness of the rib should have been able to withstand the shear forces induced by the aerodynamic pressures around the wing. Figure 4.5 represents the central rib of the wing in which the servomotor is fixed.

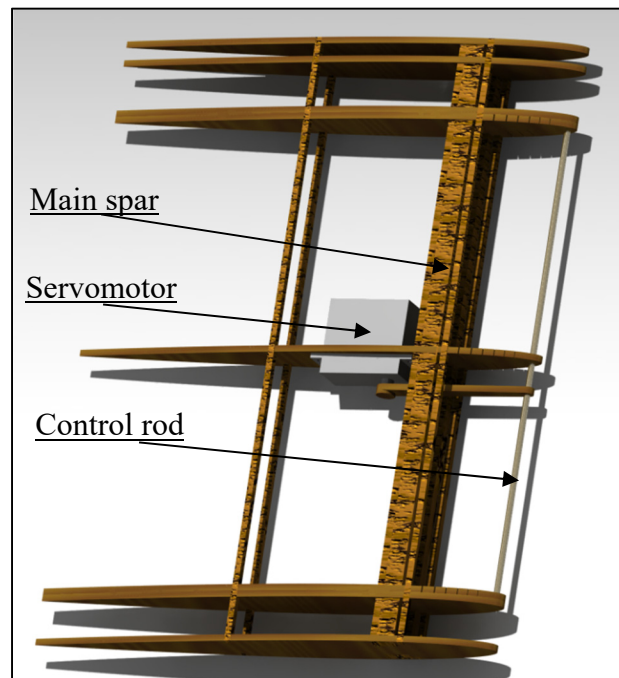


Figure 4.4 Internal structure of the wing

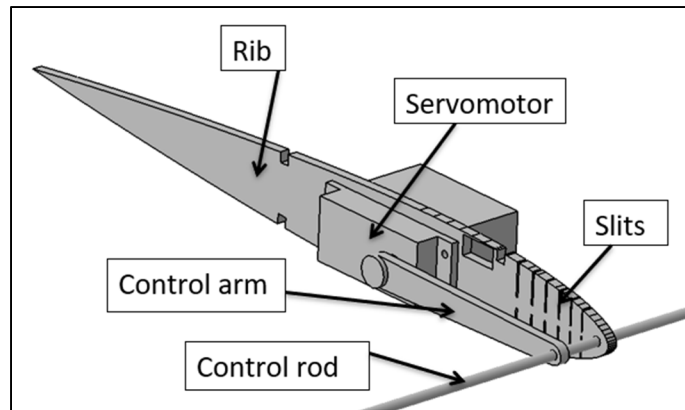


Figure 4.5 Morphing leading edge (MLE) system

The servomotor moves a rod vertically. This rod is connected to the ribs that are desired to deform. Thus, all three ribs connected by the rod move together thanks to the control arm, as seen in Figure 4.6.

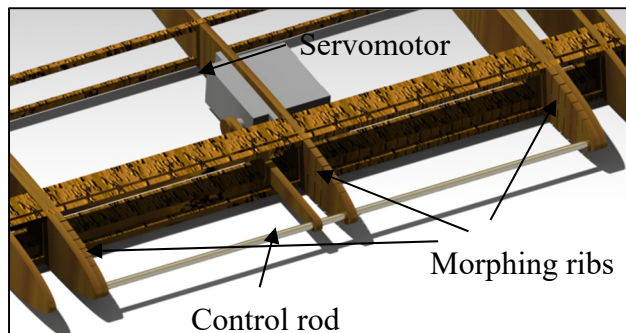


Figure 4.6 Connected morphing ribs with the control rod

The MLE only has one control arm, as the rigid surface of the wing ensures that there is no twist in the MLE and that the three ribs move together with the same displacement.

To allow the control arm to move the LE through the main spar, the main spar is composed of two beams. One beam is connected to the inner surface of the wing and the other beam is connected to the upper surface of the wing. As the structure is designed to have symmetrical behavior in the wind tunnel, the two beams have the same dimensions (Figure 4.7).

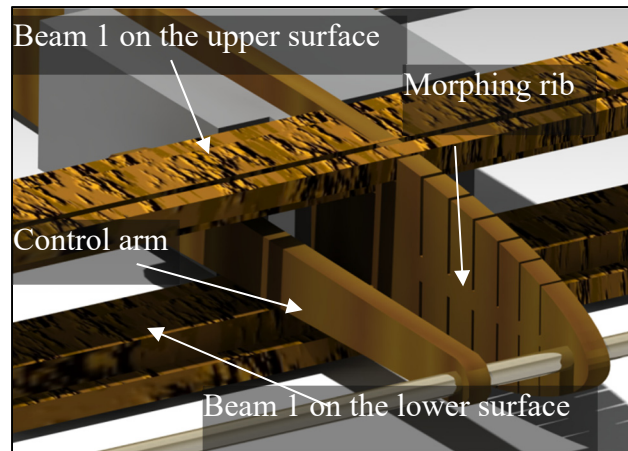


Figure 4.7 Control arm through the main spar

In order to allow the LE to morph, slits were placed on the surface of the wing, corresponding to those on the ribs (Figure 4.8).

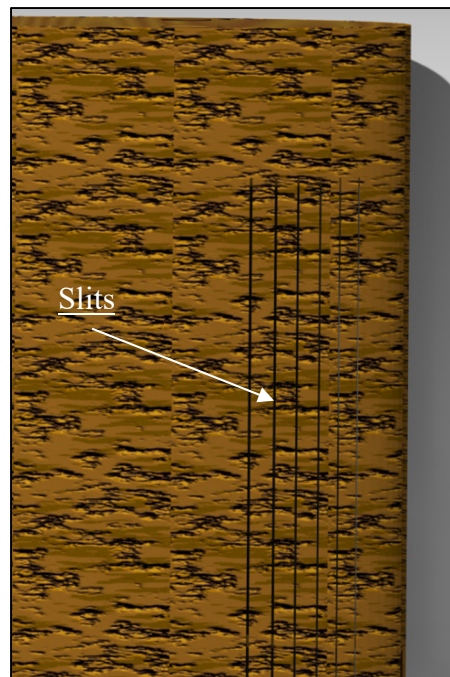


Figure 4.8 Slits on wing surface

However, the presence of slits degrades the flow of air around the wing. To solve this problem, the wing was covered with a sheet of heat-shrinkable plastic such as MonoKote®. The sheet was placed in such a way that the motion of the LE was left free, in order to allow the morphing of the LE. This sheet contributed to the formation of slight humps at the level of the slits. This design, which involved covered slits, was not perfect, but as seen in Figure 4.9, it generated less drag than when leaving the slits opened and just a little more drag than when leaving the slits closed (i.e., when the slits did not have humps on their surface). The values presented in Figure 4.9 were obtained during wind tunnel tests on the MTE at a speed of 15 m/s (Communier, Botez, & Wong, 2019). It is important to mention the fact that the configuration which kept the slits closed cannot be used because it does not allow the LE to be morphed.

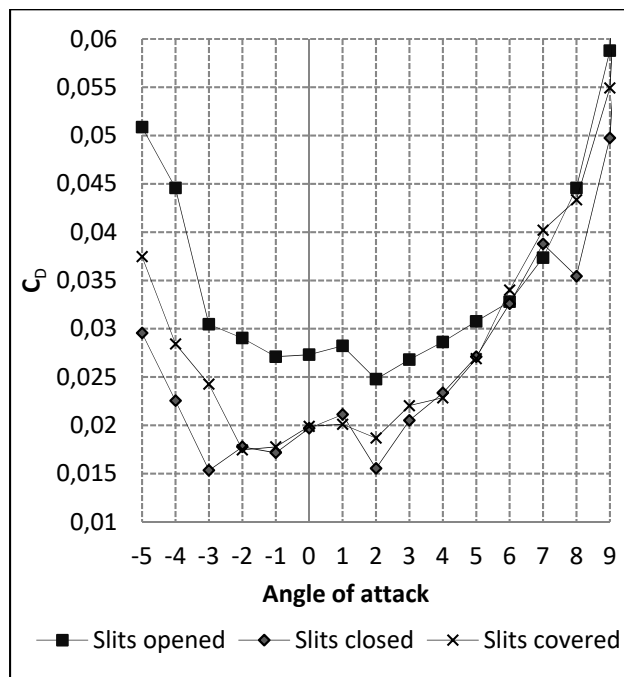


Figure 4.9 Impact of the slits on wing drag

In order to test a prototype in the wind tunnel, a wing with the integrated MLE system was designed and manufactured. This wing was provided with a circular base which allowed for its fixation in the test chamber of the wind tunnel. Figure 4.10 shows this wing prototype equipped with an MLE system.



Figure 4.10 Prototype of the MLE for wind tunnel testing

4.3 Structural Analysis of the MLE System

The size of the slits is usually determined by four parameters: the width of the slit l , the depth of the slit p , the distance between the slit and the LE L , and the airfoil thickness e (Figure 4.11). The parameter t represents the thickness of material remaining at the bottom of a slit and is defined by Equation (4.1), as seen in Figure 11

$$t = e - 2 * p \quad (4.1)$$

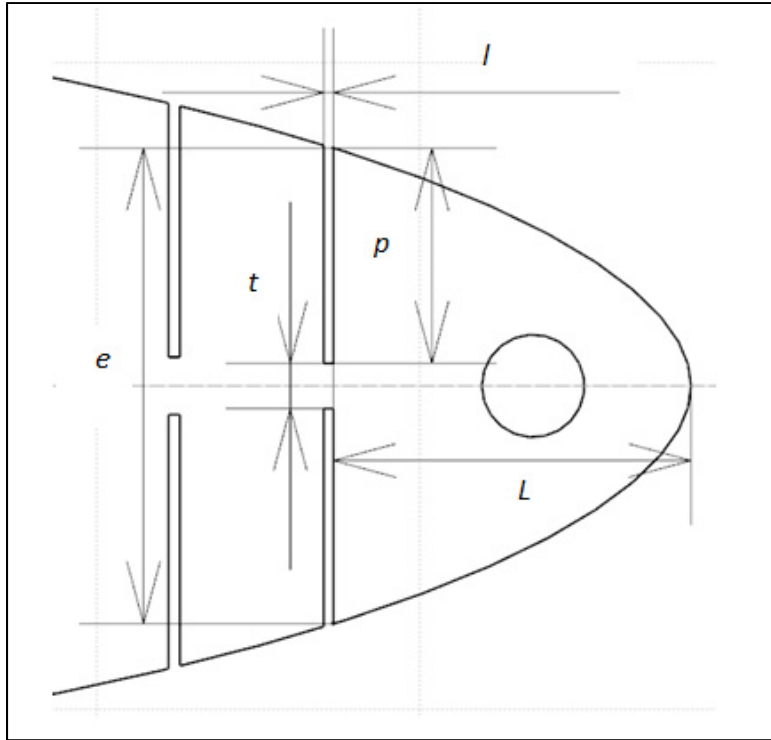


Figure 4.11 Slit parameter definitions. l = width of the slit, p = depth of the slit, L = distance between the slit and the LE, e = airfoil thickness and t = thickness at bottom of the slit

Since $L \gg t$, according to the compliant mechanism's theory (Howell L. L., 2001), we can assume that the bottom of the slits acts as a pivot link. Hence, the maximum rotation allowed by the slits can be calculated from Figure 4.11, as follows:

$$MLE \text{ angle} = \tan^{-1} \left(\frac{l}{p} \right) \quad (4.2)$$

For the determination of t , FEA using CATIA V5 was performed on the design of the MLE. In the FEA, the maximum value of t is dependent on the maximum torque of the servomotor. To ensure the maximum strength of the ribs, the value of t was determined so that the servomotor could deform the ribs until the slits closed on themselves while maintaining the values of aerodynamic loads applied to the MLE. In order to take into account aerodynamic loads applied to the wing when using FEA with CATIA V5, a methodology was developed at

LARCASE ((Communier, Flores Salinas, Carranza Moyao, & Botez, 2015), (Communier, Botez, & Wong, 2017)]. Figure 4.12 shows the MLE with the aerodynamic load applied on its surface. The aerodynamic loads were obtained with XFLR5 software and then were imported into CATIA V5.

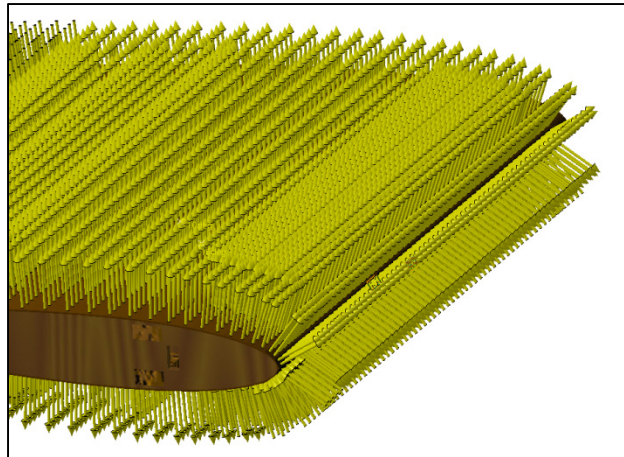


Figure 4.12 MLE with the aerodynamic loads around the wing

The mesh of the pieces that deform and that of the other pieces (rib, arm, and rod) are fine in order to obtain an accurate distribution of the constraints. The mesh of each part was generated with the tool “OCTREE Tetrahedron Mesh” with parabolic elements. The rib mesh had a “global size” of 0.15 inches and a “local size” around the slits of 0.02 inches. The embedding of the assembly was placed on the two holes corresponding to the position of the main spar. The rib was connected to the control rod with the function “slider connection mesh”. The control rod had a mesh of a “global size” of 0.05 inches. The control arm was connected to the control rod with the function “pressure fitting connection mesh”. It was modelled with a mesh which had a “global size” of 0.1 inches and with a local mesh at both ends which had a “local size” of 0.05 inches. The control arm was connected with the servomotor with two functions of “slider connection mesh”. The servomotor had the largest global mesh of 0.25 inches because it did not deform. The servomotor was fixed to the rib with four function “contact connection meshes”. (Figure 4.13). In order to impose an angle of rotation for the servomotor head, a “rigid virtual part” was added on the control arm,

connected with the servomotor head. A function “user-defined restraint” was placed on the “rigid virtual part” with a restraint on the rotation corresponding to the axis of the servomotor head. Finally, an “enforced displacement” was placed on the “user-defined restraint” with the rotation that was needed for the FEA. In Figure 4.13, the rotation angle was set to -5° to obtain a down motion of the leading edge. The mesh in Figure 4.13 had a total of 61,393 elements.

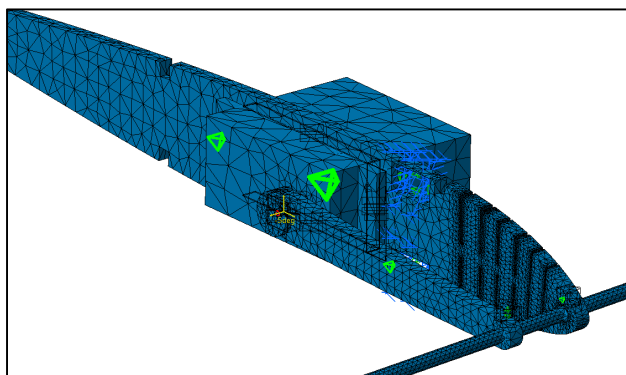


Figure 4.13 Finite element analysis (FEA) structural mesh of the MLE system

During the FEA, the input was the “angle of the servomotor head” in degrees and the output was the “constraint” in the wood parts (ribs and control arm) in MPa (color from blue to red), as shown in Figure 4.14. The components that were the most stressed were the “control arm” and the “ribs”. The stresses on the rib were concentrated on the slits. As wood was used for the MLE design, the maximum stresses before the rib broke were around 70 MPa. The maximum stresses found in the control arm were around 30 MPa. Hence, the control arm was able to send the rotation of the servomotor to the MLE. Concerning the slit, this FEA did not give good results as the material in CATIA V5 was an isotropic one but the “wood” used for the ribs was “orthotropic”, and “orthotropic material 3D” was not available for computation. As the sizes of the slits were set following our design with the MTE, the flexibility of the ribs should have been good. A static test of the flexibility of the ribs before wing manufacturing was done to ensure that the MLE would deform with the full amplitude desired.

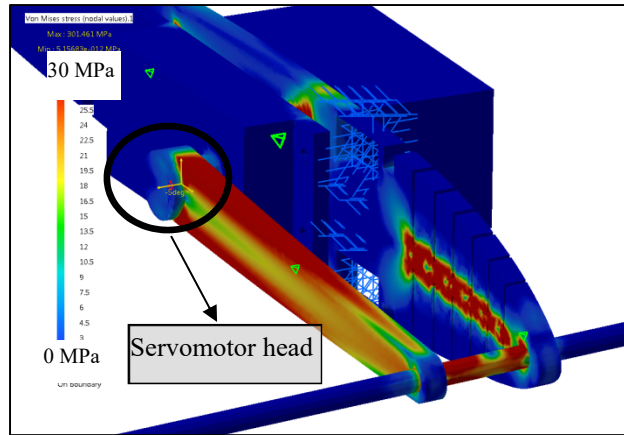


Figure 4.14 FEA of the Structure of the MLE system

The contribution of each slit in the displacement y of the LE tip was able to be calculated with Equation (4.3), i.e.,

$$y = \frac{(l \times L)}{p} \quad (4.3)$$

Table 4.1 shows the dimensions of the parameters e , t , l , p , L , MLE angle and y , of the six slits. These dimensions correspond to a “reference” wing chord of 10 inches (25.4 cm). The definitions of these parameters are given in Figure 4.11.

Table 4.1 Dimensions of the slits

Slit number	e (in)	t (in)	l (in)	p (in)	L (in)	MLE angle (rad)	y (in)
1	0.579	0.055	0.012	0.262	0.436	0.046	0.020
2	0.682	0.070	0.014	0.306	0.623	0.046	0.029
3	0.765	0.085	0.018	0.340	0.817	0.053	0.043
4	0.842	0.100	0.021	0.371	1.037	0.057	0.059
5	0.902	0.115	0.024	0.394	1.258	0.061	0.077
6	0.957	0.130	0.026	0.413	1.507	0.063	0.095

By use of Equation (4.4) and the parameters values shown in Table 4.1, the maximum displacement of the LE was able to be calculated by adding the contribution from each of the six slits, i.e.,

$$\text{Maximum MLE displacement} = \sum_{i=1}^6 y_i = 0.322 \text{ in (8.18 mm)} \quad (4.4)$$

The value of this total displacement value was able to be numerically validated using the FEA of a morphed rib. To obtain the maximum displacement of the MLE, its corresponding angle needed to be found. Thus, the angle of the servomotor head was tuned to find the maximum displacement angle when all the slits were closed (Figure 4.15). Following this operation design using CATIA V5, the servomotor head angle that gave the maximum displacement of the MLE was found to be 10° .

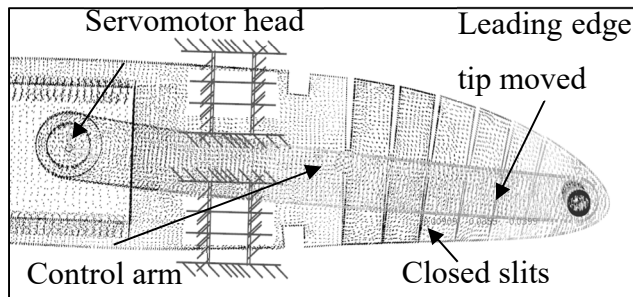


Figure 4.15 Maximum displacement of the MLE tip

Thus, for an angle of the servomotor head of 10° , the displacement of the MLE was obtained by calculating the z component of the displacement of the MLE tip node. As seen in Figure 4.16, the absolute maximum displacement computed using FEA is 0.333 was found to be (8.46 mm). A relative error of 3.4% was found for the MLE maximum displacement calculated with Equation (4.4) versus the maximum displacement obtained using CATIA V5 software. This small relative error shows that the method of calculation used for the maximum displacement of the MLE can be considered a very good method. This method allowed us to design the MLE with a desired maximum displacement without needing an FEA. This method might therefore be used in future research.

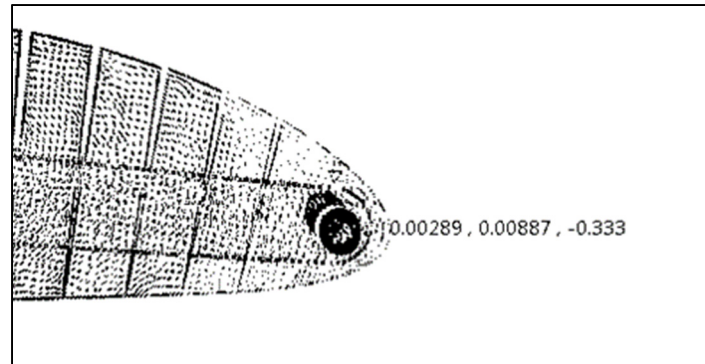


Figure 4.16 Maximum displacement values of the MLE tip

As seen above, no optimization process was used for this dimensioning, as the objective of this work until now was to obtain a functional MLE system. After the demonstration of the functionality of the MLE system, optimization to increase the amplitude of the deformation and to further to reduce the required power for its obtention was realized. The displacement of the MLE tip obtained using FEA (Figure 4.16) was compared with the MLE tip displacement obtained used the test wing during wind tunnel tests, as seen in the following sections.

4.4 Experimental setup of the MLE system

All tests were carried out in the Price–Païdoussis subsonic wind tunnel of the LARCASE ((Tchatchueng Kammegne, Grigorie, Botez, & Koreanschi, 2014), (Koreanschi, Sugar-Gabor, & Botez, 2016)) (Figure 4.17). This tunnel is an open circuit wind tunnel 40 feet in length. The wind tunnel consists of a centrifugal fan, a diffuser and settling chamber, a contraction section, and a working section. The dimensions of these different sections are indicated in Figure 4.18. The test section measured 3 feet in width, 2 feet in height and 4 feet in length (Figure 4.19). In this wind tunnel, testing was done for speeds between 6 m/s and 35 m/s. The measurements presented in this section were made during wind tunnel testing at a speed of 20 m/s and at an air density of 1.18 kg/m³. A more detailed description of the wind tunnel and its method of calibration can be found in (Ben Mosbah, Salinas, Botez, & Dao, 2013).



Figure 4.17 Test wing in the Price - Païdoussis subsonic wind tunnel

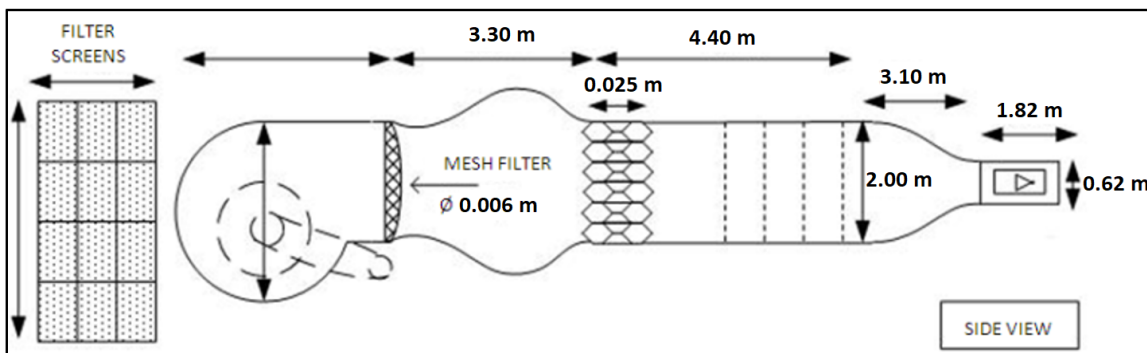


Figure 4.18 Price - Païdoussis subsonic blow down wind tunnel dimensions

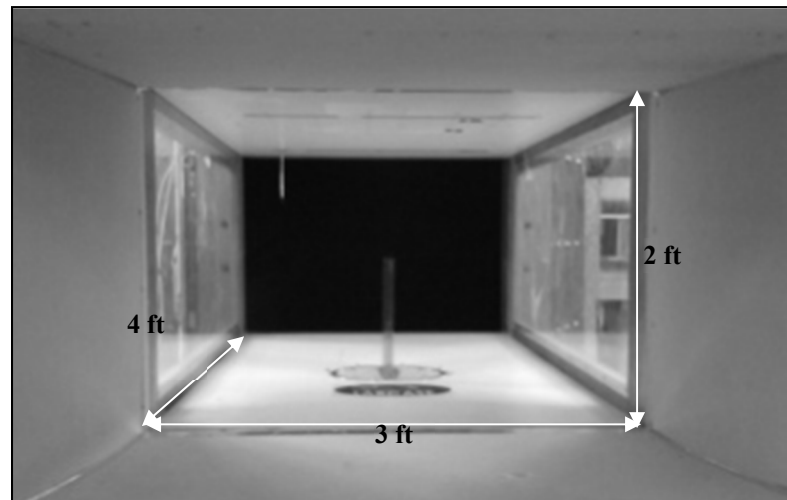


Figure 4.19 Section of the Price-Paidoussis subsonic wind tunnel of the Laboratory of Applied Research in Active Controls, Avionics, and AeroServoElasticity (LARCASE)

The aerodynamic loading scales installed in the wind tunnel measured the forces and moments experienced by the objects studied in the test section (Machetto, Communier, Botez, Carranza Moyao, & Wong, 2017). The aerodynamic loading scales consisted of a turntable controlled by a stepper motor (Table 4.2) assembled on a force and torque (F/T) sensor. An Omega 160 F/T sensor (Table 4.3) from ATI Industrial Automation was used in the aerodynamic loading scales designed and manufactured in house.

Table 4.2 NEMA 23 Bipolar Stepper product specification

Motor Type	Bipolar Stepper	Recommended Voltage	12 V DC
Manufacturer Part Number	57STH56-2804MB	Rated Current	2.8 A
Step Angle	0.9°	Coil Resistance	900 mΩ
Step Accuracy	±5%	Phase Inductance	4.5 mH
Holding Torque	12 kg cm	Shaft Diameter	1/4"
Rated Torque	11.2 kg cm	Rear Shaft Diameter	3.9 mm
Maximum Motor Speed	2150 RPM	Mounting Plate Size	NEMA23
Acceleration at Max Speed	80 0001/16 steps/sec ²	Weight	695 g
Number of Leads	4	Wire Length	300 mm

Table 4.3 Range and resolution for ATI Omega 160 force and torque (F/T) sensor. F_{x,y,z} represent the forces and T_{x,y,z} represent the torques

SI-1000-120 US-200-1000	F _x , F _y	F _z	T _x , T _y	T _z
Sensing Ranges	1000 N (200 lbf)	2500 N (500 lbf)	120 Nm 1000 lbf-in	120 Nm 1000 lbf-in
Resolution	1/4 N 1/32 lbf	1/4 N 1/16 lbf-in	1/40 Nm 1/8 lbf-in	1/80 Nm 1/8 lbf-in

This aerodynamic loading scales allowed the dynamic reading of the loads and thus their measurements for several flight conditions in terms of angles of attack, Reynolds numbers, and Mach numbers without stopping the running of the wind tunnel between each measure. In addition, the sensor was able to read high forces and moments (Table 4.3), and, by use of filters, was also able to read very small forces (0.01 N). The ability to read very small forces is necessary to measure the drag forces acting on the test wings. The high force reading was used to measure the drag of large objects such as a surveillance radars from FLIR Systems,

whose drag measurements were also made in the LARCASE Price–Païdoussis wind tunnel. Figure 4.20 shows the internal structure of the aerodynamic loading scales.

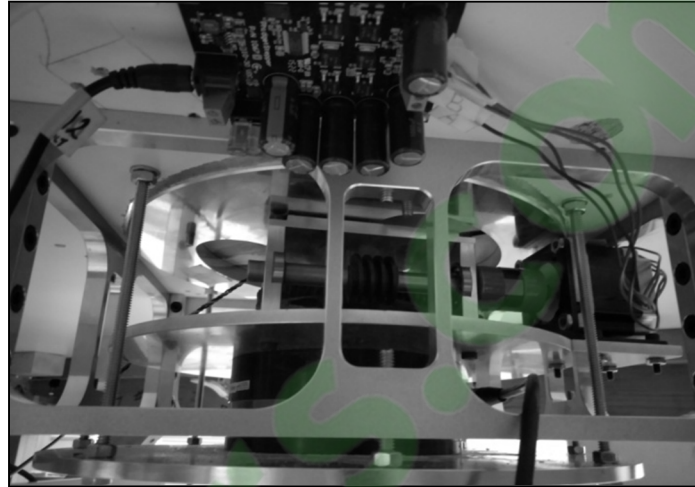


Figure 4.20 Internal mechanism of the aerodynamic loading scales

The upper part of the aerodynamic loading scales was a hollow tray used for the installation of objects to be studied in the wind tunnel (Figure 4.21). In order to be installed on the aerodynamic loading scales, the objects to be tested had to have their discs on which they are installed have a diameter of 10.7 inches and a base 0.5 inches thick. The disc had to be fixed at the basis of the aerodynamic loading scales with four screws.

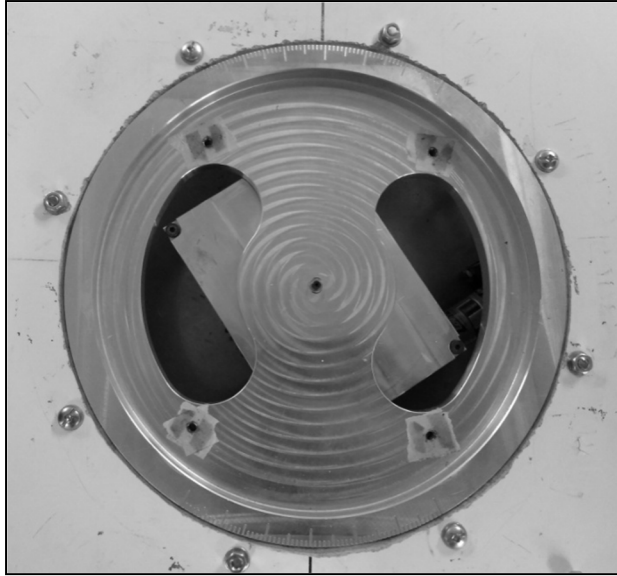


Figure 4.21 Upper disc of the aerodynamic loading scales

The wing used for subsonic wind tunnel testing had a 12 inch span and a part of it (of 0.5 inches) was embedded into the base shape as a disc; thus, the span exposed to the airflow was 11.5 inches. The wing chord was chosen to be 10 inches.

The LE could not be morphed over the entire span; its MLE section had a length of 9.5 inches and covered over 20% of the wing chord. Figure 4.22 shows the leading edge of the MLE where the difference of shapes between the fixed and the morphing part of the leading edge can be seen at the root of the wing.

Two wingspan sections, each of them 1 inch at the wing root and at the wing tip, could not be morphed. These two sections made it possible to identify the impact of discontinuities between the morphing section and the fixed sections. This impact was around 0.002 on the value of the drag coefficient. The impact of the discontinuities could also not be neglected especially at small angles of attack, but these discontinuities are also present for classical LE flap or a slat. This impact is not a weakness of the MLE system with respect to the classical system already used.



Figure 4.22 Leading edge (LE) of the prototype in its morphed configuration

A servomotor controls the MLE. The servomotor used is HITEC HS-5685MH, which allows for control of up to a maximum torque of 179 oz/in (12.9 kg/cm) and a maximum current of 2600 mA. The servomotor used an ‘Arduino-uno’ controller. A multi-meter was added to the controller to monitor the current consumed by the servomotor in order to avoid over-consumption that could lead to the servomotor malfunction.

A LabVIEW interface is presented in Figure 4.23. This interface was divided into different sections. The first section allowed the readings of the forces, their variations with respect to the disc angle, and their variation with the command sent to the servomotor (Figure 4.24). All the graphs showing these variations are plotted in real time in one LabVIEW section. These plotted graphs were able to be exported to a text file for analysis of the results. Another section of the LabVIEW interface was dedicated to the control of the disc angle (Figure 4.25). The LabVIEW interface was also linked with a PhidgetStepper Bipolar HC control board in order to control the stepper motor of the aerodynamic loading scales (Table 4.4).

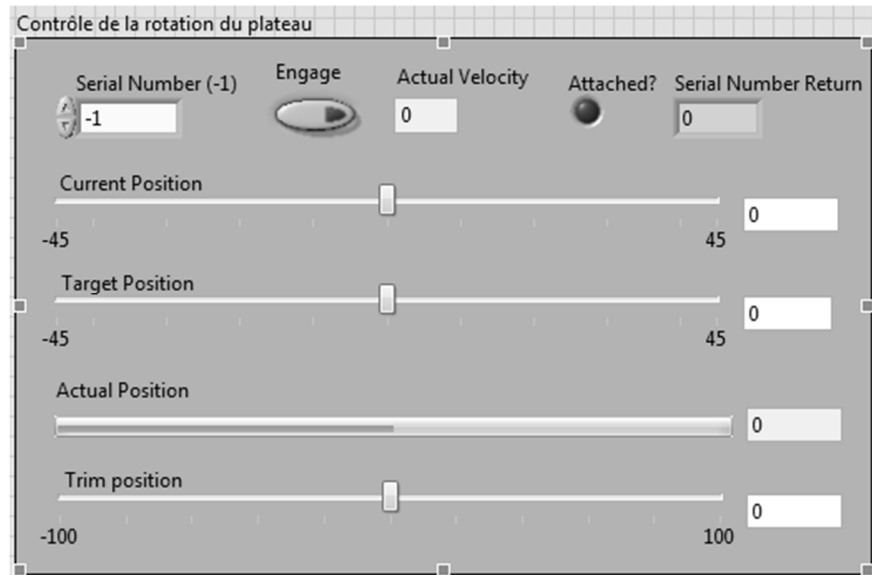


Figure 4.25 Disc angle controller

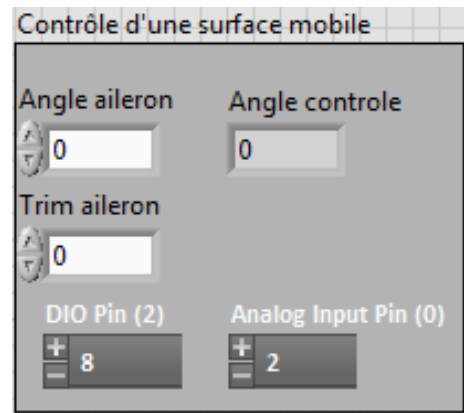


Figure 4.26 Servomotor controller

Table 4.4 PhidgetStepper Bipolar HC product specification

Motor Type	Bipolar Stepper	Available Current per Coil Max	4 A
Number of Motor Ports	1	Supply Voltage Min	10 V DC
Motor Position Resolution	1/16 Step (40-Bit Signed)	Supply Voltage Max	30 V DC
Position Max	$\pm 1E+15$ 1/16 steps	Current Consumption Min	25 mA
Stepper Velocity Resolution	1 1/16 steps/sec	Power Jack	5.5 × 2.1 mm Center Positive
Stepper Velocity Max	250,000 1/16 steps/sec	Recommended Wire Size (Motor Terminal)	12 to 26 AWG
Stepper Acceleration Resolution	1 1/16 steps/sec ²	Recommended Wire Size (Power Terminal)	12 to 26 AWG
Stepper Acceleration Min	2 1/16 steps/sec ²	Operating Temperature Min	-20 °C
Stepper Acceleration Max	1E+07 1/16 steps/sec ²	Operating Temperature Max	85 °C

The results presented in the following section were obtained using the angle of the MLE as the command sent with LabVIEW to the servomotor.

4.5 Wind Tunnel Tests Results

The lift and drag coefficients were calculated from wind tunnel tests measurements using the following equations:

$$C_L = \frac{L}{Q \times S}, \quad (4.5)$$

$$C_D = \frac{D}{Q \times S}, \quad (4.6)$$

where the dynamic pressure Q is given by

$$Q = \frac{1}{2} \times \rho \times v^2, \quad (4.7)$$

where L and D are the lift and drag forces measured by the aerodynamic loading scales, and S is the wing surface.

The performance curves of C_L and C_D were able to be plotted with respect to the angle of attack to observe the influence of the MLE system on the performance of the wing.

Figure 4.27 shows the results expressed as the variation of the lift coefficient as a function of the angle of attack of the wing. The black curve represents this result for the wing without using the MLE system. The gray curves represent the result of deformation for the wing with the MLE system for the angles of rotation of the servomotor head which are equal to 18° and -18° . The angles of 18° and -18° correspond to the maximum MLE system deformations. As the main goal was to identify the best performances of the MLE for the stall angle, these maximum MLE deformation angles were chosen for this study. Note that during a deformation of the MLE, the stall angle of the wing varies. Thus, a positive (downward) deformation will delay the stall angle of the wing (18°) and a negative (upward) deformation will advance the wing stall angle (12°). This result obtained for the MLE's behavior corresponds to the classical behavior of a slat. Figure 4.28 shows the variation of the lift

coefficient as a function of the deformation of the MLE. It was found that the lift coefficient remained constant for MLE angles smaller than the stall angle of the wing, which was approximately 15° . This result obtained for the MLE system shows its improved behavior over a conventional slat behavior which slightly degrades the variation of the lift coefficient when moving the LE (Renukumar, Bramkamp, Hesse, & Ballmann, 2006).

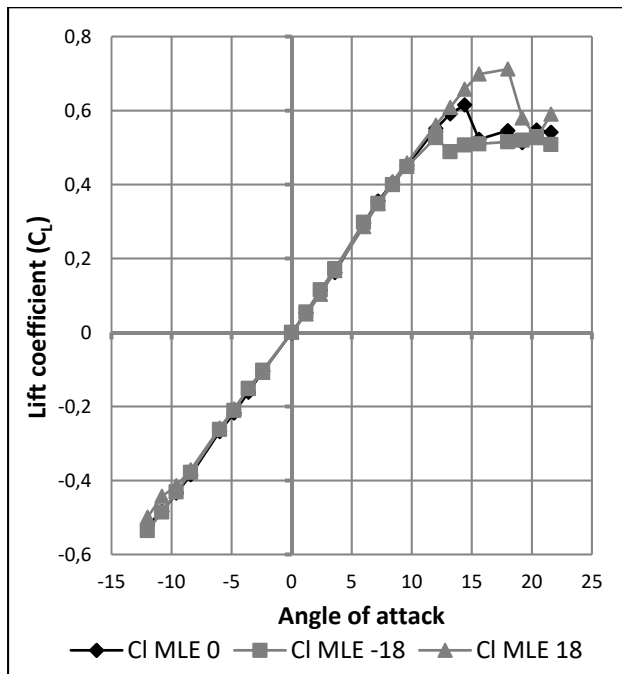


Figure 4.27 Variation of the lift coefficient with angle of attack

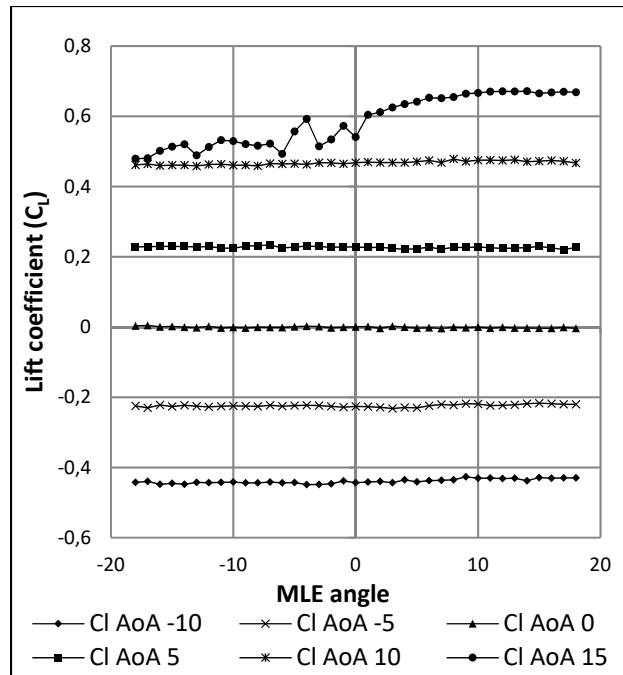


Figure 4.28 Variation of the lift coefficient with morphing angle of the MLE

Figure 4.29 shows the result in terms of variation of the drag coefficient as a function of the angle of attack of the wing. The black curve represents this result for the wing without MLE deformation. The gray curves represent this result for the wing with MLE deformations of 18° and -18° . The maximum inaccuracy of the drag force measurement going up to 0.1 N caused an important fluctuation in the reading of the forces; drag values during tests can be seen to have varied between 0.15 N and 0.6 N for angles ranging -5° to 10° . Despite this inaccuracy, drag curve variation with the angle of attack was able to be traced and its trend can be further observed in Figure 4.29. Apart from the stall angle, which was different for each MLE angle configuration, the drag coefficient did not show significant variation between each MLE angle changed configuration. As seen in Figure 4.30, drag coefficient variation was more due to measurement imprecision than an effect of the MLE.

Since drag reading cannot be improved at this time, drag analysis cannot be pushed any further to quantify it accurately. However, it was observed that the morphing of the LE did not increase the wing drag. As the lift coefficient did not vary according to the MLE angle

and the drag coefficient did not show significant variation according to the MLE angle, the MLE should not have significantly affected the L/D ratio. Due to imprecision in the measurement of drag forces which was found to be smaller than 0.4 N, the variation in the reading of drag forces close to 0 N had too much effect on the L/D ratio in order to obtain a readable curve as that shown in Figure 4.31.

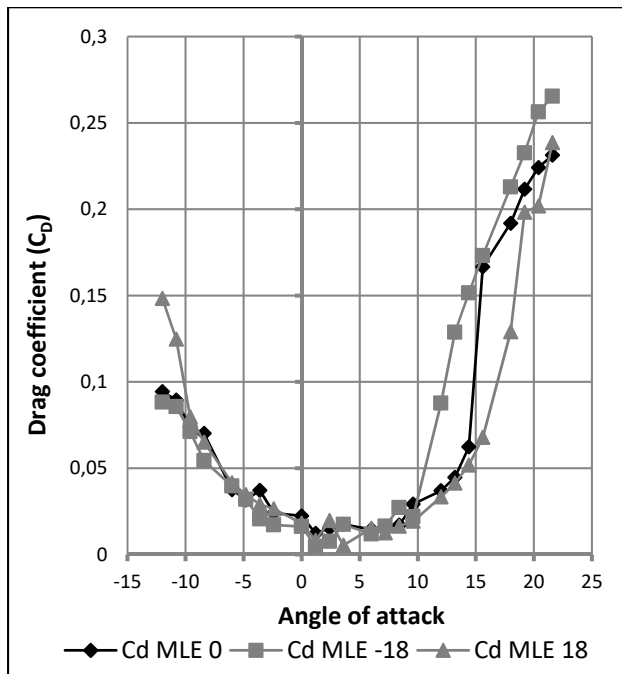


Figure 4.29 Variation of the drag coefficient with angle of attack

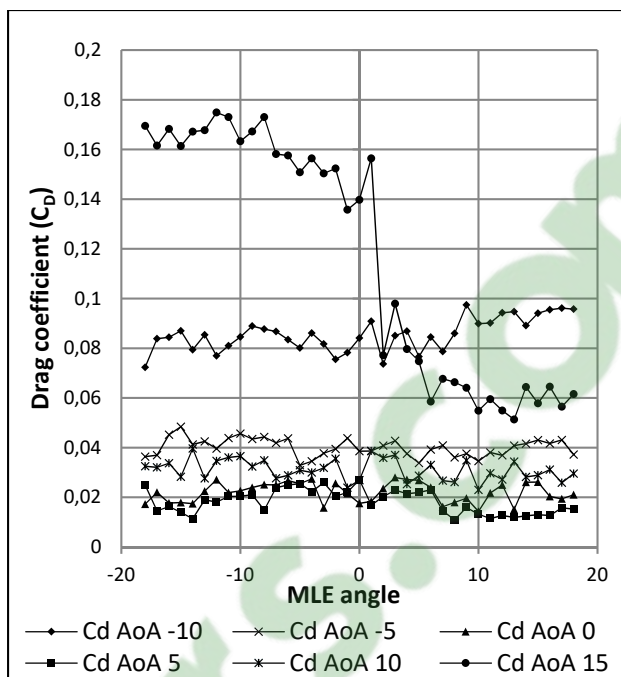


Figure 4.30 Variation of the drag coefficient with morphing angle of the MLE

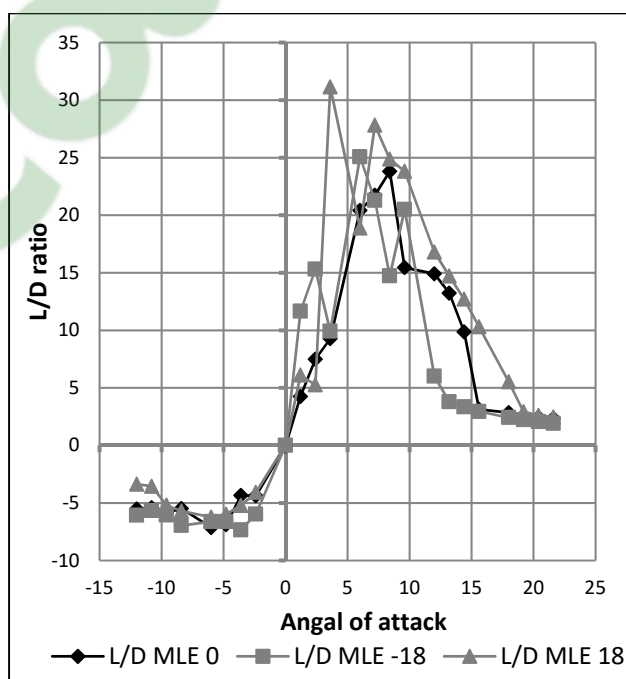


Figure 4.31 Variation of the lift on drag (L/D) ratio with angle of attack

In order to compare the experimental deformation with the deformation previously calculated, the MLE tip displacement was measured. Before adding the sheeting of the wing (ribs alone), the MLE could achieve a maximum displacement of 0.313 inches (8 mm). Once the wing was manufactured, a maximum displacement of 0.157 inches (4 mm) was obtained for both directions of the MLE deformation (positive and negative) during static experimental tests. This experimental deformation is twice as small as the calculated deformation of 0.322 inches (8.18 mm). This fact indicates that after its manufacture, the MLE was not able to reach its calculated maximum displacement.

To increase this displacement, “finishing” at the slots needed to be improved in order to obtain less obstruction against the deformation. In addition, the experimental angle of the servomotor was found to be larger (18°) than the calculated angle (10°). This observation therefore indicates a larger experimental twist of the internal control mechanism than the twist obtained using the FEA.

4.6 Aerodynamic simulation of the wing

The performances of the wing obtained in the wind tunnel were compared with the ANSYS Fluent simulation of the wing. ANSYS Fluent allows for the obtaining of fast and accurate computational fluid dynamics (CFD) results (Triet, Ngoc, & Thang, 2015). The performance criteria considered to compare the experimental results with the simulation results were the lift and drag coefficients, which were dependent on the angle of incidence of the airfoil with respect to the flow. The fluid used was air with a constant density of 1.225 kg/m^3 and a constant viscosity of $1.7894\text{e-}05 \text{ kg/(m}\cdot\text{s)}$. Then, we specified a flow velocity equal to the one used in the wind tunnel, i.e., 20 m/s. The reference values used for the wing geometrical parameters were an area of 0.0625 m^2 and a length of 0.254 m. To obtain comparable results, the distance of the LE tip deformation was defined as 4 mm (Figure 4.32), which corresponds to the maximum displacement obtained experimentally.

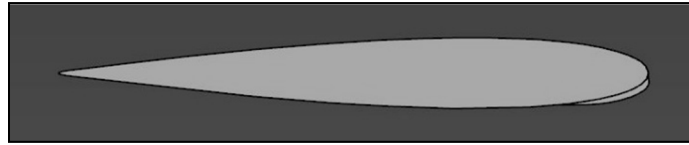


Figure 4.32 Wing with 4 mm displacement of LE tip

The modeling of the wing was carried out in three phases (Noor, Wandel, & Yusaf, 1-3 Jul 2013), and these phases were (1) the design of a 3D model using Catia V5 software (Figure 4.33), (2) the determination of a fluid domain and its mesh computation with ANSYS Meshing (Figure 4.34), and (3) the simulation of aerodynamic coefficients with ANSYS Fluent (Figure 4.35).

The fluid domain used for the simulation corresponded to the fluid in the test section of the wind tunnel. It was generated with the DesignModeler of ANSYS Fluent. The inlet was rounded in order to reduce the volume of the fluid domain and to reduce the computation time.

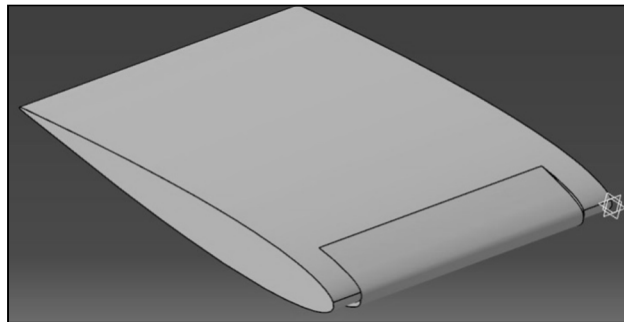


Figure 4.33 Model of wing with MLE

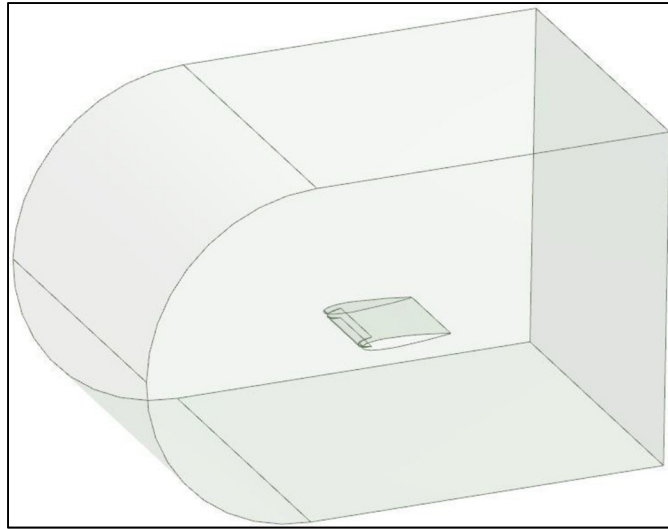


Figure 4.34 Fluid domain of the simulation

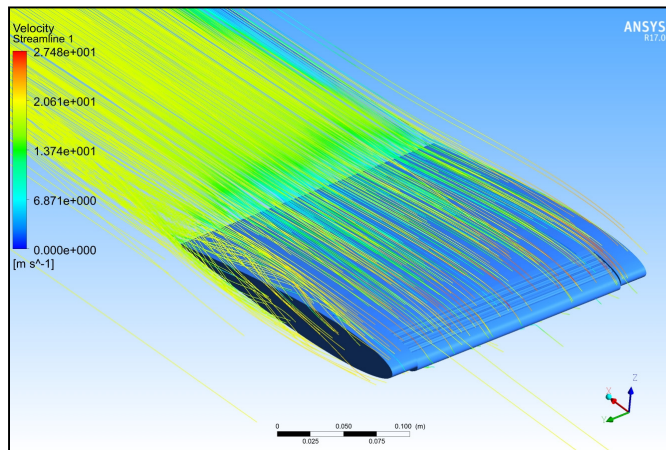


Figure 4.35 Fluent simulation

Morphed wing airfoil coordinates were obtained from an FEA of the system with CATIA V5 (Figure 4.14). From this morphed airfoil it was possible to design a simplified model of the wing which did not consider the slits, was experimentally validated in the wind tunnel, and allowed a first study approximation.

The mesh in Figure 4.36 was designed using the Meshing tool of ANSYS Fluent. The size function “proximity and curvature” was used in order to get a good resolution around the wing (relevance of -10). An inflation around the wing was used in order to get the finest

mesh at the surface of the wing (transition ratio of 0.272, five layers, and a growth rate of 1.2). Finally, a face sizing around the sharp corners (trailing edge, slits, and bumps) was used in order to avoid convergence problems using an element size of 1 mm. For this first simulation, the mesh had around 3,652,638 elements with a satisfying quality (average orthogonality of 0.85 and average skewness of 0.23). Using this configuration, the mesh size was calculated in 10 to 15 min depending on the computer execution speed.

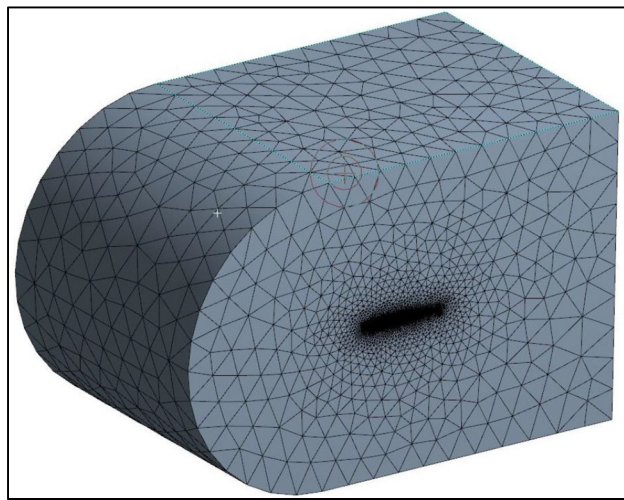


Figure 4.36 Fluid domain mesh of the simulation

The model used in ANSYS Fluent was a combination of the Standard k- ϵ (two equations) (Lauder & Spalding, 1974), (Grisval, Liauzun, & Johan, June 22-25, 1999), (Liauzun, July 2006), (Grisval & Liauzun, 1999)) with standard wall functions (Patankar & Spalding, 1968), (Wolfshtein, 1969)) because this represents a good compromise between calculation time and quality of results. The two equations model was chosen due to the computing capabilities of our computers.

Once a fluid domain was designed and a suitable mesh calculated, it was possible to run simulations at different angles of incidence in order to obtain lift (Figure 4.37) and drag (Figure 4.38) variations with angle of attack of the wing thanks to the monitors in ANSYS Fluent.

The difference between the stall angle calculated with CFD simulations and the stall angle obtained experimentally during the wind tunnel tests was found to be 1° , which corresponds to a difference in maximum lift coefficient value of 0.212. The experimental drag variation with the angle of attack seems to have been shifted with respect to the numerical drag variation with the angle of attack. Indeed, given the observation of the drag variation with the angle of attack of the MLE at 0° deformation (Figure 4.39), there is a shift of the axis of symmetry of 3 degrees relative to the vertical axis at an angle of attack of 0° . The shifting of the drag curve was probably due to the experimental setup, but the exact cause needs to be still determined. As the airfoil used was a NACA0012, the drag variation with the angle of attack should have been symmetrical with respect to the vertical axis at an angle of attack of 0° . The drag variation with the angle of attack is plotted in Figure 4.40, where a vertical offset between the experimental and numerical values can be seen; this indicates that the prototype wing generated more drag than the ANSYS Fluent modeling. In order to obtain modeling which is faithful to the wind tunnel tests, the surface of the wing model needed to be degraded at the LE.

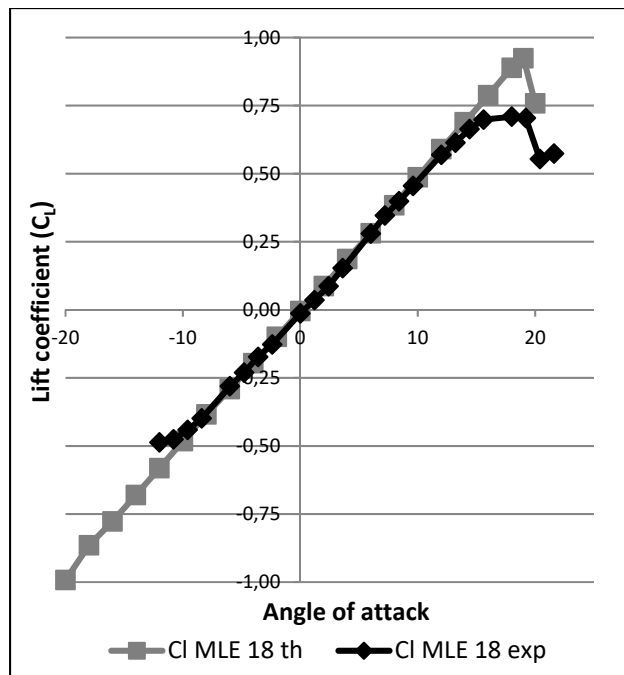


Figure 4.37 Lift coefficient variation with angle of attack

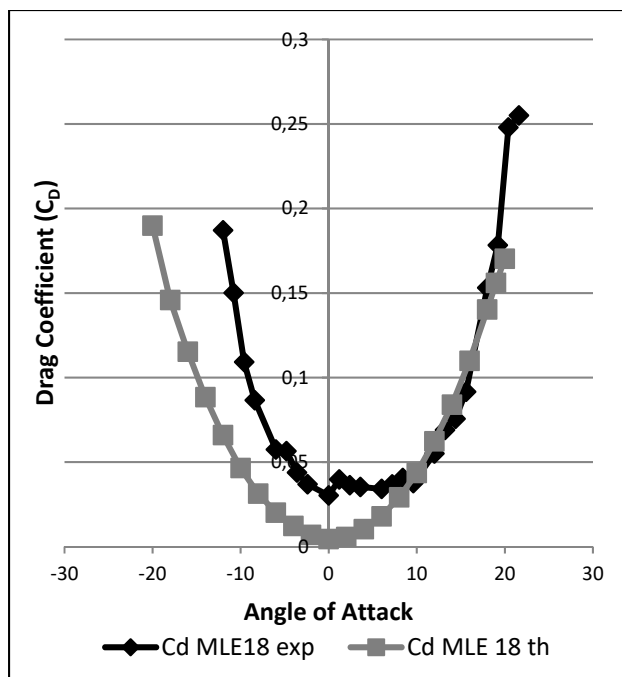


Figure 4.38 Drag coefficient variation with angle of attack

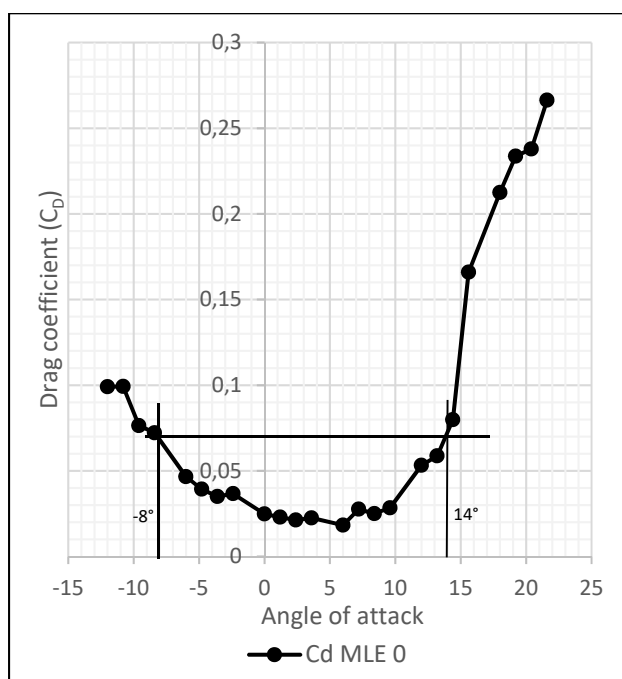


Figure 4.39 Drag variation with angle of attack for MLE at 0°

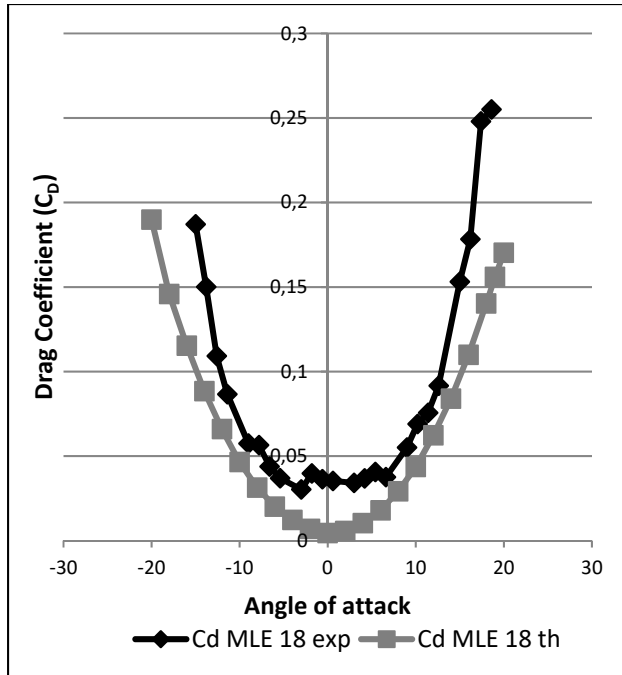


Figure 4.40 Drag coefficient variation with angle of attack with experimental values shift by 3°

Grooves and bumps were added to the surface of the wing's LE (Figure 4.41) to simulate the behavior of the uneven surface of the model due to the slits. The grooves and bumps were defined with a half-circle profile with a radius of 0.5 mm. There were five of each on the inner surface and five of each on the upper surface for a total of 10 grooves and 10 bumps. The size of the mesh elements around the grooves and the bumps was fixed at 0.25 mm. The size of the mesh elements around the rest of the wing was 1 mm.

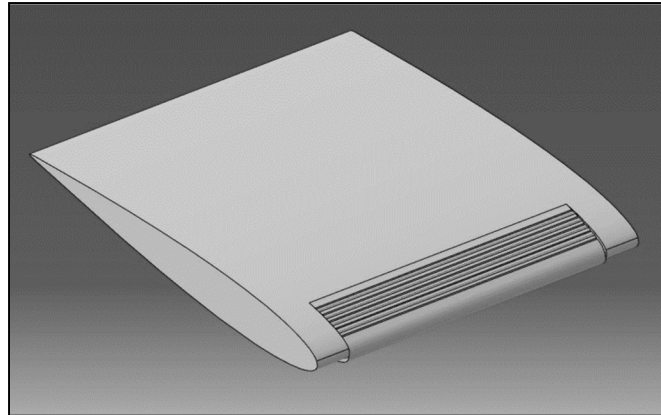


Figure 4.41 MLE with grooves and bumps

Using this new model, which was closer to the real manufactured wing LE than the previous one, we can see in Figure 4.42 that the maximum lift coefficient had values obtained during the simulation which were close to those values obtained during wind the tunnel tests with an error of 0.1% for the maximum lift coefficient value, while the stall angle obtained in the simulation can be seen to have been 1° smaller (17°) than the stall angle obtained following the wind tunnel tests (18°). The modification (consisting of grooves and bumps added to the model) made it possible to obtain a numerical lift coefficient which was close to its experimental value, in the sense that a numerical stall angle was found to be close to the experimental stall angle. For drag variation with the angle of attack, by considering an offset of 3° for its experimental value, the simulated and measured drag coefficient values were found to be very close to each other (Figure 4.43). There was a difference for angle of attack close to 0° that seems to have been due to wind tunnel measurements. It can therefore be concluded that this new model allows a good estimate of the lift and drag coefficients of a wing with an MLE system.

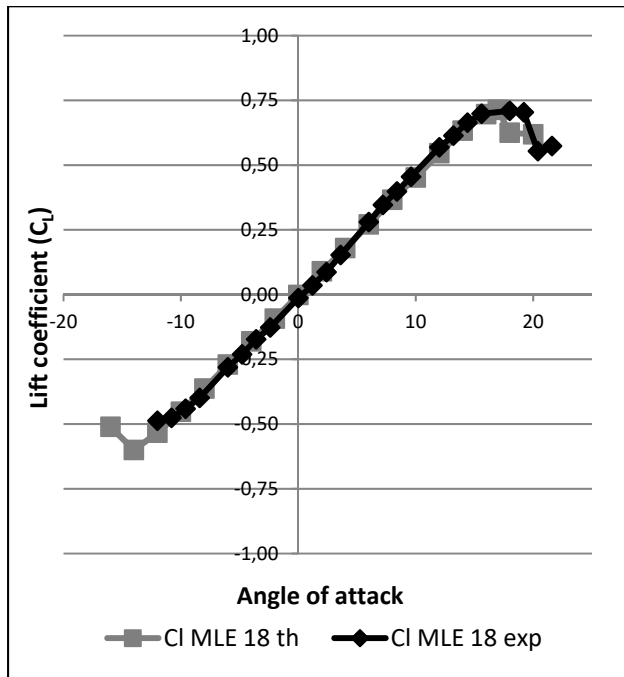


Figure 4.42 Lift coefficient variation with angle of attack for improve modeling

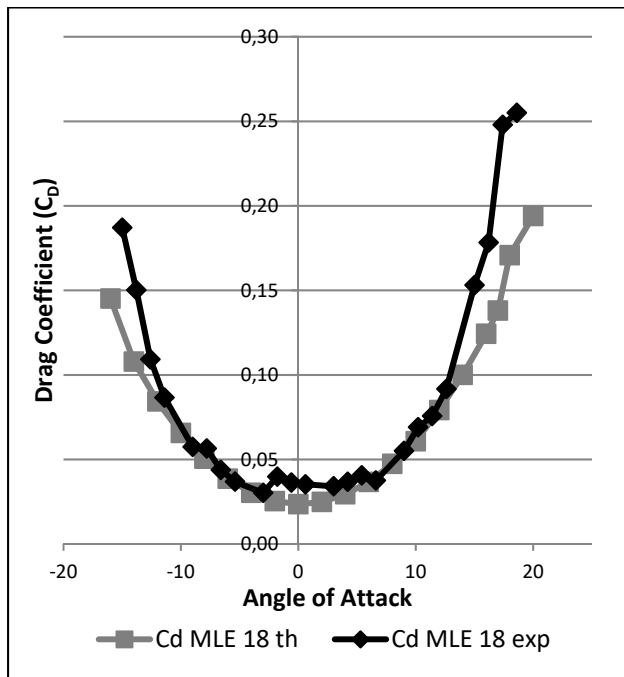
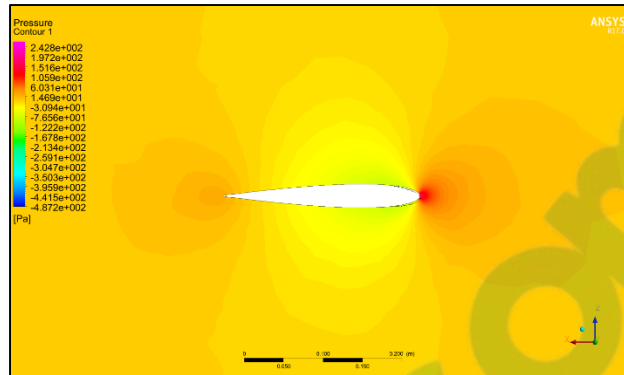
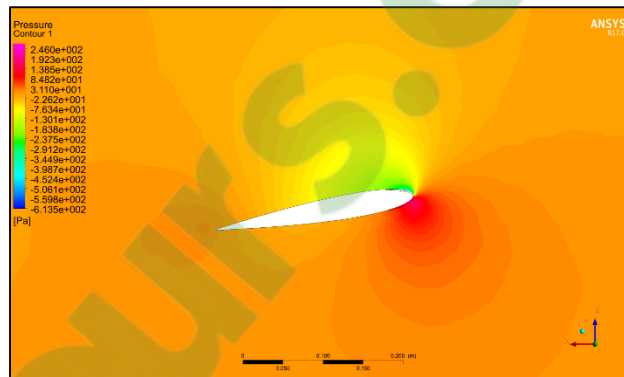


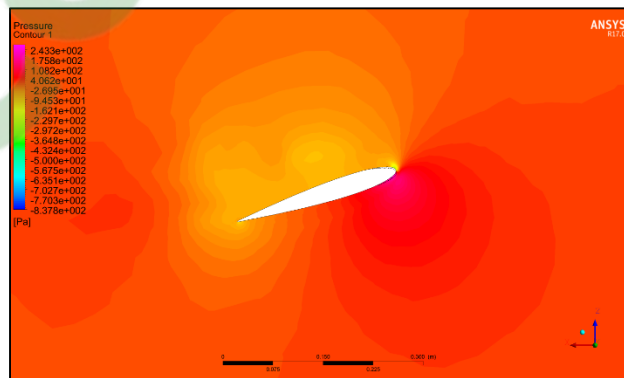
Figure 4.43 Drag coefficient variation with angle of attack for improved modeling



(a)

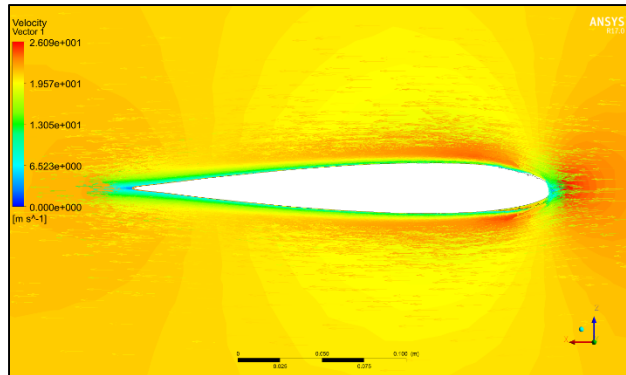


(b)

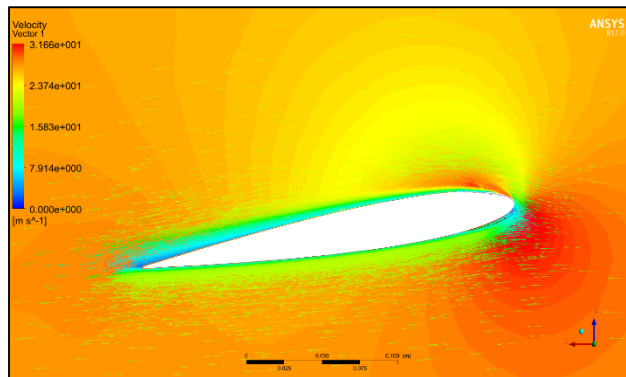


(c)

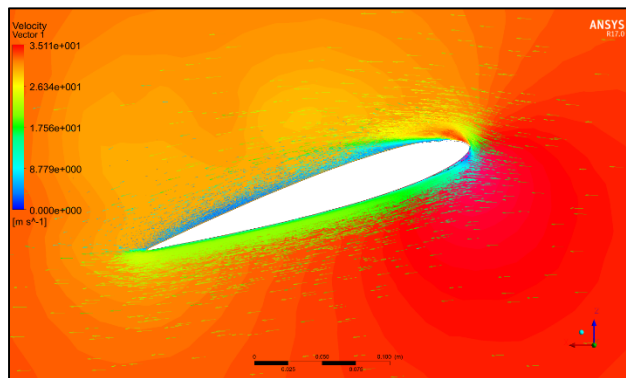
Figure 4.44 Pressure around the wing with MLE at 18° with an airspeed of 20 m/s and (a) angle of attack 0° , (b) angle of attack 10° , and (c) angle of attack 18°



(a)



(b)



(c)

Figure 4.45 Velocity vector around the wing with MLE at 18° with an airspeed of 20 m/s and (a) angle of attack 0°, (b) angle of attack 10°, and (c) angle of attack 18°

Figure 4.44 shows the pressure around the wing in Pascal units for angles of attack of 0° , 10° , and 18° with the MLE at 18° , where the airspeed is 20 m/s and a reference p_0 is of 101 325 Pa. The red color corresponds to an area with high pressures, the orange and yellow colors correspond to areas with low pressure, and the blue color corresponds to an area with high depressurization. For an angle of attack of 0° , the pressures and velocities were the same above and below the airfoil. This behavior was due to the symmetrical shape of the airfoil NACA0012. For positive angles, the pressure can be seen to have been high below the airfoil and low above the airfoil. This behavior allowed the wing to generate the lift required for the aircraft to fly. Figure 4.45 shows the norm of the velocity vector around the wing in m/s for angles of attack of 0° , 10° , and 18° with the MLE at 18° , where the airspeed is 20 m/s. The red vector corresponds to the highest velocity and the blue vector corresponds to the slowest velocity. In Figure 4.45, the acceleration of the airflow is clearly visualized on the top of the LE for angles of attack of 10° and 18° . This acceleration combined with a velocity near 0 below the leading edge generated the lift force of the wing. Figure 4.46 shows the streamlines in the fluid domain for an angle of attack of 8° with the MTE at 18° . The speed close to the walls can be seen to have been close to 0 m/s while the inlet speed was 20 m/s. The streamlines were clearly curved by the presence of the wing. The speed around the leading edge of the wing may have reached 31 m/s.

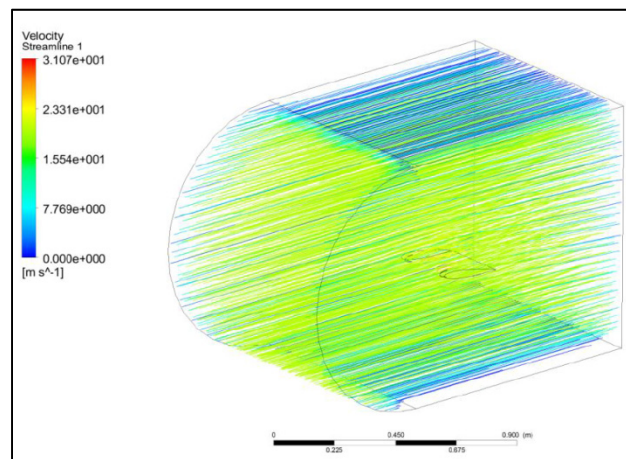


Figure 4.46 Velocity streamlines for an angle of attack of 8° and the MTE at 18°

This comparison between the experimental simulated wing results shows that in order to obtain the same maximum lift coefficient, the LE surface of the simulated MLE had to be degraded compared to a perfect LE. The need for degradation of the LE of the wing model indicates that an improvement of the surface finish of the MLE could increase the impact on the stall angle by delaying it more than with the actual prototype of the MLE. Analysis of the wing using ANSYS Fluent has revealed a good correlation between the simulation and the experimental values of the lift and drag coefficients. By validating these lift and drag coefficient values for the prototype wing in the wind tunnel, our methodology for the simulation of an MLE can be applied to larger scale wings which cannot be tested in our wind tunnel, such as the wings of the UAS-S4 from Hydra Technologies.

4.7 Conclusion and further work

The results shown in this paper regarding analysis of MLE system behavior in a subsonic wind tunnel have shown that this system can act on the stall angle as an LE flap, and thus that an MLE is a good alternative to an LE flap. The simple mechanism of this morphing system using a servomotor makes it possible to keep constant the weight of the wing if LE flaps are already present in the wing. However, it is necessary to consider an increase in the current used by the servomotor. In order to obtain the maximum deformation of the MLE at 20 m/s, the servomotor has been found to need 8.6 W for a voltage of 7.2 V (during wind tunnel testing) with respect to 25.2 mW for a voltage of 7.2 V for a classical LE flap controlled by the same servomotor [1]. The difference in power (8.6 W versus 25.2 mW) comes from the needed morphing of the structure with the MLE while the LE flap would only need to counter the aerodynamic forces that are low for the wing. The design of the MLE presented in this paper has not been optimized yet but it is entirely functional.

The current deformation range of ± 0.157 inches (± 4 mm) for the MLE could be increased, and its power consumption could be reduced, through a better design. The increase of consumption due to the MLE may seem like a big disadvantage, but if the power required for a UAV is considered (~ 10 kW would be assumed for a wingspan of 16.4 feet (5 m)), a

reduction of 1% on the needed thrust (reduction of drag) would save 100 W of power, which is much higher than the additional 8.6 W consumption by the controller.

Author Contributions

As a Ph. D. student, David Communier has done the research presented in this paper. Franck Le Besnerais realized the modeling of the wing with Ansys Fluent software. Ruxandra Botez and Tony Wong are David Communier's research directors.

Funding

This research received no external funding

Acknowledgments

The authors would like to sincerely thank the Natural Sciences and Engineering Research Council of Canada (NSERC) for the Canada Research Chair Tier 1 in Aircraft Modelling and Simulation New Technologies funding, as well as the McGill University professors Dr. Michael Païdoussis and Dr. Stuart Price for the donation of the Price–Païdoussis wind tunnel at the LARCASE, ÉTS.

Conflicts of Interest

The authors declare that there is no conflict of interest regarding the publication of this paper.

CHAPTER 5

DESIGN AND VALIDATION OF A NEW MORPHING CAMBER SYSTEM BY TESTING WITH THE SUBSONIC PRICE – PAÏDOUSSIS WIND TUNNEL

D. Communier^a, R. M. Botez^b, and T. Wong^c

^{a, b, c} Department of Systems Engineering, École de Technologie Supérieure,
1100 Notre-Dame West, Montreal, Quebec, Canada H3C 1K3

Paper published in *Aerospace*, Vol. 7, No. 3, pp. 23, March 2020,
DOI:10.3390/aerospace7030023

Résumé

Cet article présente la conception et les essais en soufflerie d'une cambrure déformable et une estimation des performances sur un véhicule aérien sans pilote. Le système de cambrure déformable est une combinaison de deux sous-systèmes: le bord de fuite déformable et le bord d'attaque déformable. Les résultats de l'étude présente montrent que les effets aérodynamiques des deux sous-systèmes sont combinés, sans toutefois interférer l'un avec l'autre sur l'aile. Le système de cambrure déformable n'agit que sur le coefficient de portance à un angle d'attaque de 0° lors de la déformation du bord de fuite, et uniquement sur l'angle de décrochage lors de la déformation du bord d'attaque. Ce comportement devrait permettre un contrôle individuel du bord d'attaque et du bord de fuite de la cambrure déformable. L'estimation des performances de la cambrure déformable sur un véhicule aérien sans pilote indique que la déformation de la cambrure permet de réduire sa traînée. Ce résultat est dû à l'angle d'attaque plus petit nécessaire pour un véhicule aérien sans pilote équipé du système de cambrure déformable que pour un véhicule aérien sans pilote équipé d'ailerons classiques. Dans l'étude de cas, le système de cambrure déformable a permis une réduction de la traînée lorsque le coefficient de portance était supérieur à 0,48.

Abstract

This paper presents the design and wind tunnel testing of a morphing camber system and an estimation of performances on an unmanned aerial vehicle. The morphing camber system is a combination of two subsystems: the morphing trailing edge and the morphing leading edge. Results of the present study show that the aerodynamics effects of the two subsystems are combined, without, interfering with each other on the wing. The morphing camber system acts only on the lift coefficient at a 0° angle of attack when morphing the trailing edge, and only on the stall angle when morphing the leading edge. The behavior of the aerodynamics performances from the MTE and the MLE should allow individual control of the morphing camber trailing and leading edges. The estimation of the performances of the morphing camber on an unmanned aerial vehicle indicates that the morphing of the camber allows a drag reduction. This result is due to the smaller angle of attack needed for an unmanned aerial vehicle equipped with the morphing camber system than an unmanned aerial vehicle equipped with classical aileron. In the case study, the morphing camber system was found to allow a reduction of the drag when the lift coefficient was higher than 0.48.

5.1 Introduction

In an effort to reduce aircraft fuel consumption, researchers and engineers strive to optimize all aircraft flight phases. To this end, many studies have focused on optimizing aircraft weight (structure and materials), engine efficiency, aircraft trajectories and aerodynamics, etc. The optimization of the aerodynamics of an aircraft is performed by modifying its shapes and/or its surfaces (wings, empennage, etc.). In terms of the shapes of the aircraft surfaces, they could be optimized according to the flight phases (Raymer, 2018). Some research has targeted the modification of the shapes of the surfaces during flight- to adapt them to changing conditions, and phases.

This article presents a prototype of a Morphing Camber System (MCS) that enables an aircraft wing to modify its shape during flight. The MCS is intended to change the wing's lift, which it does by having the lowest possible impact on the aircraft drag. As result, the

morphing of the wing generates a smaller increase in drag than the present increase when classic control surfaces are used. The purpose of the MCS is to reduce the drag of the aircraft by replacing the slats, the aileron and the flaps with a morphing of the internal structure. In this paper, a new method to achieve the morphing of the internal structure is presented. This method consists of using slits on the ribs to make them compliant. Numerous theoretical studies have been carried out on the aerodynamic shape optimization of wing surfaces ((Abdessemed, Yao, Narayan, & Bouferrouk, 2017), (Grisval, Liauzun, & Johan, June 22-25, 1999), (Triet, Ngoc, & Thang, 2015), (Woods, Fincham, & Friswell, 2014, July), (Carossa, et al., 2015)). However, few functional mechanisms were tested (Barbarino, Bilgen, Ajaj, Friswell, & Inman, 2011), Blondeau (Blondeau, Richerson, & Pines, 2003) tested a morphing aspect ratio in wind tunnel, Chanzy tested a morphing trailing edge in wind tunnel and in a flight test with a UAV integrating the morphing system (Chanzy & Keane, 2018), Pecora and al. tested a morphing trailing edge based on a full-scale wing of a civil regional transportation aircraft ((Pecora, Barbarino, Concilio, Lecce, & Russo, 2011), (Concilio, Dimino, Pecora, & Ciminello, January 2016), (Botez, et al., January 2017)), Radestock tested a morphing leading edge mechanism (Radestock, et al., 2016), Woods also tested a morphing trailing edge system using a fish bone concept (Woods, Bilgen, & Friswell, 2014). Numerical optimization studies are generally hindered by their feasibility from a mechanical and thus, practical standpoint. Conversely, studies or “experimental analysis” on morphing mechanisms allow less aerodynamic improvement than is ideal. The main obstacles in the design and testing of a morphing mechanism are generally given by the weight, the power consumption of the morphing mechanism and the elasticity of the wing surface ((Sofla, Meguid, Tan, & Yeo, 2010), (Gandhi & Anusonti-Inthra, 2008)). According to Weisssharr (Weisshaar, 2013), the fact that morphing systems are expensive, that morphing aircraft are heavier than conventional aircraft and that morphing systems are complex and require exotic material is a myth and demonstrated it by reviewing early morphing aircraft history.

In previous studies, our LARCASE team has developed morphing wing mechanisms which, by modifying the upper surface of the wing, allow the flow transition delay between the laminar and the turbulent regimes around the wing ((Tchatchueng Kammegne, Grigorie,

Botez, & Koreanschi, 2016), (Tchatchueng Kammegne, Grigorie, Botez, & Koreanschi, 2014), (Koreanschi, et al., 2016), (Koreanschi, Sugar-Gabor, & Botez, 2016), (Michaud, Joncas, & Botez, 2013), (Popov, Grigorie, Botez, Mamou, & Mébarki, 2010), (Sugar Gabor, Koreanschi, Botez, Mamou, & Mebarki, 2016)). This delay has the effect of reducing the drag generated by the wing.

The present study aims to modify the camber of the wing with the aim to increase its lift coefficient and lift to drag ratio (L/D). It is known that when the lift coefficient is increased, the aircraft can fly with a lower angle of attack, thereby reducing its drag.

5.2 Problem statement

The MCS problem is simplified by dividing the wing into its three sections: the leading edge, the wing box and the trailing edge. Such a morphing system needs two actuating mechanisms to morph the leading edge (Morphing Leading Edge (MLE)) and the trailing edge (Morphing Trailing Edge (MTE)), while the wing box remains fixed.

In this research a NACA0012 airfoil is considered, which will be morphed by the MCS mechanism into a NACA4412 airfoil. This morphing is equivalent to modifying the grey airfoil (NACA0012) to the black airfoil (NACA4412), as shown in Figure 5.1. In this figure, these two airfoils shapes are each divided into three sections: the leading edge, the center box and the trailing edge. The center box is the same constant shape, thus un-modified for both airfoils while the leading and trailing edges are different for both airfoils. The NACA0012 and NACA4412 airfoils were considered because they have the same thickness, and the only difference between their shapes lies in their cambers. This is the reason why this new system is called a “Morphing Camber System” (MCS).

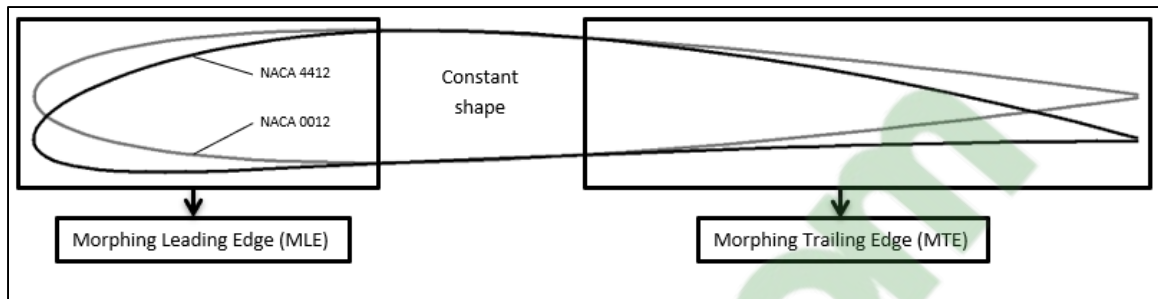


Figure 5.1 NACA0012 and NACA4412 airfoil superimposed

To compare the efficiency of these two airfoils, an analysis of the L/D ratio is not enough. Indeed, an airfoil could have a lower drag and a higher L/D , while having a lower lift, which could be too low to allow the aircraft to fly. The variation of the drag coefficient with the lift coefficient, allows directly visualization of the airfoil having the smallest drag given a constant lift value. Thus, when comparing the variation of C_l with C_d for NACA0012 airfoil versus the NACA4412 airfoil, it can be seen in Figure 5.2 that the NACA4412 airfoil is more efficient than the NACA0012 airfoil for a lift coefficient C_l greater than 0.367.

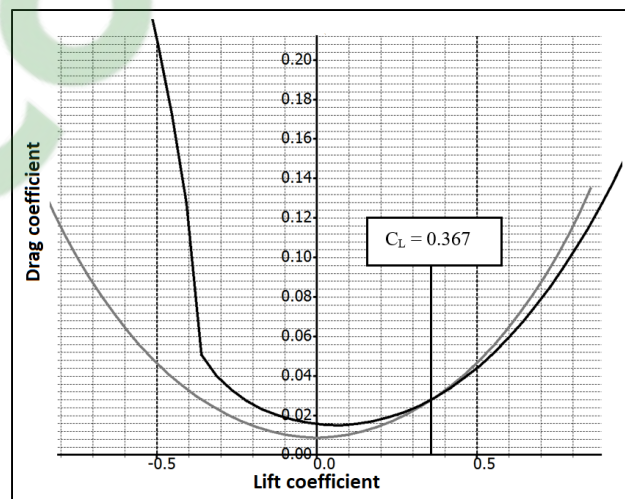


Figure 5.2 Drag coefficient variation with the lift coefficient for NACA0012 (grey) and NACA4412 (black). For $C_L = 0.367$, angle of attack of NACA0012 = 7.8° and angle of attack of NACA4412 = 2.97°

This lift coefficient is obtained for an angle of attack of 2.97° for the NACA4412 airfoil, and of 7.8° for the NACA0012 airfoil. It is therefore possible for an aircraft wing, equipped with an MCS, to increase its lift without having to change the angle of attack but only by changing its shape from a NACA0012 to a NACA4412. Furthermore, as the angle of attack of the aircraft could be smaller with an MCS than with classical wing, there is an additional reduction in drag from other aircraft surfaces (fuselage, empennage).

A measurement of the total efficiency gain when considering all components (wing, fuselage, empennage, etc.) of the UAV is obtained by performing comparative flight tests for a UAV with a conventional wing and the same UAV with a morphing wing.

5.3 Design of the Morphing Camber System

The wing will be equipped with flexible ribs to morph its camber. The flexibility of the ribs is made possible using vertical slits. Each slit allows the ribs to perform a small rotation as if a pivot connection had been added to the system. By distributing the slits along the ribs, the wing's overall behavior becomes like the one of a morphing camber system (MCS). The functionality and efficiency of this approach have been demonstrated using the morphing leading edge (MLE) and the morphing trailing edge (MTE) concept developed in (Communier, Botez, & Wong, 2019), (Communier, Botez, & Wong, 2019). The maximum displacement of the MLE and the MTE was determined as follows:

$$\text{Maximum displacement} = \sum_{i=1}^n y_i, \quad (5.1)$$

where:

$$y = \frac{l \times L}{p}, \quad (5.2)$$

where n is the number of slits, l the width of the slit, p represents the depth of the slit, and finally, L represents the distance between the slit and the end of the rib (Communier, Botez, & Wong, 2019).

Using the slits dimensions given in Table 5.1 and Table 5.2, a maximum MTE displacement y of 1.33 in (33.78 mm), and a maximum MLE displacement y of 0.322 in (8.18 mm) were obtained using Equation (5.1) and Equation (5.2). This displacement corresponds to the one observed on the model before the surface is installed on the wing.

Table 5.1 Slits' dimensions on the trailing edge of the rib

Slit number	l_n (in)	L_n (in)	p_n (in)
1	0.026	4.911	0.416
2	0.026	4.635	0.4
3	0.021	3.609	0.34
4	0.021	3.338	0.317
5	0.014	2.317	0.233
6	0.014	2.053	0.205

Table 5.2 Slits' dimensions on the leading edge of the rib

Slit number	l_n (in)	L_n (in)	p_n (in)
1	0.012	0.436	0.262
2	0.014	0.623	0.306
3	0.018	0.817	0.340
4	0.021	1.037	0.317
5	0.024	1.258	0.394
6	0.026	1.507	0.413

The MLE displacement can also be obtained using a Finite Element Analysis (FEA) (Grisval & Liauzun, 1999) under CATIA V5 with a 3.3% error with respect to its experimental determined value (Figure 5.3).

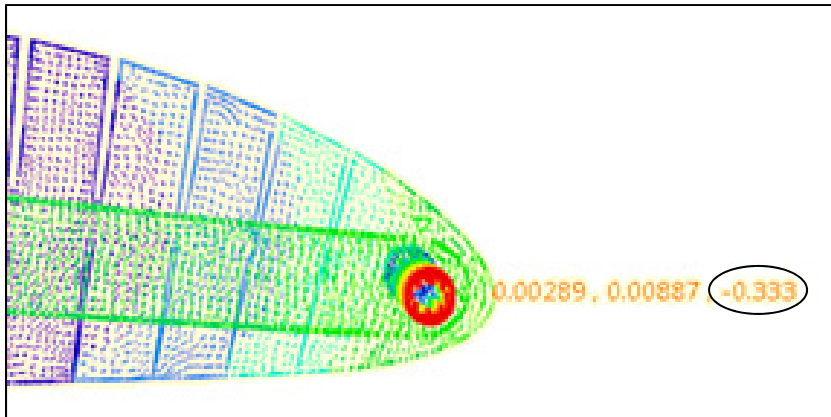


Figure 5.3 MLE tip maximum displacement of 0.333 in (8.46 mm)

The maximum displacement of the MTE was not obtained directly from the FEA, as it was limited by the CATIA V5 software at a maximum rotation of 10° for the MTE displacement (Figure 5.4).

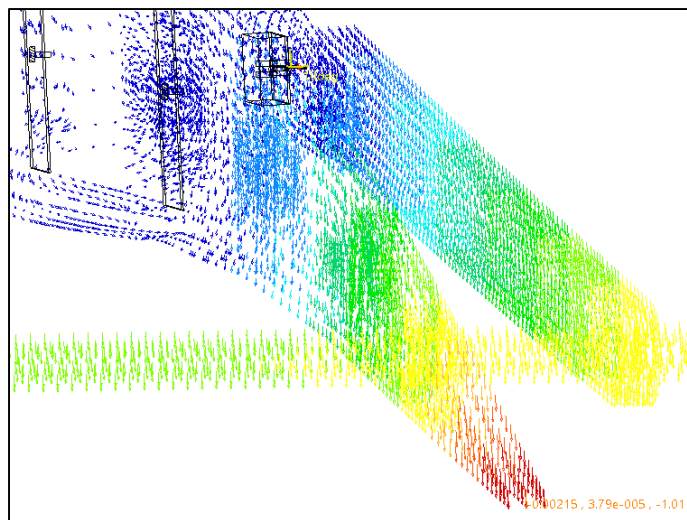


Figure 5.4 MTE tip displacement of 1.01 in (25.65 mm) for a 10° rotation of servomotor

We note, however, that the displacement of the MTE is linearly proportional to the rotation angle of the servomotor (Table 5.3). As shown in Table 5.3, a rotation of 13.4° (angle corresponding to the calculate maximum displacement of 1.33 in (33.78 mm)) for the MLE

tips is obtained for its deformation of 1.357 in (34.47 mm), which corresponds to a 2.06% of relative error. This displacement is reduced once the surface is installed on the wing because the heat-shrinkable plastic used to hide the slits folds back on itself, which reduces the width of the slits.

Table 5.3 MTE tip displacement values according to the servomotor angle of rotation

Servomotor angle	Tip displacement
0°	0 in
5°	0.549 in
10°	1.01 in
13.4°	1.357 in

The impact of each morphing system on the overall wing behaviour is obtained thanks to the two previous studies on the MTE ((Figure 5.5) (Communier, Botez, & Wong, 2019). (Communier, Botez, & Wong, 2019)) and on the MLE (Figure 5.6).

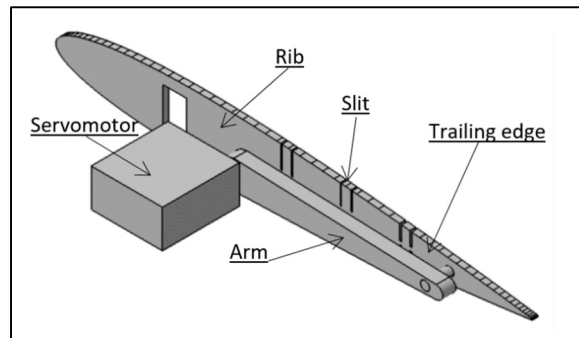


Figure 5.5 MTE system

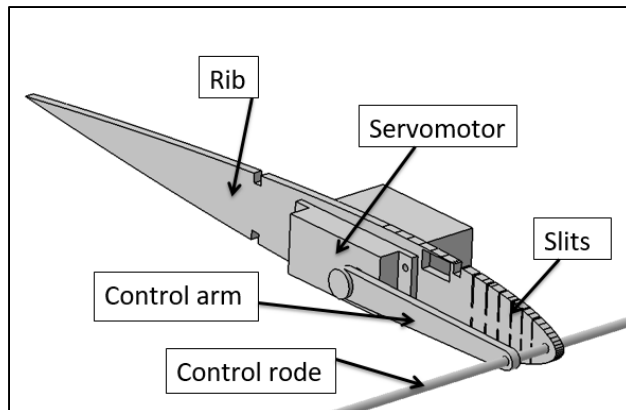


Figure 5.6 MLE system

The MCS is a combination of these two morphing systems, and it maintains the dimensions of the slits for the trailing edge (Table 5.1) and the leading edge (Table 5.2), as shown in Figure 5.7. Consequently, it becomes possible to identify potential interactions between the MTE system and the MLE system aerodynamic performance.

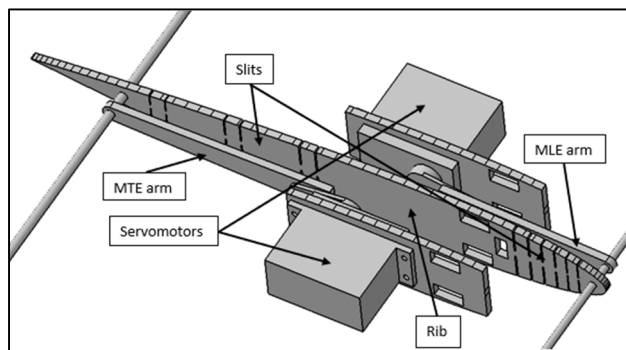


Figure 5.7 MC system

To compare MCS performances with those of a non-morphing system, the prototype of the MCS must have the same dimensions as the non-morphing system (reference wing): 10 in (254 mm) chord, 12 in (304.8 mm) in span. The MCS have a morphing section span of 9.5 in (241.3 mm) with 1 in (25.4 mm) on each side of the morphing section that can not be morphed. The last 0.5 in (12.7 mm) of remaining span was needed to embed the wing to the

circular base of the aerodynamic loading scales. The total span in contact with the airflow was 11.5in (292.1 mm).

The morphing section of the wing is composed of three ribs, which are connected by rods to its trailing and leading edges. These connections allow the ribs to move in parallel, which results in an identical morphing along the span of the morphing section. To obtain a very good aerodynamic behavior, a heat-shrinkable plastic was installed on the surface of the wing. When this plastic was installed over the slits, the morphing surface moved, maximizing the spacing between the slits, and preserving the maximum displacement of morphing for the control surfaces.

Figure 5.8 shows the internal structure of the wing with its MCS. In previous prototypes (MTE and MLE), the servomotors were fixed on the central rib. The MCS required two servomotors, two servomotor brackets were added next to the central rib on the wing structure. All other features of the design (ribs with slits, main spars, control rods, control arms), shown in Figure 5.8, were design in the MTE, for the rear part of the wing, or in the MLE, for the front part of the wing.

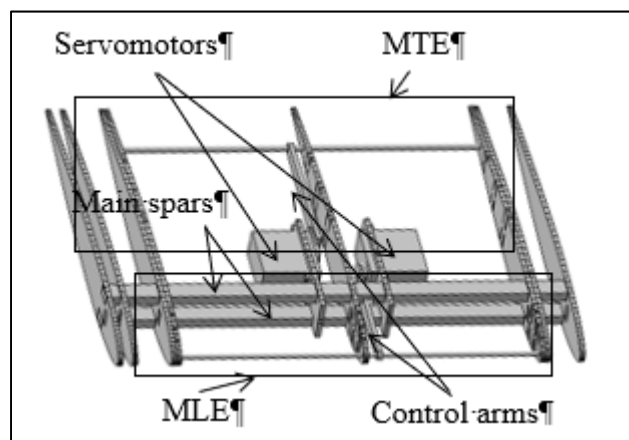


Figure 5.8 MC system internal assembly

5.4 Prototype manufacturing

The prototype of the MCS requires wood as raw material, while the other parts are made from commercially available material and hardware. All the wooden pieces, with the sole exception of the spar, were cut with a LASER cutting machine, enabling the pieces to be connected (with glue) together. To ensure the correct positioning of the pieces during gluing, the jigs were also done with plywood and cut using the LASER machine. These jigs provide the exact spacing between the ribs to obtain a morphing span of 9.5 in (241.3 mm) with an overall span of 12in (304.8 mm), the angle of incidence of the ribs and the perpendicularity of the ribs according to the main spars (Figure 5.9).

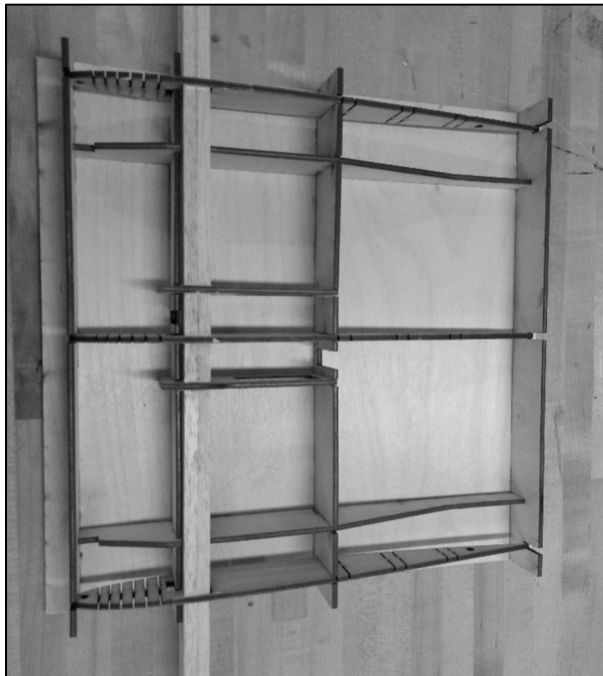


Figure 5.9 Morphing ribs place in the manufacturing guide

The prototype was manufactured in two phases. First, the central section was constructed. This section corresponds to the MCS of the wing, with a span of 9.5 in (241.3 mm). Each rectangular part of the wing surface was LASER-cut to ensure the straightest slits possible, as shown in Figure 5.10.



Figure 5.10 Central section of the wing corresponding to the MC system

In order to obtain the surface at the leading edge, the balsa leaves were moistened, and then shaped into molds (Figure 5.11). The molds were also cut with a LASER cutting machine on plywood.

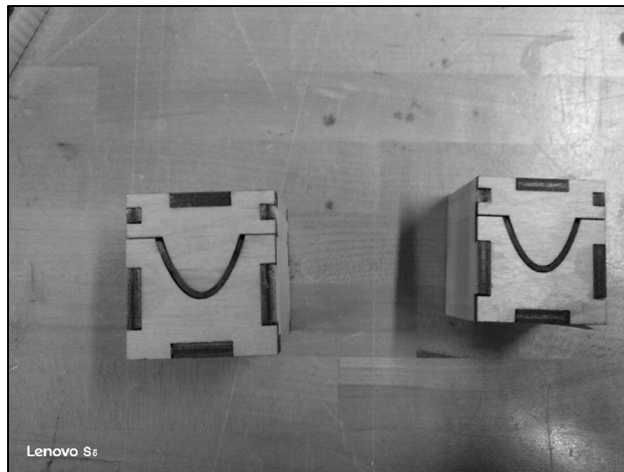


Figure 5.11 Leading edge mold

5.5 The Price – Païdoussis wind tunnel

The LARCASE laboratory is equipped with the Price-Païdoussis subsonic wind tunnel (Figure 5.12), which has already been used in many LARCASE projects ((Tchatchueng Kammegne, Grigorie, Botez, & Koreanschi, 2014), (Communier, Botez, & Wong, 2019), (Andre, et al., 2017), (Koreanschi, Sugar-Gabor, & Botez, 2016), (Ben Mosbah, Salinas, Botez, & Dao, 2013)).

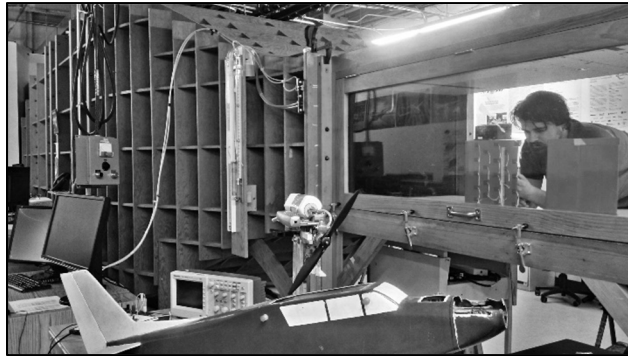


Figure 5.12 Price - Païdoussis subsonic wind tunnel of LARCASE

This open circuit wind tunnel (Figure 5.13) is modular and allows test chambers of different sizes. The test chamber used for wing testing with the MCS is 2 ft (0.609 m) tall, 3 ft (0.914 m) wide and 4 ft (1.219 m) long Figure 5.14). This test chamber size enables measurement of model aerodynamic performance at speeds ranging from 6 m/s to 35 m/s.

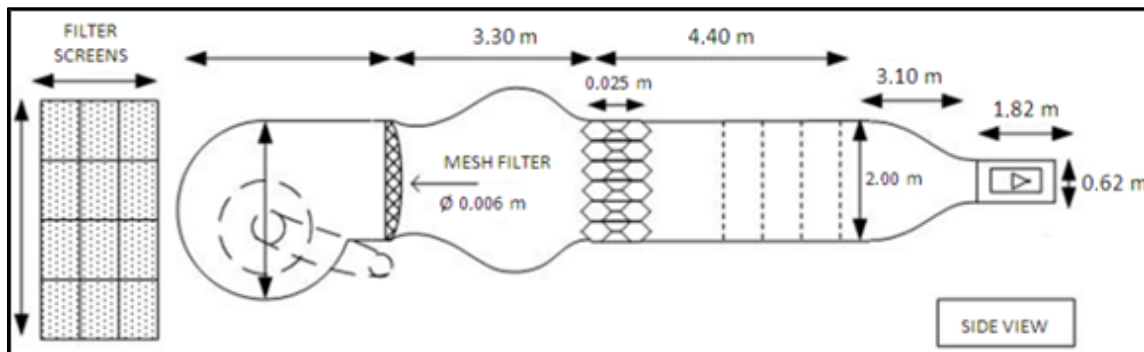


Figure 5.13 Dimensions of the Price - Païdoussis subsonic wind tunnel

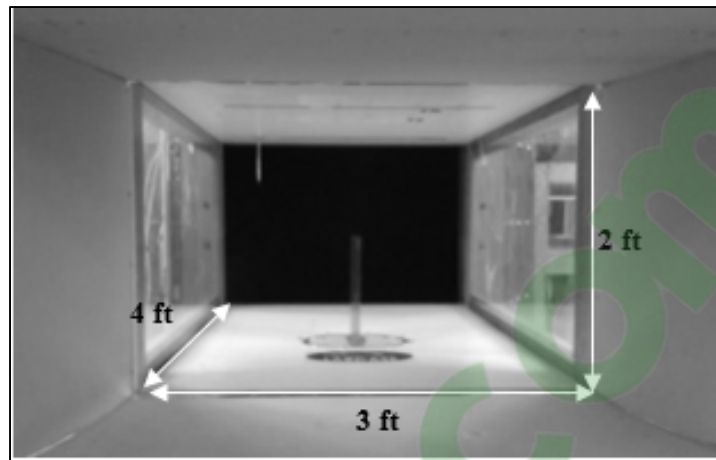


Figure 5.14 Dimension of the test chamber of the wind tunnel

To obtain results, the wind tunnel was equipped with an aerodynamic loading scales whose design and implementation are explained in (Andre, et al., 2017), (Communier, Flores Salinas, Carranza Moyao, & Botez, 2015), (Machetto, Communier, Botez, Carranza Moyao, & Wong, 2017) (Figure 5.15). The aerodynamic loading scales allowed measurement of the forces (Communier, Flores Salinas, Carranza Moyao, & Botez, 2015), to control a servomotor installed in the test wing (Andre, et al., 2017), and to control the change of the angle of attack of the wing during testing (Machetto, Communier, Botez, Carranza Moyao, & Wong, 2017). For the tests of the wing with the MCS, a servomotor control was added to the interface. The interface had to be modified to allow the display of the forces according to the second servomotor.

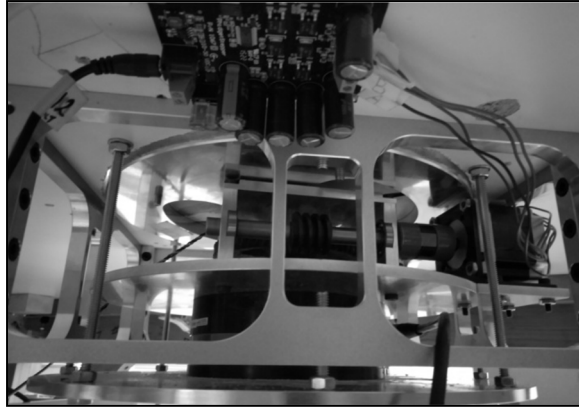


Figure 5.15 Aerodynamic loading scales

5.6 Result

During wind tunnel tests, the aerodynamic forces of drag and lift were measured on the MCS. All tests were carried out at a speed of 20 m/s, for an air density of 1.18 kg/m³. The leading and trailing edges of the wing were morphed according to their angle values presented in Table 5.4.

Table 5.4 Morphing cases studied in wind tunnel

Case study	MTE angle	MLE angle
Fixed wing	N/A	N/A
MCS 0	0°	0°
MCS 5	5°	5°
MCS 10	10°	10°
MTE 5	5°	0°
MTE 10	10°	0°

For each of these cases, the drag (Figure 5.16) and the lift (Figure 5.17) forces variation curves with the angle of attack were plotted using measurements carried out in the wind tunnel. From these measured values, the performance of the wing with the MCS was studied. The drag coefficients variation showed in Figure 5.16 that the wing with the MCS generated more drag than a fixed wing (without control surface) for an angle of attack higher than -7°, and that its stall angle was lower by 4°. The difference in the variation of the drag coefficient obtained for each morphing case was too small to be analyzed from Figure 5.16.

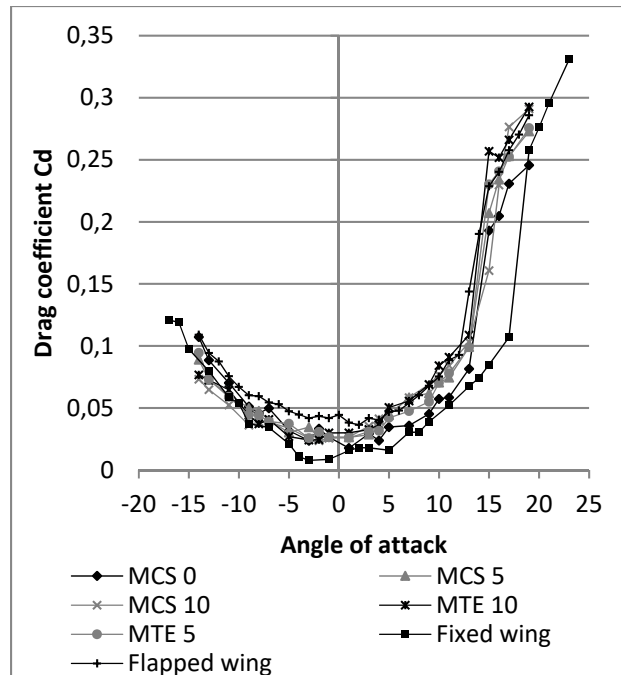


Figure 5.16 Drag coefficient variation with the angle of attack

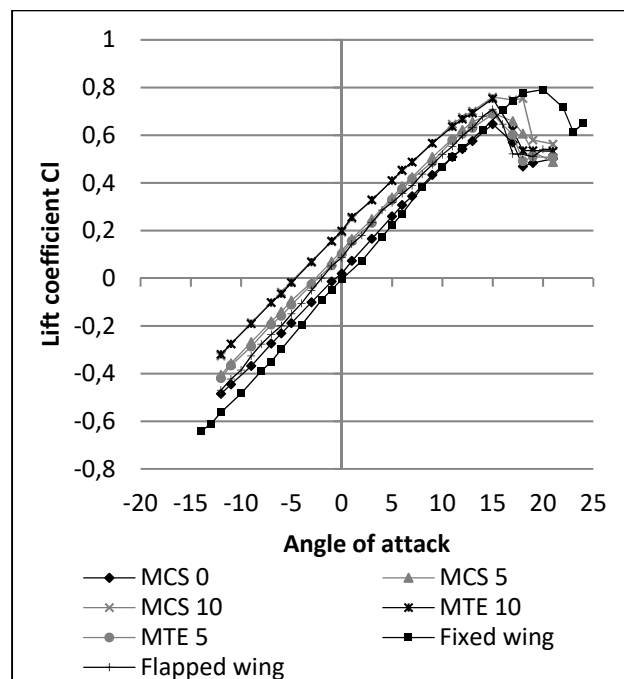


Figure 5.17 Lift coefficient variation with the angle of attack

The lift coefficient variation curves show Figure 5.17 that the MTE acts on the variation of the lift coefficient of the wing by causing a shift to the left, for a positive angle. The MLE has no effect on the value of the lift coefficient for an angle of attack of 0° and the slope of the variation of the lift coefficient.

Figure 18 shows that the L/D variations with the angle of attack values are close to each other for each of morphing camber cases. The maximum L/D tends to shift to the left of the curves (closer to the angle of attack 0°) when the morphing of the camber increases. It is also shown that the MCS reduces the L/D of the wing for angles of values of 5° to the stall angle, but for angles smaller than 5° , the MCS gives the highest L/D.

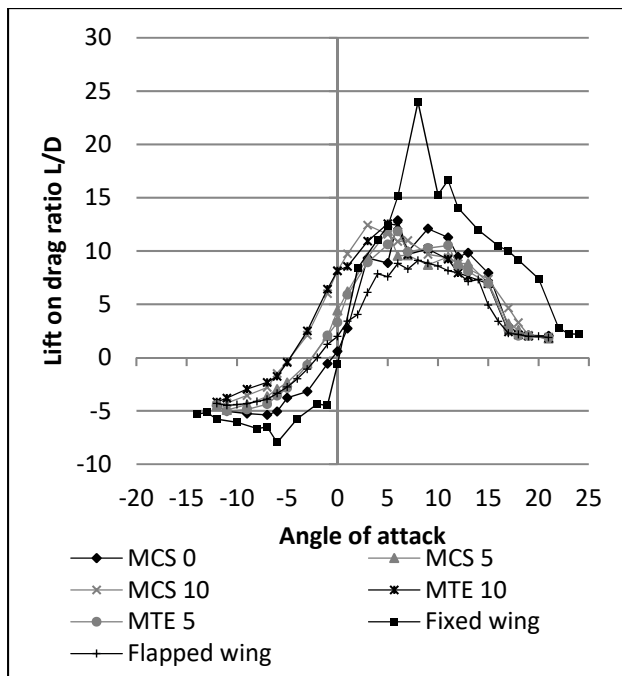


Figure 5.18 Lift on drag ratio variation with the angle of attack

Figure 5.19 shows a modification of wing behavior during the stall when camber morphing is at 10° (case MC 10). These behaviors of the drag and lift coefficient variation curves with the morphing of the trailing and leading edges are identical to those observed during independent analyses of the MTE and MLE systems (Communier, Botez, & Wong, 2019). It can thus be

seen that the presence of the MLE system does not generate any interferences on the MTE system and that there is not an additional drag due to the combination of the two systems on the same wing.

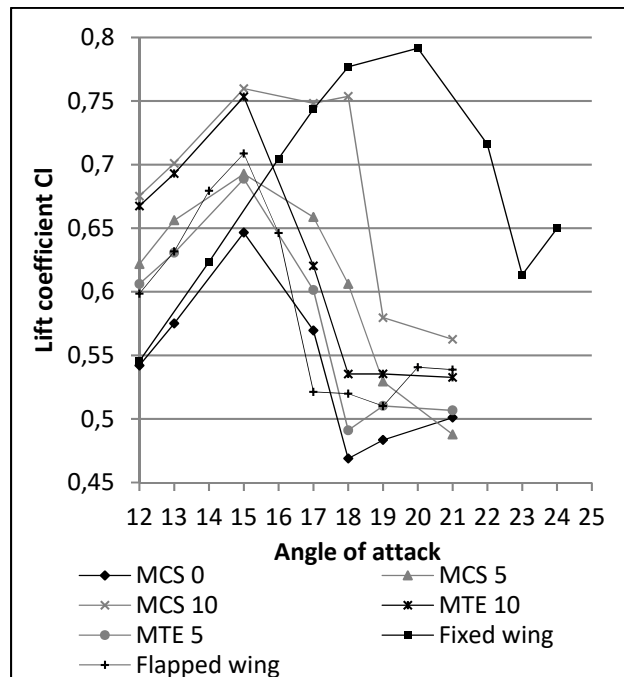


Figure 5.19 Lift coefficient variation with the angle of attack around the stall angle

The following figures and discussion will only consider the MCS 0, MCS 5, MCS 10 and Fixed Wing cases to improve the visibility of the curves. However, these curves alone cannot assess the effectiveness of the wing with the MCS because of the fact that for a given angle, the MCS provides more lift, but generates more drag, than a fixed wing. In the next section, the methodology to conclude on the effectiveness of the MCS is discussed.

5.7 Discussion

During the design of an aircraft, we seek to obtain a target lift value. To allow an analysis of the performance of the wing with the, thus, it is preferred to represent the drag coefficient variation with the lift coefficient. These curves thus made it possible to identify the

configuration that generates the least drag, given a target lift coefficient value. This idea allows to define its specific morphing configuration for drag minimization, for each flight case of an aircraft, characterized by a needed lift. The drag coefficient variation differences are small between each case study. As we want to establish the effectiveness of the MCS for its use on an aircraft, we can reduce the number of measurements displayed by keeping only the measurement for positive lift coefficients, and by removing the measurements corresponding to the stall angles. Thus, in Figure 5.20, the values obtained for each case studied are compared. It can be observed that a fixed wing allows obtaining the least drag in the range of lift coefficients allowed by the NACA0012 airfoil. However, this wing has no control surface for controlling the aircraft, which means that this configuration is not functional for an aircraft.

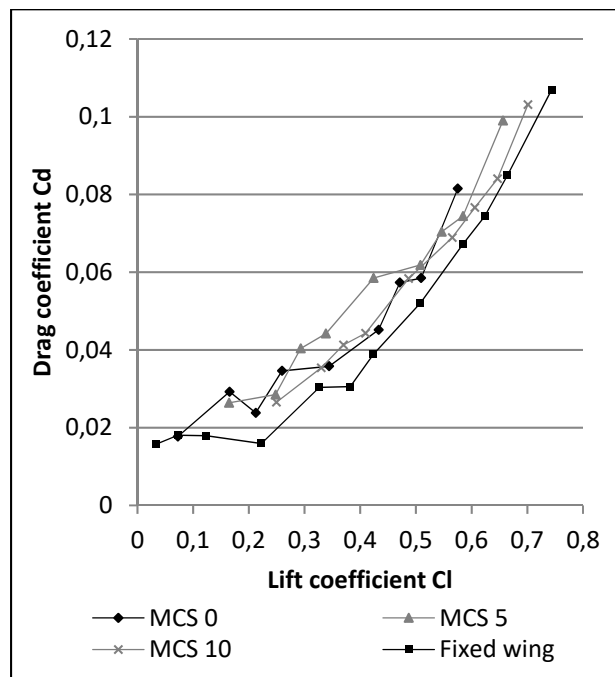


Figure 5.20 Drag coefficient variation with the lift coefficient variation

The fixed wing configuration was studied for the comparison of its result with those of an MCS 0 configuration. The differences in these two cases for the variation of drag coefficient with the angle of attack (Figure 5.20) came from the interference between the MCS and

aerodynamic fluid around the wing. The variation of the MCS 0 and MCS 10 drag coefficient values are too close for the lift coefficient values between 0.25 and 0.5 to define which configuration would generate less drag than the other configuration. For a lift coefficient value less than 0.1, the MCS 0 case generates less drag; similarly, for a lift coefficient value greater than 0.5, the MCS 10 case generates less drag. There is no lift coefficient value for which the MCS 5 case generates less drag, but for lift coefficient values less than 0.25 and between 0.5 and 0.6, the MCS 5 case is very close to the MCS 10 case. It would therefore be preferred to make the transition between the MCS 0 case and the MCS 10 case when the lift coefficient required to make the aircraft fly will be between 0.5 and 0.6. The drag generated by the wing during a flight will be minimized.

5.8 Application of results with the UAS-S4 Ehécatl

The Unmanned Aerial System (UAS) S4 Ehécatl is an autonomous flight system. It includes an onboard camera, an autopilot and the sensors necessary for its operation. The UAS-S4 Ehécatl model was developed in Mexico by Hydra Technologies in 2002 and made its first flight in 2006. It is therefore a continuous development project for almost 15 years. UAS-S4 Ehécatl is used by the Mexican army and police. As part of the research developed at the Research Laboratory in active control, avionics and aeroservoelasticity (LARCASE), we use it to develop new methods of analysis, design and manufacturing applied to morphing wings. The geometries for the UAS-S4 in this paper are in Table 5.5.

Table 5.5 Geometric data of the UAS-S4

Geometry	Value
Wing Surface S	2.9769 m ²
Root chord CR	656.159 mm
Wing span b	4.19 m
Wing Taper Ratio λ	0.6057

To measure the impact of the MCS on the drag and lift forces of the UAS-S4, we must calculate the C_{d0} and the cl_{α} values from the lift and drag coefficients values using Equation (5.3).

The value of cl_α can be calculated using the equation:

$$Cl_\alpha = \frac{cl_\alpha}{1 + \frac{cl_\alpha}{\pi * AR * e}} \quad (5.3)$$

where the aspect ratio (AR) of the wing is:

$$AR = b / \bar{c}, \quad (5.4)$$

and the Oswald coefficient for a straight wing is:

$$e = 1.78 * (1 - 0.045 * AR^{0.68}) - 0.64, \quad (5.5)$$

The value of Cl_α is obtained from the lift coefficient linear variation curves with the angle of attack (Figure 5.21), and the equations of these curves are presented in Table 5.6.

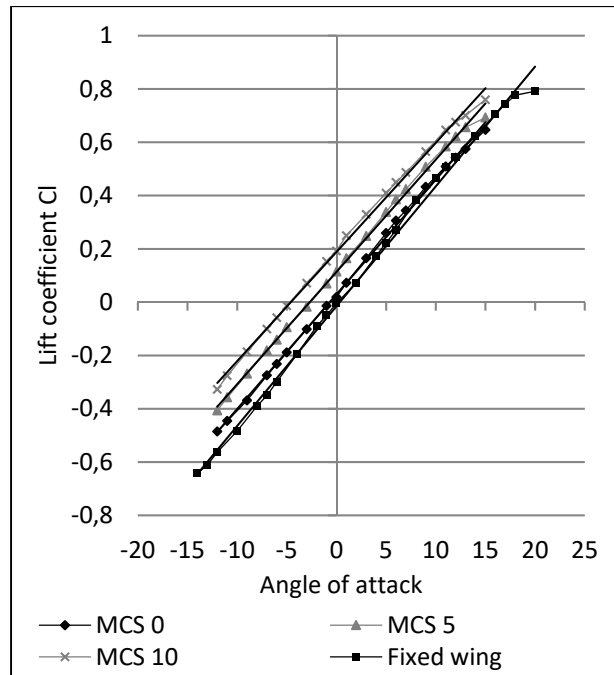


Figure 5.21 Lift coefficient variation curve with the angle of attack

Table 5.6 Equation of lift coefficient variation with angle of attack

Studied cases	Cl equation of variation	Cl_{α}
Fixed wing	$y=0.0446x-0.0112$	0.0446
MCS 0	$y=0.043x+0.0294$	0.043
MCS 5	$y=0.0421x+0.1138$	0.0421
MCS 10	$y=0.041x+0.1885$	0.041

The span of the wing in the wind tunnel was 11.5 in. Because the floor of the wind tunnel acts as a symmetry plane with respect to the aerodynamics flow around the wing, the span considered for the calculation must be 23 in., and the chord has 10 in. The aspect ratio $AR = 2.3$, and the Oswald coefficient value $e = 0.9989$ were obtained. These values allow us to calculate the cl_{α} corresponding to the wing airfoil for each case study. The cl_{α} values are presented in Table 5.7.

Table 5.7 Values of cl_α for each studied case

Case study	cl_α
Fixed wing	0.0449
MCS 0	0.0433
MCS 5	0.0423
MCS 10	0.0412

The value of Cd_0 is calculated using the equation:

$$Cd = Cd_0 - Cd_i, \quad (5.6)$$

where:

$$Cd_i = \frac{cl^2}{\pi * AR * e}, \quad (5.7)$$

From the equations of C_l , the induced drag Cd_i for each case studied was calculated (Figure 5.22). The value of Cd was obtained using the drag coefficient variation curve with the angle of attack (Figure 5.23). The equations of these polynomial (2nd order) curves is presented in Table 5.8. From the induced drag Cd_i and the total drag Cd , the value of drag of the skin friction Cd_0 is determined (Figure 5.24).

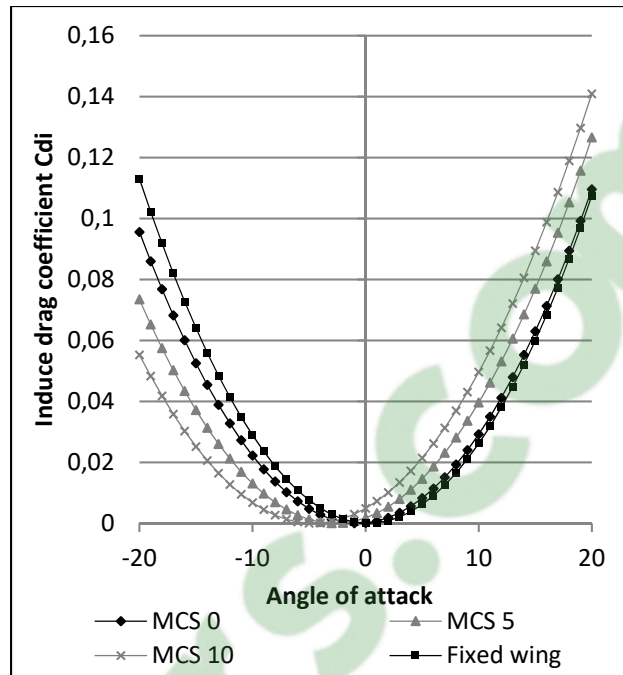


Figure 5.22 Induce drag coefficient variation with the angle of attack

Table 5.8 Equation of drag coefficient variation with angle of attack

Studied cases	Cd equation of variation
Fixed wing	$y = 0.000364x^2 - 0.000397x + 0.010814$
MCS 0	$y = 0.000368x^2 - 0.000446x + 0.022767$
MCS 5	$y = 0.000347x^2 + 0.000788x + 0.028511$
MCS 10	$y = 0.000333x^2 + 0.001496x + 0.028223$

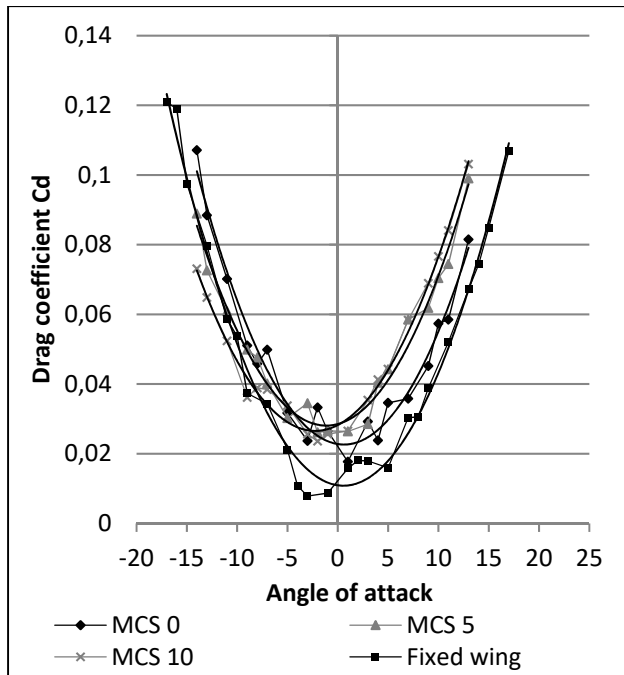


Figure 5.23 Equation of drag coefficient variation with angle of attack

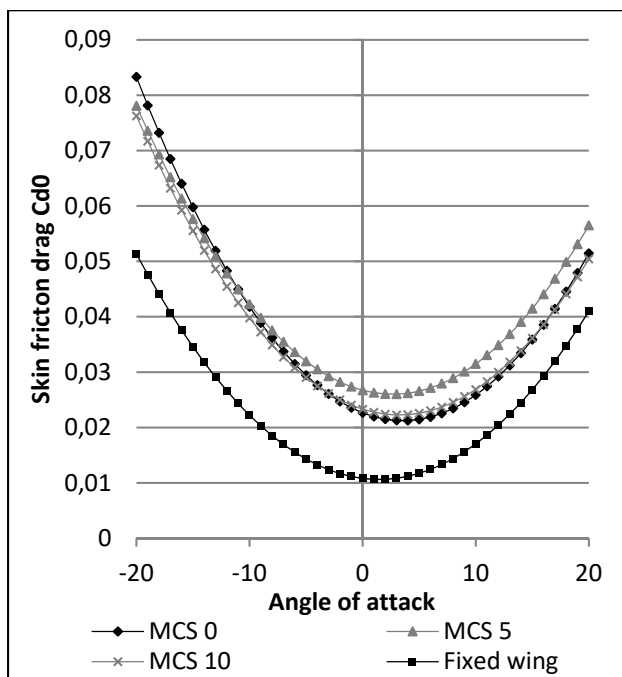


Figure 5.24 Skin friction drag variation with the angle of attack

As shown in Figure 5.20, for the same lift value, the fixed wing generates less drag. However, as seen in Figure 5.17, for the same lift value, the angle of attack of the MCS is lower than that of the fixed wing. This observation implies that the angle of attack of the fuselage for an aircraft using the MCS will be lower than the angle of attack of the fuselage of a conventional aircraft. The variation of the drag coefficient with the lift coefficient is recalculated using the UAS-S4 wing and fuselage geometry as the fuselage geometry needs to be considered. The drag and lift coefficients of the fuselage were obtained using the UAS-S4 in-house simulator for flight conditions corresponding to the wind tunnel tests (20 m/s) (Kuitche & Botez, 2019). The drag and lift performance of the wings were obtained by using Equations (5.3), (5.4) and (5.8) to (5.10) with the previously calculated cl_α and Cd_0 values, and by use of the wing geometry of UAS-S4.

The equation for modeling the drag coefficient of the fuselage with the angle of attack (AoA) from the drag coefficients used in the simulator at a speed of 20 m/s is:

$$Cd_{of} = 1.442834 * 10^{-6} * AoA^3 + 7.472932 * 10^{-5} * AoA^2 - 3.14648307 * 10^{-4} * AoA + 4.434891635 * 10^{-3}, \quad (5.8)$$

The equation for modeling the lift coefficient of the fuselage with the angle of attack (AoA) from the drag coefficients used in the simulator at a speed of 20 m/s is:

$$Cl_f = 3.08 * 10^{-6} * AoA^3 + 6.872 * 10^{-5} * AoA^2 + 3.33018 * 10^{-3} * AoA - 8.16467 * 10^{-3}, \quad (5.9)$$

In Equations (5.8) and (5.9), the angle of attack (AoA) is in degrees.

The drag and lift coefficients of the fuselage were expressed according to the surface of the wing. This allows adding the coefficients of the fuselage to the coefficients of the wings. Thus, we could estimate the total drag and lift coefficients according to the following equations:

$$Cl_t = Cl + Cl_f, \quad (5.10)$$

$$Cd_t = Cd_0 + Cd_{0f} + Cd_i + Cd_{if}, \quad (5.11)$$

where:

$$Cd_{if} = \frac{Cl_f^2}{\pi * AR * e}, \quad (5.12)$$

Equation (5.13) will be used for calculating the Oswald coefficient (Raymer, 2018) because of the fact that the wing of UAS-S4 is trapezoidal with a sweep angle $\Lambda_{LE} = 6.353^\circ$ and $AR = 10.4785$.

$$e = 4.61 * (1 - 0.045 * AR^{0.68}) * (\cos \Lambda_{LE})^{0.15} - 3.1, \quad (5.13)$$

By use of Equation (5.3) for the calculation of Cl_α of the wing, the values of Cl_0 of the test wings, the variation curves of the lift coefficient of the wing with the angle of attack can be traced in Figure 5.25. Then, Equations (5.9) and (5.10) give the lift coefficient variations for the wing and fuselage assembly (Figure 5.26).

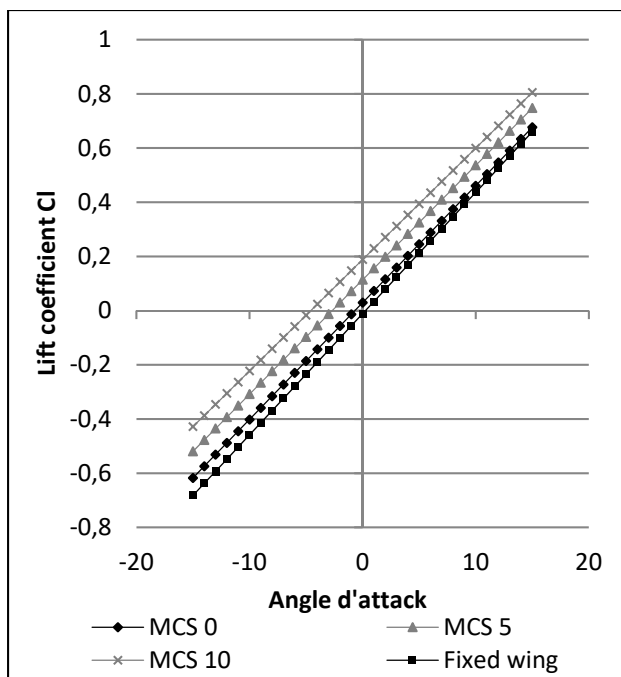


Figure 5.25 Lift coefficient variation with angle of attack for the UAS-S4 wing

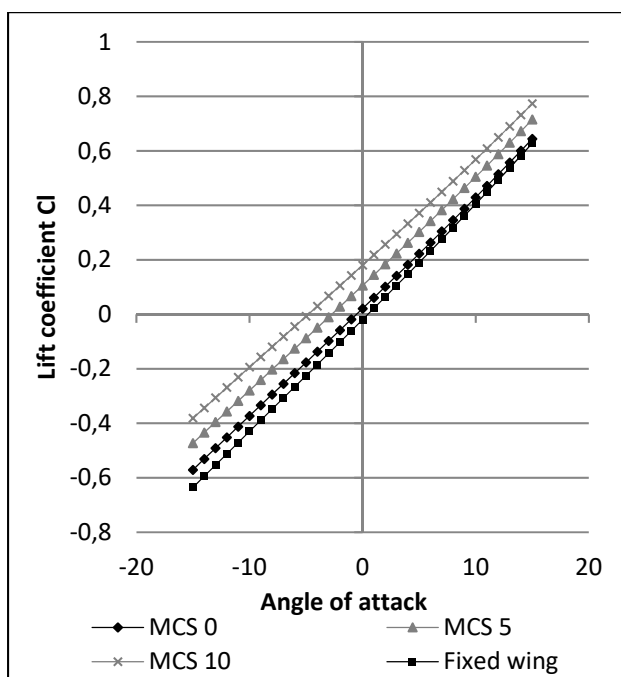


Figure 5.26 Lift coefficient variation with angle of attack for UAS-S4 (wing + fuselage)

Equation (5.7) allows the calculation of the induced drag coefficients for the UAS-S4 wing from the lift coefficients of the wing. Then, with Equation (5.11), the combination of wing and fuselage drag coefficients of the UAS-S4 are plotted (Figure 5.27).

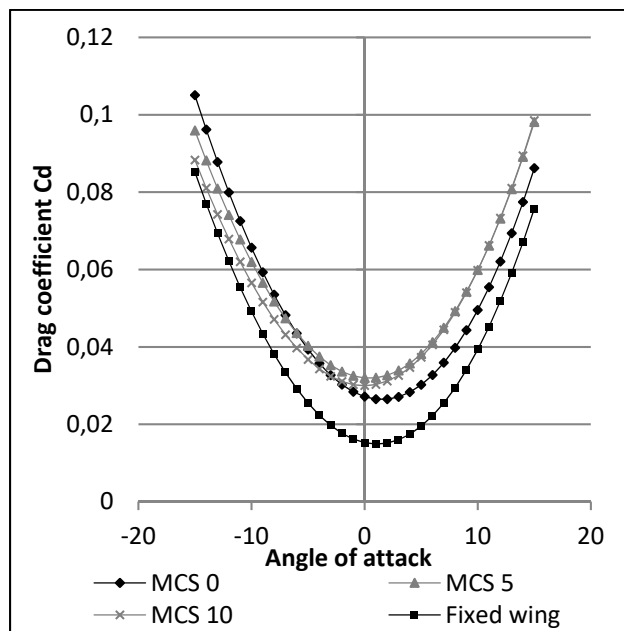


Figure 5.27 Drag coefficient variation with the angle of attack for UAS-S4

Once the drag and lift coefficient variation curves are obtained, the graph representing the variation of the drag coefficient with the lift coefficient is plotted (Figure 5.28). As seen in Figure 5.29, for a lift coefficient greater than 0.48, the wing with a morphing of the camber of 10° (MCS 10) generates less drag than a fixed wing. This value corresponds, in Figure 5.26, to an angle of attack of 11° for a fixed wing, and of 7° for a wing with a morphing of the camber of 10° . This observation indicates that for the aircraft lift coefficient greater than 0.48, the MCS will be more advantageous than the fixed wing.

These values were calculated for a wing with a NACA0012 airfoil whose performances were obtained in the wind tunnel. This is not the airfoil used in the current UAS-S4, but it is a close one, the values are useful for potential gain that can be provided using an MCS on the UAS-S4.

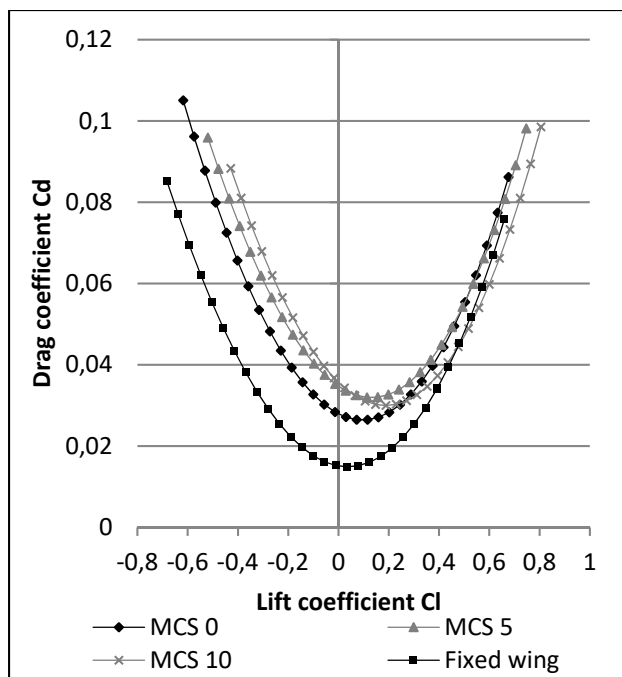


Figure 5.28 Drag coefficient variation with the lift coefficient for the UAS-S4

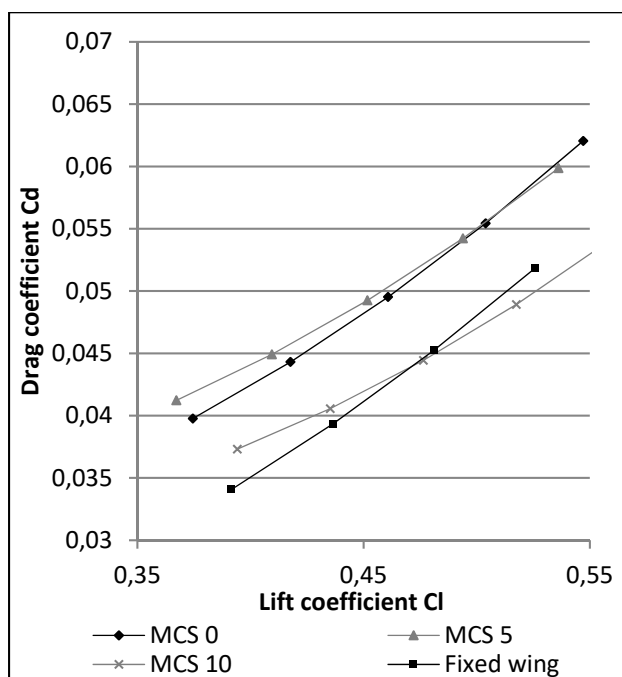


Figure 5.29 Drag coefficient variation with the lift coefficient for UAS-S4 (zoom)

5.9 Conclusion

In this article, a new system allowing the complete morphing of the camber, from the airfoil leading edge to its trailing edge, was presented from its design to its validation in a wind tunnel. The design of this system provides an easy-to-manufacture and lightweight MCS for the wing structure. The MCS will consequently not penalize the performance of the aircraft from its weight point of view. The method used to calculate the maximum displacements of the MLE and of the MTE makes it easy to size the slits without having to perform an FEA optimization process. In order to apply this method, the thickness of the material remaining at the slits must allow the rib bending without causing its plastic deformation. To ensure this bending, anisotropic materials, such as wood or carbon fibers in the direction of the length of the rib will be more effective than isotropic materials, such as steel or aluminum. The wind tunnel tests, despite having a lower than expected maximum morphing capabilities due to the manufacturing method, showed that the MCS improved the aerodynamic performance of the wings, and of the UAS-S4. The MTE and MLE systems were also shown to be independent. The MTE acted on the lift of the wing, and the MLE acted on the stall angle, thus, independent control of both systems was allowed. Wind tunnel performance scaling was used to determine the potential gain from using an MCS on the UAS-S4. The next step will be to design an MCS with the dimensions used for the UAS-S4 wing.

Author Contributions

Investigation, methodology, writing, D.C.; Supervision, Writing-review & editing, R.M.B. and T.W.

Funding

This research received no external funding

Acknowledgments

The authors would like to sincerely thank the Natural Sciences and Engineering Research Council of Canada (NSERC) for the Canada Research Chair Tier 1 in Aircraft Modelling and Simulation New Technologies funding, as well as the McGill University professors Dr. Michael Païdoussis and Dr. Stuart Price for the donation of the Price–Païdoussis wind tunnel at the LARCASE, ÉTS.

Conflicts of Interest

The authors declare that there is no conflict of interest regarding the publication of this paper.

CHAPTER 6

DISCUSSION OF RESULTS

In the preceding chapters, we could see how the MCS was functioning. In Chapter 3, it could be seen that the trailing edge of the wing could be morphed using slits in the ribs. This chapter showed that the methodology made it possible to modify the shape of the wing, and that the obtained morphing makes it possible to reduce the drag of the wing if a conventional aileron was replaced by an MTE. In addition, an analysis of the wing behavior as function the angle of the MTE ((Communier, Botez, & Wong, 2019)) made it possible to show that the MTE could allow a UAV such as the UAS-S4 Ehécatl, to make its turns only by morphing the wing. This operation would allow the removal of the aileron from the wing.

Chapter 4 demonstrated that the methodology made it possible to modify the LE of the wing and to increase the stall angle of the wing. However, an improvement in the manufacturing of the system was made in order to obtain the complete desired MLE.

Finally, Chapter 5 showed that the two systems, MTE and MLE, could operate in parallel on one wing with an impact on the lift of the wing separately for the MTE and the MLE. Thus, the MLE only modifies the stall angle of the wing, and the MTE only modifies the C_{L0} of the wing.

As seen in Figure 6.1, the MCS model allows the NACA0012 airfoil of the wing to be morphed to a shape very close to the NACA4412 airfoil. The MLE needs to cover a larger portion of the wing chord than the actual system to obtain a better superposition between the morphed airfoil and the NACA4412 airfoil. In Figure 6.1, NACA4411 airfoil correspond to the shape of the wing ribs. Once the wing skin has been added around the ribs, the shape of the NACA4412 airfoil was obtained. Figure 6.1 presents the NACA0012, NACA4411 and NACA4412, as well as the morphed airfoil of the wing for a rotation of 5° of the MLE, and 5° of the MTE.

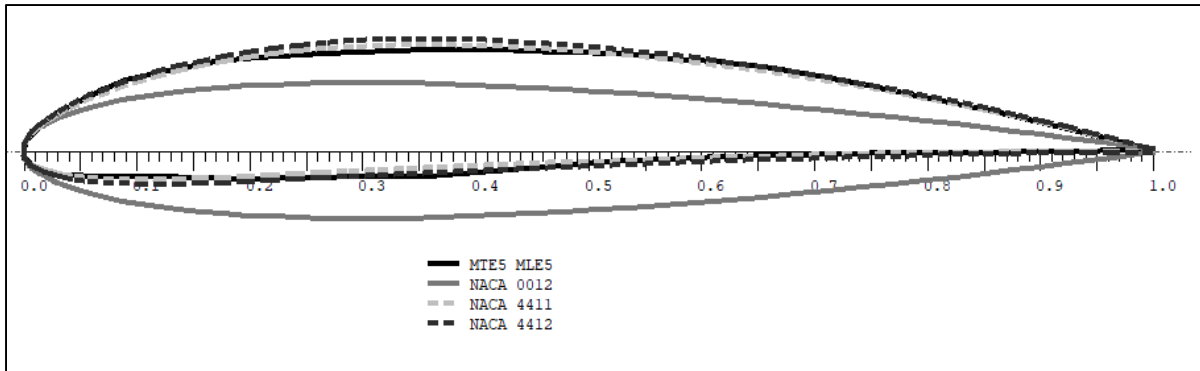


Figure 6.1 Shapes of NACA0012, NACA4411, NACA4412 and MLE

The theoretical performances were obtained for the morphed airfoil and the NACA4412 airfoil. In Figure 6.2 and Figure 6.3, the results obtained with XFLR5 code are shown. The studied wings had a span of 23 in and a chord of 10 in. The considered speed was 20 m/s and the analysis method used was 3D Panels.

Figure 6.2 shows that the lift coefficient variation with the angle of attack of the morphed wing corresponds to the lift of the NACA4412 wing. The gray curve represents the lift coefficient variation with the angle of attack of the NACA0012 wing which corresponds to the shape of the morphing wing without deformation. There is a constant difference of 0.2 between the lift coefficients of the NACA0012 wing and the NACA4412 wing for each angle of attack. An early stall at angle of attack of 15° is found for the morphed wing (the numerical analysis stops when stall angle is reach). During the wind tunnel test, a stall around 15° is also observed for the MCS. For the NACA0012 wing, the stall angle is observed around 20° .

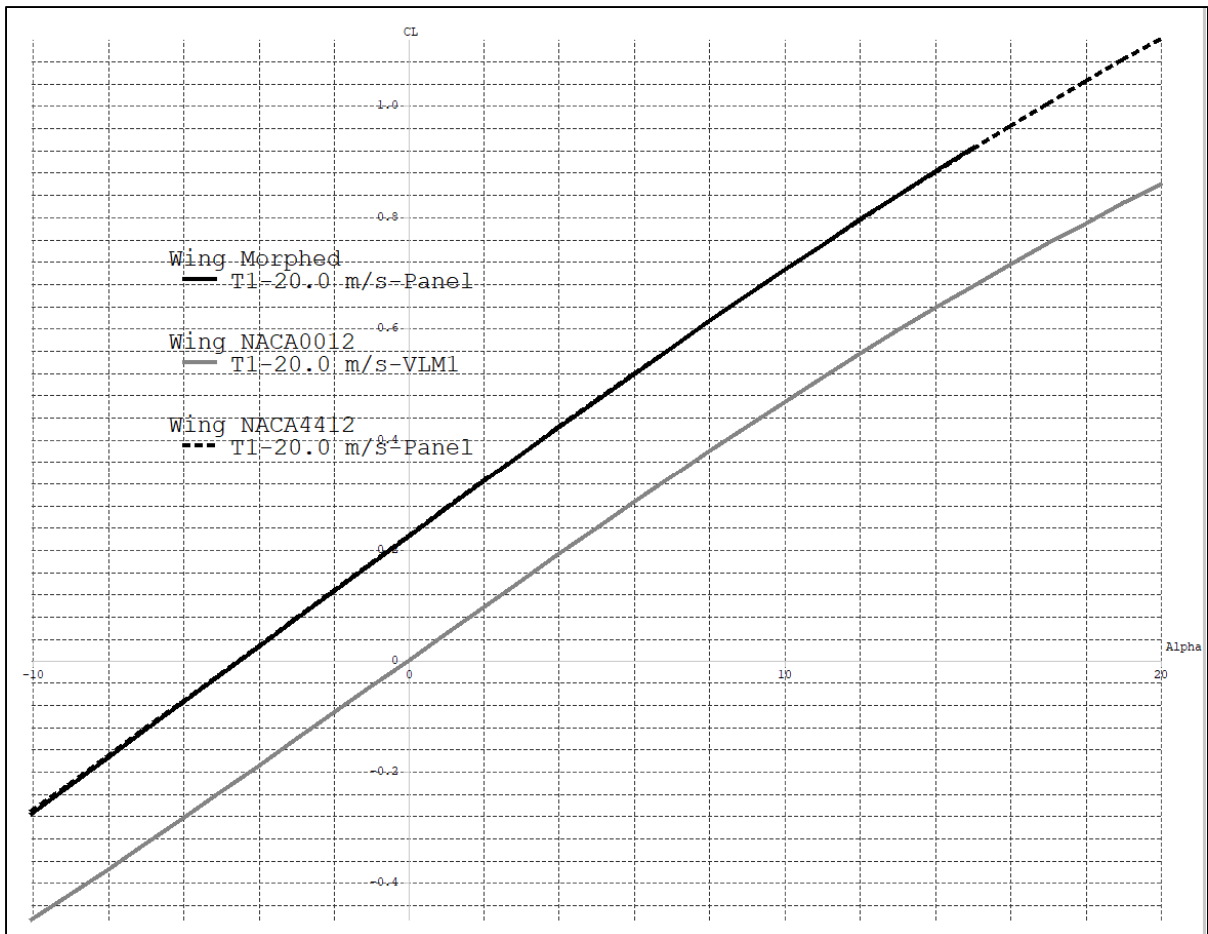


Figure 6.2 Lift coefficient variation with the angle of attack (theoretical using XFLR5 code)

Figure 6.3 shows the drag coefficient variation with the angle of attack. We can see that the drag coefficient of the morphed wing is higher than that of the NACA4412 wing. This is most likely due to the contour of the morphed wing which is not clean as the contour of the NACA4412 wing. As the center part of the wing is fixed, even if the morphed shape is close to the NACA4412 airfoil shape, it is not the same. These differences between the NACA4412 airfoil shape and the morphed airfoil shape induce a shift in the maximum thickness position (29% of the chord for NACA4412 to 36% of the chord for the morphed wing) and in the value of the camber (4% at 40% of the chord for the NACA4412 airfoil, and 3.82% at 53.02% of the chord for the morphed wing airfoil), which led to an increase of the wing drag.

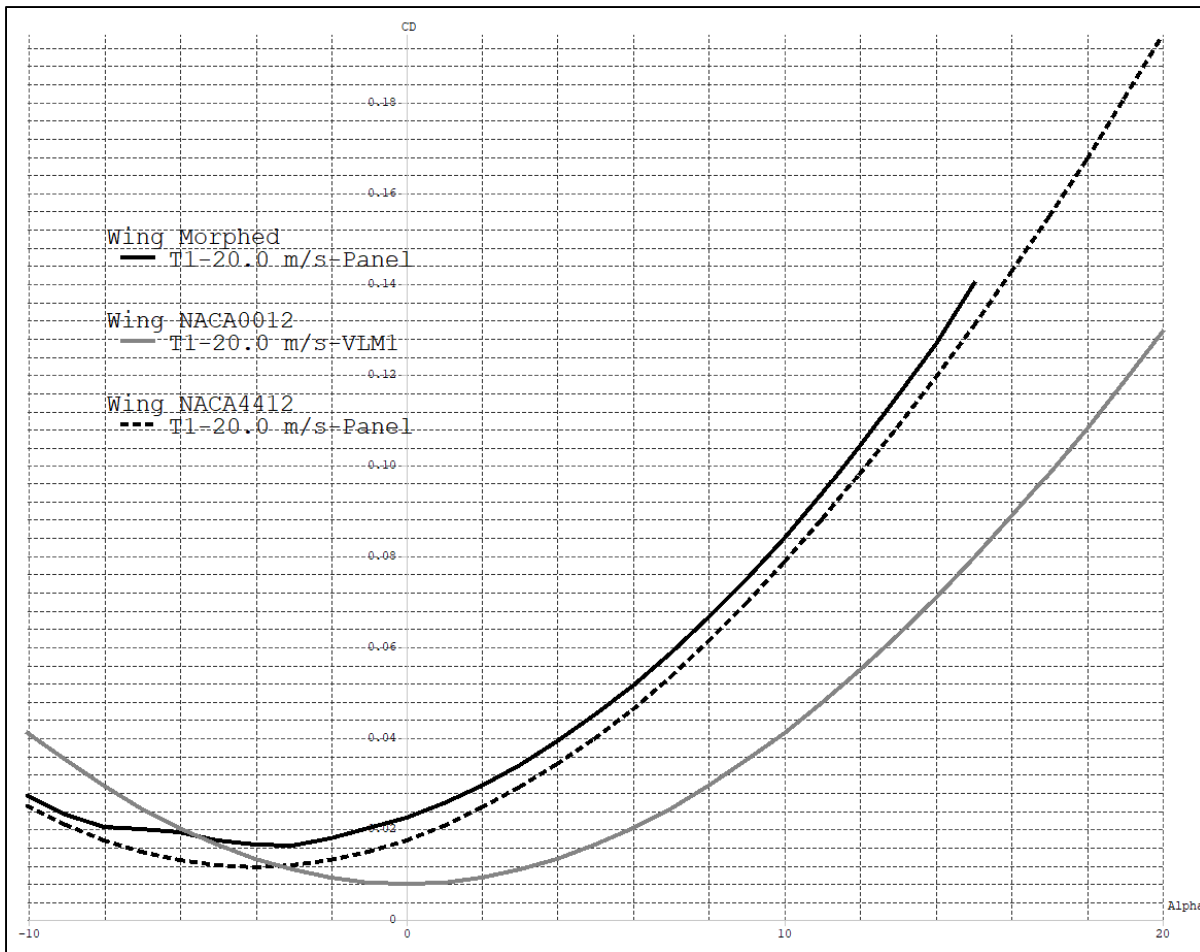


Figure 6.3 Drag coefficient variation with the angle of attack (theoretical)

During the design of the MCS, the servomotors positions were changed; these positions were no longer fixed on the morphing ribs. Therefore, it was possible to increase the morphing area of the ribs and thus to obtain better continuity in the deformation of the ribs. This operation would reduce the drag of the wing.

This analysis of the morphed airfoil demonstrates that the MCS is capable to change the shape of a NACA0012 airfoil to the shape of a NACA4412 airfoil for a wing.

During this research, the dimensions of the UAS-S4 Ehécatl were used for our analyses of the MCS functionality. The UAS-S4 uses the NACA2310 airfoil. This airfoil is thinner than the NACA0012 airfoil, but as seen in Figure 6.4, a rotation of the MTE of 1° , and a rotation of the MLE of 3° allow to obtain a very close shape to the shape used for the wings of the UAS-S4 Ehécatl (NACA2310).

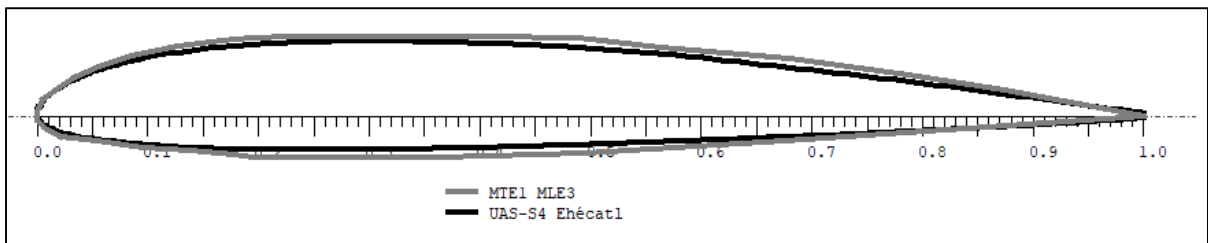


Figure 6.4 Shape of UAS-S4 Ehécatl wing airfoil and morphed airfoil

The similarity between the airfoil of the UAS-S4 Ehécatl and the morphed airfoil shown in Figure 6.4 justifies that the MCS could be used on the UAS-S4 Ehécatl.

In this thesis, three morphing systems are analyzed. Even if the MCS is a combination of the MTE and the MLE, it is not always the best choice. The mission that the aircraft to be designed would need to perform will determine the choice of the system. As the MLE can be used alone, the choice would need to be done between the MTE and the combination of the MTE and the MLE (Camber System). If the aircraft to be designed would need to fly at high angles of attack (close to the stall angle), the MCS will be chosen as it would allow the delay of the stall angle. But if the aircraft will fly only at low angles of attack (close to 0°), the use of the MLE will not be needed. Therefore, it will be better to use the MTE alone as it is a lighter weight system than the MCS, and it generates less drag than the MCS.

CONCLUSION AND RECOMMENDATIONS

This thesis presents a morphing wing system that allows to modify the shape of a wing airfoil from a NACA0012 airfoil to a NACA4412 airfoil. This morphing system reduces the drag generated by the ailerons of the wing by replacing them with the MTE. The MLE makes possible the delay of the stall. It is thus possible to avoid the stall of the wing during the take-off, landing and cornering phases in the slow flight phase. The combination of the MTE and MLE makes it possible to obtain a complete morphing of the wing camber necessary to convert a NACA0012 airfoil into a NACA4412 airfoil. The MCS, allows the UAS to reduce its angle of attack, and thus to reduce its drag.

This morphing system uses the same servomotor already used in the UAS-S4 in order to ensure that the method of actuating the morphing system does not increase the weight of the UAS. The morphing of the wing is done via the ribs bending, using slit along the height of the ribs. A method of calculation was developed in order to easily determine the amplitude of deformation from the sizes of the slits. This design made it possible to obtain flexible ribs without requiring additional parts, that would increase the weight of the structure. The morphing system presented in this thesis makes it possible to obtain morphing wing without increasing the total weight of the UAS versus the classical wing.

This thesis presents an innovative and easy-to-manufacture concept allowing the independent morphing of the leading edge, and the trailing edge of the wing of a UAS. The operation of the morphing wing system has been validated by wind tunnel tests. The analysis of the results shows that this system improves the aerodynamic performances of the UAS. These improvements translate, at equal lift, in drag reduction of the UAS with a morphing system with respect to the UAS without morphing system.

During this research, the sizing of the slits was obtained, so that the system remained functional, it is therefore recommended to optimize their sizes. This optimization could further reduce the drag of the UAS and allow to delay the stall angle of the wing. It can also

increase the deformation range of the system which is of 4 mm. Even if the morphing systems presented in this thesis need an increase of the power consumption of the aircraft, the potential reduction in power consumption is much higher than the power consumption increase.

The airfoil used to validate the morphing systems is NACA0012. The studied system can morph up and down with the same amplitude. During a flight, more amplitude of the leading edge with down motion than up motion is needed. It is therefore recommended to perform a morphing system design using the amplitude (downwards and upwards) needed for the UAS-S4 Ehécatl in order to determine the gains for the UAS-S4 Ehécatl aerodynamical coefficients.

To obtain the real gain that this morphing system can provide for a UAS, it is recommended to design a UAS with two sets of wings. One wing would be equipped with the morphing system and the other wing would have an aileron for its control. By programming the UAS to perform an identical route with the two sets of wings; the total consumption of the engine for the length of the trip will determine if the morphing system will provide, and quantify a real gain once implemented on a UAS. To obtain very good data, the tests must be performed under stable climatic conditions for the longest possible path length. These tests could be done to have the UAV run in circles until the battery reaches a critical level and count the number of turns with the ground station. The number of turns will determine which system allows the longest run time.

BIBLIOGRAPHY

- Abdessemed, C., Yao, Y., Narayan, P., & Bouferrouk, A. (2017). Unsteady Parametrization of a Morphing Wing Design for Improved Aerodynamic Performance. *52nd 3AF International Conference on Applied Aerodynamics*. Lyon, France.
- Aero@Net, & Cnc@Net. (2004, décembre). *Utilitaire Profscan*. Retrieved décembre 13, 2017, from <http://www.teaser.fr/~abrea/cncnet/logiciel/profscan.phtml>
- Amendola, G., Dimino, I., Pecora, R., & Amoroso, F. (2015). Actuation System Design for a Morphing Aileron. *Applied Mechanics and Materials*. 798, pp. 582-588. Trans Tech Publications.
- Andre, T., Communier, D., Flores, M., Botez, R., Carranza Moyao, O., Wong, T., & Gauthier, G. (2017). Mesure de l'influence d'un aileron sur le comportement aérodynamique en soufflerie. *Substance ÉTS*.
- Barbarino, S., Bilgen, O., Ajaj, R. M., Friswell, M. I., & Inman, D. J. (2011). A review of morphing aircraft. *Journal of intelligent material systems and structures*, 22(9), 823-877. doi:10.1177/1045389X11414084
- Ben Mosbah, A., Botez, R. M., & Dao, T.-M. (2014). New methodology for the prediction of the aerodynamic coefficients of an ATR-42 scaled wing model. *SAE 2014 aerospace systems and technology conference*. Cincinnati, OH, USA.
- Ben Mosbah, A., Botez, R. M., & Dao, T.-M. (2016). A hybrid original approach for prediction of the aerodynamic coefficients of an ATR-42 scaled wing model. *Chinese Journal of Aeronautics*, 29(1), 41-52.
- Ben Mosbah, A., Salinas, M. F., Botez, R. M., & Dao, T.-m. (2013). New Methodology for Wind Tunnel Calibration using Neural Networks-EGD Approach. *SAE International Journal of Aerospace*, 6(2), 761-766. doi:10.4271/2013-01-2285
- Berton, B. (2006). *Shape memory alloys application: trailing edge shape control*. SAINT-CLOUD (FRANCE): DASSAULT AVIATION.
- Blondeau, J., Richerson, J., & Pines, D. J. (2003). Design, development and testing of a morphing aspect ratio wing using an inflatable telescopic spar. *AIAA paper*, 1718, 7-10.

- Botez, R. M., Koreanschi, A., Sugar Gabor, O., Mebarki, Y., Mamou, M., Tondji, Y., ... Concilio, A. (January 2017). Numerical and experimental testing of a morphing upper surface wing equipped with conventional and morphing ailerons. *55th AIAA Aerospace Sciences Meeting*, (p. 1425). Grapevine, Texas, USA. doi:10.2514/6.2017-1425
- Cai, Z., & Ross, R. J. (2010). Mechanical properties of wood-based composite materials. *Wood Handbook, Wood as an Engineering Material*, 12--1.
- Carossa, G. M., Ricci, S., De Gaspari, A., Liauzun, C., Dumont, A., & Steinbuch, M. (2015). Adaptive Trailing Edge: Specifications, Aerodynamics, and Exploitation. *Smart Intelligent Aircraft Structures*, (pp. 143-158). Springer, Cham. doi:10.1007/978-3-319-22413-8_7
- Chanzy, Q., & Keane, A. (2018, March). Analysis and Experimental Validation of Morphing UAV Wings. *The Aeronautical Journal*, 122(1249), 390-408. doi:10.1017/aer.2017.130
- Communier, D. (2015). *Méthodologie de modélisation aérostructurale d'une aile utilisant un logiciel de calcul aérodynamique et un logiciel de calcul par éléments finis*. École de technologie supérieure.
- Communier, D., Botez, R. M., & Wong, T. (2017). Aero-structural analysis - Creation of a wing assembly with non-linear aerodynamic pressure distribution on its surface. *CASI AERO 2017*. Toronto.
- Communier, D., Botez, R. M., & Wong, T. (2019). Rolling Authority of a Morphing Trailing Edge System Design. *AERO 2019: Aircraft Design & Development Symposium*. Laval, QC.
- Communier, D., Botez, R., & Wong, T. (2019). Experimental Validation of a New Morphing Trailing Edge System using Price - Païdoussis Wind Tunnel Tests. *Chinese Journal of Aeronautics*.
- Communier, D., Flores Salinas, M., Carranza Moyao, O., & Botez, R. M. (2015). Aero Structural Modeling of a Wing using CATIA V5 and XFLR5 Software and Experimental Validation using the Price-Païdoussis Wing Tunnel. *AIAA Atmospheric Flight Mechanics Conference*. Dallas, TX, USA. doi:10.2514/6.2015-2558

- Concilio, A., Dimino, I., Pecora, R., & Ciminello, M. (January 2016). Structural Design of an Adaptive Wing Trailing Edge for Enhanced Cruise Performance. *24th AIAA/AHS Adaptive Structures Conference*, (p. 1317). San Diego, California, USA. doi:10.2514/6.2016-1317
- Elzey, D. M., Sofla, A. Y., & Wadley, H. N. (2003). A bio-inspired high-authority actuator for shape morphing structures. *Smart structures and materials 2003: Active Materials: Behavior and Mechanics*, 5053, 92-101.
- Elzey, D. M., Sofla, A. Y., & Wadley, H. N. (2005). A shape memory-based multifunctional structural actuator panel. *International Journal of Solids and Structures*, 42(7), 1943-1955.
- Fischer, C., Terriault, P., & Brailovski, V. (2012). Debonding Characterization of SMA/Polymer Morphing Structures. *Advanced Materials Research*, 409, 621-626.
- Fraqueiro, F. R., Albuquerque, P. F., & Gamboa, P. V. (2016). A computer application for parametric aircraft design. *Open Engineering*, 6(1), 432-440. doi:10.1515/eng-2016-0067
- Gabor, O. S., Koreanschi, A., & Botez, R. M. (2012). Low-speed aerodynamic characteristics improvement of ATR 42 airfoil using a morphing wing approach. *IECON 2012-38th annual conference on IEEE Industrial Electronics Society* (pp. 5451-5456). Montréal, QC, Canada: IEEE. doi:10.1109/IECON.2012.6388954
- Gandhi, F., & Anusonti-Inthra, P. (2008). Skin design studies for variable camber morphing airfoils. *Smart Materials and Structures*, 17(1), 015025.
- Grisval, J.-P., & Liauzun, C. (1999). Application of the Finite Element Method to Aeroelasticity. *Revue européenne des éléments finis*, 8(5-6), 553-579. doi:10.1080/12506559.1999.10511397
- Grisval, J.-P., Liauzun, C., & Johan, Z. (June 22-25, 1999, April 7). Aeroelasticity Simulations in Turbulent Flows. *CEAS/AIAA/ICASE/NASA Langley International Forum on Aeroelasticity and Structural Dynamics 1999* (pp. 287-297). Williamsburg, VA, USA: National Aeronautics and Space Administration.
- Howell, L. L. (2001). *Compliant Mechanisms*. John Wiley & Sons.

- Howell, L. L., & Midha, A. (1994). A method for the design of compliant mechanisms with small-length flexural pivots. *Journal of mechanical design*, 116(1), 280-290.
- Jacobs, E. N., Ward, K. E., & Pinkerton, R. M. (1933). *The characteristics of 78 related airfoil sections from tests in the variable-density wind tunnel*.
- Katz, J., & Plotkin, A. (2001). *Low-speed aerodynamics* (Vol. 13). Cambridge university press.
- Konstadinopoulos, P., Thrasher, D., Mook, D., Nayfeh, A., & Watson, L. (1985, January). A vortex-lattice method for general, unsteady aerodynamics. 22(1), 43-49.
- Koreanschi, A., Sugar Gabor, O., Ayrault, T., Botez, R. M., Mamou, M., & Mebarki, Y. (2016). Numerical Optimization and Experimental Testing of a Morphing Wing with Aileron System. *24th AIAA/AHS Adaptive Structures Conference*, (p. 1083). San Diego, CA. doi:10.2514/6.2016-1083
- Koreanschi, A., Sugar-Gabor, O., & Botez, R. M. (2016). Drag Optimisation of a Wing equipped with a Morphing Upper Surface. *The Aeronautical Journal*, 120(1225), 473-493.
- Koreanschi, A., Sugar-Gabor, O., & Botez, R. M. (2016). Numerical and Experimental Validation of a Morphed Wing Geometry using Price-Paidoussis Wind-Tunnel Testing. *The Aeronautical Journal*, 120(1227), 757-795.
- Kota, S., Hetrick, J. A., Osborn, R., Paul, D., Pendleton, E., Flick, P., & Tilmann, C. (2003). Design and application of compliant mechanisms for morphing aircraft structures. *Smart Structures and Materials 2003: Industrial and Commercial Applications of Smart Structures Technologies*, 5054, 24-34.
- Kuitche, M. A., & Botez, R. M. (2019, January). Modeling novel methodologies for unmanned aerial systems - Application to the UAS-S4 Ehecatl and the UAS-S45 Balaam. *Chinese Journal of Aeronautics*, 32(1), 58-77. doi:10.1016/j.cja.2018.10.012
- Launder, B. E., & Spalding, D. B. (1974, March). The Numerical Computation of Turbulent Flows. *Computer Methods in Applied Mechanics and Engineering*, 3(2), 269-289. doi:10.1016/0045-7825(74)90029-2

- Liauzun, C. (July 2006). Assessment of CFD Techniques for Wind Turbine Aeroelasticity. *ASME 2006 Pressure Vessels and Piping/ICPVT-11*, 9, pp. 341-350. Vancouver, BC, Canada. doi:10.1115/PVP2006-ICPVT-11-93800
- Machetto, A., Communier, D., Botez, R., Carranza Moyao, O., & Wong, T. (2017). Automatisation du changement d'angle d'une aile dans la soufflerie Price--Païdoussis du LARCASE. *Substance ÉTS*.
- Michaud, F., Joncas, S., & Botez, R. M. (2013). Design, Manufacturing and Testing of a Small-Scale Composite Morphing Wing. *19th International Conference on Composite Materials*. Montreal.
- Monner, H. P., D., S., & Elmar J., B. (2000). *Design aspects of the elastic trailing edge for an adaptive wing*. GERMAN AEROSPACE CENTER. BRAUNSCHWEIG (GERMANY): INST OF STRUCTURAL MECHANICS.
- Monner, H. P., Hanselka, H., & Breitbach, E. J. (1998). Development and design of flexible fowler flaps for an adaptive wing. *Smart Structures and Materials 1998: Industrial and Commercial Applications of Smart Structures Technologies*, 3326, 60-71.
- Moosavian, A., Chae, E. J., Pankonien, A. M., Lee, A. J., & Inman, D. J. (2017). A parametric study on a bio-inspired continuously morphing trailing edge. *Bioinspiration, Biomimetics, and Bioreplication 2017*, 10162, 1016204.
- Nemec, M., Zingg, D. W., & Pulliam, T. H. (2004). Multipoint and multi-objective aerodynamic shape optimization. *AIAA journal*, 42(6), 1057-1065.
- Noor, M., Wandel, A. P., & Yusaf, T. (1-3 Jul 2013). Detail Guide for CFD on the Simulation of Biogas Combustion in Bluff-Body Mild Burner. *2nd International Conference of Mechanical Engineering Research (ICMER 2013): Green Technology for Sustainable Environment*, (pp. 1-25). Pahang, Malaysia. Retrieved from <http://eprints.usq.edu.au/id/eprint/23716>
- Onen, A. S., Cevher, L., Senipek, M., Mutlu, T., Gungor, O., Uzunlar, I. O., ... Tekinalp, O. (2015). Modeling and controller design of a VTOL UAV. *Unmanned Aircraft Systems (ICUAS), 2015 International Conference on* (pp. 329-337). IEEE. doi:10.1109/ICUAS.2015.7152307
- Park, K., Han, J.-W. L.-J., Kim, B.-S., & Lee, J. (2008). Optimal design of airfoil with high aspect ratio in Unmanned Aerial Vehicles. *World Academy of Science, Engineering and Technology*, 2(4), 171-177.

Patankar, S. V., & Spalding, D. B. (1968). *Heat and Mass Transfer in Boundary Layers*. Morgan-Grampian.

Pecora, R., Barbarino, S., Concilio, A., Lecce, L., & Russo, S. (2011, August 8). Design and Functional Test of a Morphing High-Lift Device for a Regional Aircraft. *Journal of Intelligent Material Systems and Structures*, 22(10), 1005-1023. doi:10.1177/1045389X11414083

Peel, L. D., Mejia, J., Narvaez, B., Thompson, K., & Lingala, M. (2009). Development of a Simple Morphing Wing Using Elastomeric Composites as Skins and Actuators. *Journal of Mechanical Design*, 131(9), 091003.

Phillips, W. F., & Snyder, D. O. (2000, July). Modern adaptation of Prandtl's classic lifting-line theory. *Journal of Aircraft*, 37(4), 662-670.

Poonsong, P. (2004). *Design and analysis of a multi-section variable camber wing*.

Popov, A. V., Grigorie, T. L., Botez, R. M., Mamou, M., & Mebarki, Y. (2010). Closed-Loop Control Validation of a Morphing Wing using Wind Tunnel Tests. *Journal of Aircraft*, 47(4), 1309-1317.

Popov, A. V., Grigorie, T. L., Botez, R. M., Mamou, M., & Mébarki, Y. (2010). Real Time Morphing Wing Optimization Validation Using Wind-Tunnel Tests. (AIAA, Ed.) *Journal of Aircraft*, 47(4), 1346-1355. doi:10.2514/1.47431

Radestock, M., Riemenschneider, J., Monner, H. P., Huxdorf, O., Werter, N. P., & De Breuker, R. (2016). Deformation Measurement in the Wind Tunnel for an UAV Leading Edge with a Morphing Mechanism. *30th Congress of International Council of the Aeronautical Sciences*. Daejeon.

Raymer, D. (2018). *Aircraft Design: A Conceptual Approach*. American Institute of Aeronautics, Inc.

Reich, G., & Sanders, B. (2007). Introduction to morphing aircraft research. *Journal of aircraft*, 44(4), 1059-1059.

Renukumar, B., Bramkamp, F. D., Hesse, M., & Ballmann, J. (2006). Effect of Flap and Slat Riggings on 2-D High-Lift Aerodynamics. *Journal of Aircraft*, 43(5), 1259-1271.

- Rudenko, A., Radestock, M., & Monner, H. P. (2016). Optimization, Design and Structural Testing of a High Deformable Adaptive Wing Leading Edge. *24th AIAA/AHS Adaptive Structures Conference*, (p. 1314). San Diego.
- Sanders, B., Eastep, F. E., & Forster, E. (2003). Aerodynamic and Aeroelastic Characteristics of Wings with Conformal Control Surfaces for Morphing Aircraft. *Journal of Aircraft*, *40*(1), 94-99.
- Shili, L., Wenjie, G., & Shujun, L. (2008). Optimal design of compliant trailing edge for shape changing. *Chinese Journal of Aeronautics*, *21*(2), 187-192.
- Sodja, J., Martinez, M. J., Simpson, J. C., & De Breuker, R. (2015). Experimental evaluation of the morphing leading edge concept. *23rd AIAA/AHS Adaptive Structures Conference*, (p. 0791). Kissimmee.
- Sofla, A. Y., Meguid, S. A., Tan, K. T., & Yeo, W. K. (2010). Shape morphing of aircraft wing: Status and challenges. *Materials & Design*, *31*(3), 1284-1292.
- Sugar Gabor, O., Koreanschi, A., & Botez, R. M. (2012, October). Low-speed aerodynamic characteristics improvement of ATR 42 airfoil using a morphing wing approach. *IECON 2012-38th Annual Conference on IEEE Industrial Electronics Society* (pp. 5451-5456). Montreal, QC: IEEE.
- Sugar Gabor, O., Koreanschi, A., Botez, R. M., Mamou, M., & Mebarki, Y. (2016). Numerical Simulation and Wing Tunnel Tests Investigation and Validation of a Morphing Wing-Tip Demonstrator Aerodynamic Performance. *Aerospace Science and Technology*, *53*, 136-153. doi:10.1016/j.ast.2016.03.014
- Takahashi, H., Yokozeki, T., & Hirano, Y. (2016). Development of Variable Camber Wing with Morphing Leading and Trailing Sections using Corrugated Structures. (E. SAGE Publications Sage UK: London, Ed.) *Journal of Intelligent Material Systems and Structures*, *27*(20), 2827-2836.
- Tchatchueng Kammegne, M. J., Grigorie, L. T., Botez, R. M., & Koreanschi, A. (2014). Design and Validation of a Position Controller in the Price-Paidoussis Wind Tunnel. *Proceeding of Modelling, Simulation and Control IASTED Conference*. Banff.
- Tchatchueng Kammegne, M. J., Grigorie, L. T., Botez, R. M., & Koreanschi, A. (2016). Design and wind tunnel experimental validation of a controlled new rotary actuation system for a morphing wing application. *Proceedings of the Institution of Mechanical Engineers, Part G: Journal of Aerospace*, *230*(1), 132-145.

- Tchatchueng Kammegne, M. J., Khan, S., Grigorie, L. T., & Botez, R. M. (2016). New methodology for the controller of an electrical actuator for morphing a wing. *23rd AIAA/ASME/AHS Adaptive Structures Conference, Science and Technology Forum, 2015*. Kissimee, FL, USA.
- Triet, N. M., Ngoc, V. N., & Thang, P. M. (2015). Aerodynamic Analysis of Aircraft Wing. *VNU Journal of Science: Mathematics-Physics, 31*(2), 68-75.
- Vorobiev, A. N., Rennie, R. M., Jumper, E. J., & McLaughlin, T. E. (2008). Experimental investigation of lift enhancement and roll control using plasma actuators. *Journal of Aircraft, 45*(4), 1315-1321.
- Wang, D. P., Bartley-Cho, J. D., Martin, C. A., & Hallam, B. J. (2001). Development of high-rate large-deflection hingeless trailing-edge control surface for the Smart Wing wind tunnel model. *Smart structures and materials 2001: Industrial and commercial applications of smart structures technologies, 4332*, 407-419.
- Weisshaar, T. A. (2013, March). Morphing Aircraft Systems: Historical Perspectives and Future Challenges. *Journal of Aircraft, 50*(2), 337-353. doi:10.2514/1.C031456
- Wolfshtein, M. (1969, March). The Velocity and Temperature Distribution in One-Dimensional Flow with Turbulence Augmentation and Pressure Gradient. *International Journal of Heat and Mass Transfer, 12*(3), 301-318. doi:10.1016/0017-9310(69)90012-X
- Woods, B. K., Bilgen, O., & Friswell, M. I. (2014, May 1). Wind Tunnel Testing of the Fish Bone Active Camber Morphing Concept. *Journal of Intelligent Material Systems and Structures, 25*(7), 772-785. doi:10.1177/1045389X14521700
- Woods, B. K., Fincham, J. H., & Friswell, M. I. (2014, July). Aerodynamic modeling of the fish bone active camber morphing concept. *Proceeding of the RAeS Applied Aerodynamics Conference, 2224*. Bristol, UK.

